Aalborg Universitet

Modeling and control of large-signal stability in power electronic-based power systems

Shakerighadi, Bahram

Publication date:
2020

Document Version
Publisher's PDF, also known as Version of record

Link to publication from Aalborg University

Citation for published version (APA):
Shakerighadi, B. (2020). *Modeling and control of large-signal stability in power electronic-based power systems*. Aalborg Universitetsforlag.

MODELING AND CONTROL OF LARGE-SIGNAL STABILITY IN POWER ELECTRONIC-BASED POWER SYSTEMS

BY
BAHRAM SHAKERIGHADI

DISSERTATION SUBMITTED 2020

AALBORG UNIVERSITY
DENMARK

Modeling and control of large-signal stability in power electronic-based power systems

by

Bahram Shakerighadi

AALBORG UNIVERSITY
DENMARK

Dissertation submitted July 24, 2020

Dissertation submitted: July 24, 2020

PhD supervisor: Prof. Frede Blaabjerg,
Aalborg University

Assistant PhD supervisors: Prof. Claus Leth Bak,
Aalborg University

Dr. Esmaeil Ebrahimzadeh,
Ørsted Wind Power A/S, Fredericia, Denmark.

PhD committee: Professor Zhe Chen (chairman)
Aalborg University

Professor JinJun Liu
Xi’an Jiantong University

Professor Qing-Chang Zhong
Illinois Institute of Technology

PhD Series: Faculty of Engineering and Science, Aalborg University

Department: Department of Energy Technology

ISSN (online): 2446-1636
ISBN (online): 978-87-7210-679-3

Published by:
Aalborg University Press
Kroghstræde 3
DK – 9220 Aalborg Ø
Phone: +45 99407140
aauf@forlag.aau.dk
forlag.aau.dk

Printed in Denmark by Rosendahls, 2020

CV

{Bahram Shakerighadi} (SM’ 17) received the B.Sc. degree from University of Mazandaran, Iran, in 2010 and the M.Sc. degree from University of Tehran, Iran, in 2014. He is currently working toward the Ph.D. degree in modeling and stability assessment of the power-electronic-based power systems with Department of Energy Technology, Aalborg University, Denmark.

He was also a Visiting Researcher with ABB Corporate Research, Västerås, Sweden. His current research interests include modeling and stability assessment of Power Electronic-based power systems, and control of grid-tied voltage source converters.

Abstract

Nowadays, power-electronic-based (PE-based) energy sources, such as wind turbines and photovoltaics (PV), are increasing in capacity in electrical grids. Increasing the penetration of PE-based energy sources in power systems changes the scope of stability, security, reliability, and protection assessment of conventional power systems. In modern power systems with a high penetration of PE-based energy sources, the stability issues may lead to outage in a part of the system or even to a blackout. Therefore, it is important to assess PE-based power systems stability challenges to prevent undesired system outages in the grid.

In this project, it is tried to assess stability issues of modern power systems with the focus on the large-signal stability challenges. The project starts with stability analysis of grid-connected voltage source converters (VSCs), where different methods are used to assess the stability of the grid-connected VSC. An energy function-based method and an inertia-based method are used to analyze the stability of grid-tied VSC. Besides, it is tried to assess the large-signal stability of the phase-locked loop (PLL) as one of the most important control loops in most PE-based units.

Stability assessment of large-scale power systems with PE-based energy sources is considered as the next step in this project. To do so, 4-machine Kundur and 23-machine Nordic test systems are considered as the small-scale and the large-scale power systems, respectively. The large-signal stability assessment is done to demonstrate stability challenges of modern power systems with a high penetration of PE-based energy sources. Thereafter, the large-signal stability challenges of modern power systems is considered, where inertia-based assessment is used to analyze the transient stability of PE-based power systems. The last part of this project gives a solution to enhance the large-signal stability of modern power systems. Regarding the large-signal stability assessment of PE-based power systems, it is concluded that the distribution of PE-based energy sources affects the grid transient stability, and it can be assessed based on the grid inertial response.

Dansk resume

Med en stigende andel af vedvarende energikilder som værende del af det moderne elnet ændres omfanget af stabilitet, sikkerhed, pålidelighed og beskyttelses evalueringen af det konventionelle elnet. I det moderne elnet, hvor der indgår en stor andel effektelektronisk baseret energikilder kan stabilitetsproblemer lede til udfald af generationsenheder og endda mørklægning af systemet. Derfor er det vigtigt at evaluere stabilitets udfordringerne af det effektelektroniske baseret elnet for at undgå uønsket effekter. I dette projekt evalueres stabilitets udfordringerne i elnettet med stor fokus på modellering under større transiente forstyrrelser. Projektet indledes med stabilitets analyse af netforbundet spændingskilde konvertere, hvor forskellige metoder anvendes til at evaluere stabiliteten, der anvendes en metode baseret på en energi-funktion og en metode baseret på en inerti-funktion. Derudover evalueres stabiliteten ved større transiente forstyrrelser af fasesynkroniseringsenheden, som udgør en af de vigtigste kontrolsløjfer i et effektelektronisk baseret elnet.

Stabilitets evaluering af stor-skala elnet som er baseret på vedvarende energikilder, som værende det næste skridt i projektet, hvor to respektive elnet med henholdsvis 4 og 23 generationsenheder er taget i betragtning. Evalueringen af større transiente forstyrrelser udføres for at påpege stabilitets udfordringerne ved elnet med en stor andel af vedvarende energikilder. Efterfølgende er stabilitets udfordringerne under større transiente forstyrrelser betragtet, hvor inerti-baseret evalueringer anvendes til at analysere den transiente stabilitet. Under projektets afsluttende del fremføres en løsning til at forbedre stabiliteten af det moderne elnet under større transiente forstyrrelser. Med henblik på evalueringen af det moderne elnets stabilitet under større transiente forstyrrelser, kan det konkluderes at fordelingen af vedvarende energikilder har en indflydelse på den transiente stabilitet, og som kan evalueres på baggrund af nettets inertielle respons.

Table of contents

Thesis Details

Thesis Title:	Modeling and Control of Large-Signal Stability in Power Electronic-based Power Systems
Ph.D. Student:	Bahram Shakerighadi
Supervisors:	Prof. Frede Blaabjerg Prof. Claus Leth Bak Dr. Esmaeil Ebrahimzadeh

The main body of the this thesis consists of the following papers:

Publications in Refereed Journals

J1. **B. Shakerighadi**, E. Ebrahimzadeh, F. Blaabjerg, and C. L. Bak, ‘‘Large-signal stability modeling for the grid-connected VSC based on the Lyapunov method,’’ in Energies, vol. 11, p. 2533, Oct. 2018.

J2. **B. Shakerighadi**, E. Ebrahimzadeh, M. G. Taul, F. Blaabjerg and C. L. Bak, "Modeling and Adaptive Design of the SRF-PLL: Nonlinear Time-Varying Framework," in IEEE Access, vol. 8, pp. 28635-28645, 2020.

J3. **B. Shakerighadi**, S. Peyghami, E. Ebrahimzadeh, M. G. Taul, F. Blaabjerg and C. L. Bak, " A New Guideline for Security Assessment of Power Systems with a High Penetration of Wind Turbines," in Appl. Sci., 2020, 10, 3190.

Publications in Refereed Conferences

C1. **B. Shakerighadi**, E. Ebrahimzadeh, F. Blaabjerg and C. L. Bak, "Lyapunov- and Eigenvalue-based Stability Assessment of the Grid-connected Voltage Source Converter," 2018 IEEE International Power Electronics and Application Conference and Exposition (PEAC), Shenzhen, 2018, pp. 1-6.

C2. **B. Shakerighadi**, E. Ebrahimzadeh, C. L. Bak and F. Blaabjerg, " Large Signal Stability Assessment of the Voltage Source Converter Connected to a Weak Grid," Proceedings of Cigre Symposium Aalborg 2019, 2019, pp. 1-12.

C3. **B. Shakerighadi**, S. Peyghami, E. Ebrahimzadeh, F. Blaabjerg and C. L. Bak, "Security Analysis of Power Electronic-based Power Systems," IECON 2019 - 45th Annual Conference of the IEEE Industrial Electronics Society, Lisbon, Portugal, 2019, pp. 4933-4937.

C4. **B. Shakerighadi**, E. Ebrahimzadeh, F. Blaabjerg and C. L. Bak, "Large Signal Stability Assessment of the Grid-Connected Converters based on its Inertia," 2019 21st European Conference on Power Electronics and Applications (EPE '19 ECCE Europe), Genova, Italy, 2019, pp. 1-7.

This dissertation has been submitted for assessment in partial fulfilment of the Ph.D. degree. The thesis is a summary of the outcome from the Ph.D. project, which is documented based on the above publications. Parts of the results are used directly or indirectly in the extended summary of the thesis. The co-author statements have been made available to the assessment committee and are also available at the Faculty of Engineering and Science, Aalborg University.

Bahram Shakerighadi

Aalborg University, July 24, 2020

Preface

This dissertation is a summary of the outcomes of the Ph.D. work entitled: “Modeling and control of large-signal stability in power electronic-based power systems”, which was carried out at the Department of Energy Technology, Aalborg University, Denmark. The Aalborg University supports this Ph.D. project. The author would like to give an acknowledgment to the above-mentioned institution.

Foremost, I would like to begin by expressing my sincere gratitude and appreciation to my supervisor Professor Frede Blaabjerg, for his continuous guidance, motivation, and patience throughout the entire Ph.D. study. His guidance helped me in all the time of research and writing of this thesis. I would also like to extend my deepest gratitude to my co-supervisors Professor Claus Leth Bak and Dr. Esmaeil Ebrahimzadeh for their guidance and help during the entire period of the Ph.D. project. It has been such a great experience to work under your supervision.

I am also grateful to Dr. Nicklas Johansson for providing me an opportunity to visit ABB Corporate Research, Sweden, during my study abroad and broaden my knowledge in the area of stability assessment of power-electronic-based power systems.

Finally yet importantly, I would like to express my gratitude to my family for their continuous support, encouragement and for always being there for me. None of this would have been possible without you.

Bahram Shakerighadi

Aalborg University, July 24, 2020

Part I
Report

Chapter 1.
Introduction

1.1. Background and Motivation

During the last decades, the structure of power systems has been changed from conventional centralized systems with large-scale power generations to the modern distributed ones with many smaller scale distributed generations (DGs) systems; see Fig. 1.1 [1]. Most DGs are connected to the power systems by an inverter that makes them power-electronic-based (PE-based) units [2]. Nowadays, modern power systems with a high penetration of PE-based units, such as wind turbines and photovoltaics, are facing different challenges regarding their stability, reliability, security, protection, etc. [3]–[6].

The penetration of power PE-based energy sources, such as wind turbines and photovoltaics, are increasing dramatically in power system grids as shown in Fig. 1.2. By increasing the penetration level of PE-based units in power systems, different stability challenges, such as harmonics, small-signal stability, and large- signal stability, are changed [3], [7]. The main characteristics of the modern power systems that distinguish them from the conventional ones are the following:

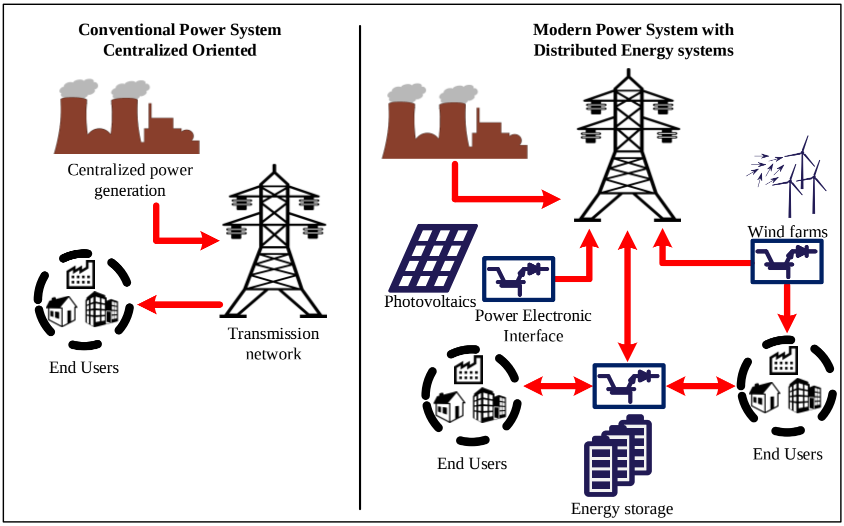

Fig. 1.1: Representation of a conventional power system (left). vs. a modern power electronic-based power system (right).

- Modern power systems with a high penetration of PE-based units introduce less inertial response in comparison with the conventional ones. This is due to the lack of physical inertial response from PE-based units, such as wind turbine and photovoltaics [7], [8].
- PE-based units are synchronized with the rest of the system by using a synchronization unit. This feature makes PE-based units distinguished from the conventional energy sources, which are mostly based on the synchronous generators (SGs). In SGs, the rotor's speed is coupled with the system frequency considering a swing equation relationship. In PE-based units, the frequency is decoupled from the main grid, and a synchronization unit like the phase-locked loop (PLL) is needed to measure the system frequency/phase [9]. The frequency/phase measured by the PLL can be used for the PE-based unit's control system. However, its performance has a strong impact on the stability of the system.
- There are some limits for PE-based units operation, due to their sensitivity to over-current and their ability to deal with the fault ride-through (FRT) condition, e.g. in case of a short circuit in the grid. These limits lead to some circumstances that make stability assessment of PE-based power system different from the conventional one.

With all this in mind, system operators are facing grid challenges, e.g. the frequency control under a high penetration of non-synchronous generation (NSG) [10]. Therefore, countries such as Ireland and U.K that have a relative small size and limited interconnection with other grids, have introduced new services demand in order to

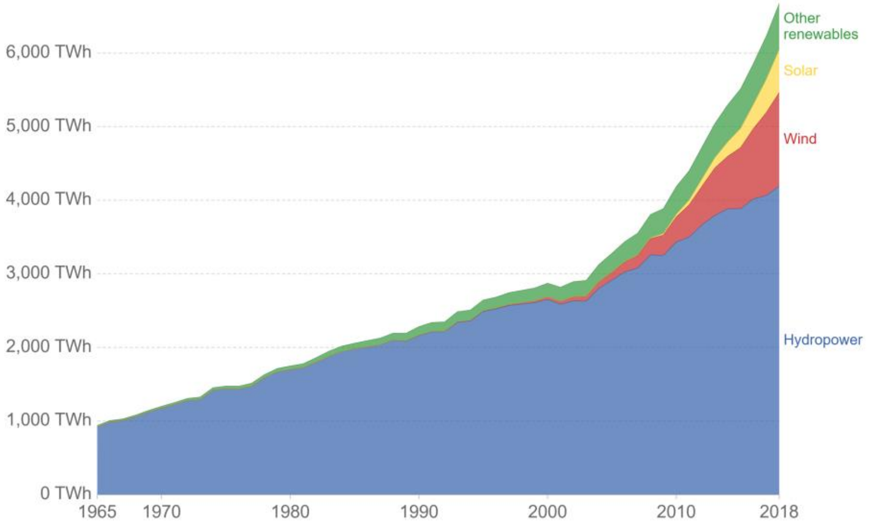

Fig. 1.2: Renewable energy generation in the world, 1965 to 2018 [11].

meet relevant challenges e.g. limited high rate-of-change-of-frequency (ROCOF) (>0.5 Hz/s) [12]. For instance, a framework is designed to evaluate the system inertia trend to indicate the risk of too high ROCOF in U.K. for a future “Go Green” scenario [13].

Besides ROCOF, other frequency related challenges are introduced by the unbalance between loads and generation in systems with a high penetration of NSG, which are frequency response to large disturbances, voltage dip that leads to frequency dips, frequency regulation and coping with its fluctuations, as well as over-frequency generation shedding [10]. From a time-scale point of view, stability challenges introduced in power grids can be categorized as it is shown in **Fig. 1.3**, where the highlighted part indicates different stability challenges including both the small-signal and large-signal stability phenomenon, and it is of interest in this project. The time-scale related to the PE-based units control ranges from a few microseconds to several milliseconds. Therefore, in can be said that the stability assessment of power-electronic based power systems includes a wide range of time scale [14].

The topic of the small-signal stability assessment of PE-based power systems has been well-studied in the literature [15]–[17]. The first step in small-signal stability analysis, and generally in all stability studies, is to model the system in an appropriate way to enable small-signal stability analysis [18].

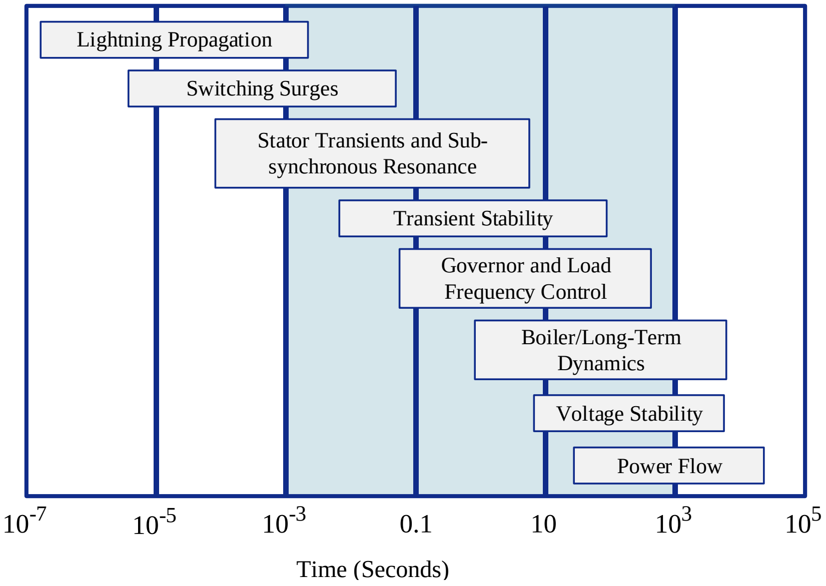

Fig. 1.3: Stability challenges and phenomenon in of power grids illustrated in terms of time scale [19].

In small-signal stability analysis, it is tried to linearize the power system equations. This makes the system model arranged in a way that it can be assessed by linear stability analysis techniques [20]. Regarding techniques for small-signal stability analysis, bode plot, eigenvalue analysis, and Nyquist criterion are straightforward to use and here most of the controllers are designed based on that. However, it might be a challenging issue to use the aforementioned techniques for a large-scale power system [21]. The small-signal stability may not be credible when the system is subjected to a large disturbance, due to the linearization techniques which are used, are not valid any more [22]. In order to analyze the stability of the PE-based power systems (and generally complex nonlinear systems), large-signal stability assessment techniques should be used [23]–[26].

Large-signal stability of power systems is defined as the power system ability to maintain stable when it is subjected to a large disturbance [27]. In other words, when a large disturbance such as the generation trip or a three-phase fault happens in the system, different stability criteria should be studied, and if the system can maintain within its stability boundaries, then it can be said that the system is stable from a large-signal stability point of view. Generally, there are three main categories of stability that should be checked for when a large disturbance happens in the system: rotor angle stability, frequency stability, and voltage stability. Mostly, each of the aforementioned stability categories is analyzed separately; however, large disturbances may cause two or three of stability challenges, instantly [28]. Most often, the large-signal stability is related to transient stability. A large-signal stability time frame is usually 3 to 5 seconds; however, it may be extended up to 10 to 20 seconds, e.g. for frequency stability assessment of the large-scale power systems.

In order to assess the large-signal stability assessment methods of PE-based power systems (and generally complex nonlinear systems), the nonlinear terms are not linearized, which makes the assessment complicated. There are some concepts that are used regarding the large-signal stability analysis of PE-based power systems, such as the Lyapunov theory (energy function theory) and equal area criterion [29], [30]. The main challenge for large-signal stability assessment techniques that are based on the Lyapunov function is that there is no straightforward method to define the energy function of a system. Therefore, it is a challenge to define an appropriate Lyapunov function that indicates system stability boundaries [22].

In order to assess the large-signal stability of PE-based power systems, the first step is to model the system in an appropriate way (like in the small-signal stability assessment). The modeling of the PE-based power system could be varied based on the focus of the study. For instance, if the main focus of the study is the stability of the PE-based unit, then the rest of the system can typically be modeled as a stiff voltage source or a simple voltage source and an impedance [31], [32]. On the other hand, if the main focus of the study is the stability of the power system rather than the PE-based unit, then a simple model for the PE-based unit might be used [33], [34]. However, a detailed model of the grid including all its components' models introduces a more realistic behavior of the system. After modeling the system, the next step is to design controllers based on the stability assessment. However, it should be noticed that most often the small-signal stability assessment is used for tuning the controllers, even for large-signal stability case studies, e.g. in FRT case study [35], [36].

The large-signal stability assessment becomes more important as the penetration of non-synchronous generators (NSGs) are increasing in power systems. By increasing the penetration of NSGs, the main system becomes more vulnerable to large disturbances, due to NSGs' lack of inertial response [37], [38]. In this way, the main grid's ability to control the system frequency and bus voltage magnitude become less compared to the stiff grid. Grids with less ability to control the system variables, such as voltage magnitude of buses and the system frequency, are called weak grids [39]–[41]. This definition of the weak grid is translated to “a voltage source connected to a large impedance” in grid-tied VSC stability assessment [40], or a large-scale power system with a low inertial response [42]. In some cases, the increase of NSG penetration in power systems may even lead to blackouts.

In this project, the stability assessment methods of PE-based power systems are studied. What is mainly motivates the author to focus on this topic is that renewable energy sources (RESs) inevitably increase the penetration in power systems, and most of them are connected via a PE interface, called an inverter. The literature regarding the modeling and stability assessment of such systems are mainly focusing on the small-signal stability. However, small-signal stability analysis is not accurate in case of a large-disturbance. Therefore, in this project, it is tried to introduce an insight regarding the large-signal stability analysis of modern power systems.

1.2. Power System Stability

Power system stability has been a challenging issue for electrical grids for many decades [27]. The stability assessment of power systems has been studied extensively in the literature. The stability of power systems is categorized into three main topics as discussed before: rotor angle stability, frequency stability, and voltage stability, as shown in Fig. 1.4. All of the three categories of the power systems stability are divided into some subcategories based on their causes (disturbance size) and their time scale [43].

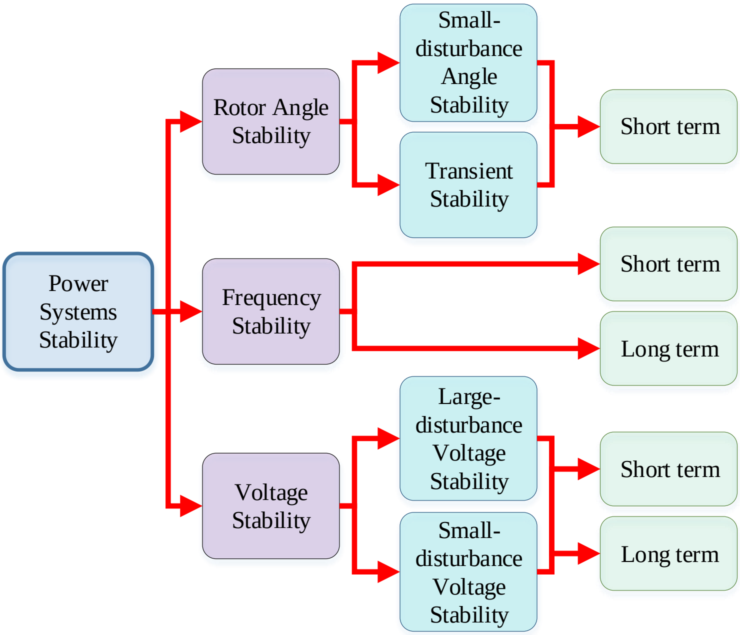

Fig. 1.4: Classical power system stability classification [27].

Most of the large disturbances in power systems, such as a three-phase short circuit fault, lead to short-term instabilities, which is a 3-5 s time scale phenomenon in order to recover [27]. However, the system scale might be affected by the time scale of an event. For instance, the period for transient stability may be extended to 10-20 s for very large-scale power systems.

In PE-based units, there is no physical rotational part that is synchronized with the rest of the grid. This makes the rotor angle stability out of scope for the PE-based units' stability studies. On the other hand, PE-based units are coupled to the rest of the system from the frequency point of view, as it is utilizing an inverter. Most often, a PLL is used for the synchronization of a PE-based unit and the rest of the system. To study the frequency stability of the PE-based units, the impact of PLL on its stability should be considered as an important part. In this way, the frequency stability of PE-based power systems is different from the conventional one. For power systems with a high penetration of NSGs, the stability definition should be slightly different from its definition for the conventional one or should be an expanded version of it.

A general guideline of PE-based power systems stability definition is discussed in [44]. Although this guideline is developed for Microgrids, its definition can be used for different PE-based power systems. It should be noticed that to apply such a guideline to large-scale power systems with a high penetration of NSGs, the relevant grid codes should be considered as well [45], [46]. As mentioned earlier, there is no rotational part in PE-based units. Therefore, only the voltage stability and the frequency stability are considered for PE-based units. However, the PE-based power systems will typically include both conventional and modern types of energy sources, which means that the conventional synchronous generators are still used as a part of the modern power systems. The new guideline for PE-based power systems stability introduced in [44], is shown in Fig. 1.5, where it can be seen in that PE-based power systems stability assessment is categorized more in details for the conventional systems (due to the introduction of more stability phenomenon by PE-based units), yet conventional stability subcategories, such as voltage stability, frequency stability, and rotor angle stability (electric machine stability), are kept like in the former one (PE-based power systems stability assessment). The disturbance size (large and small disturbances) and the time frame of the event are still used for distinguishing the different kinds of instability issues for the PE-based power systems, as well as for the conventional power systems.

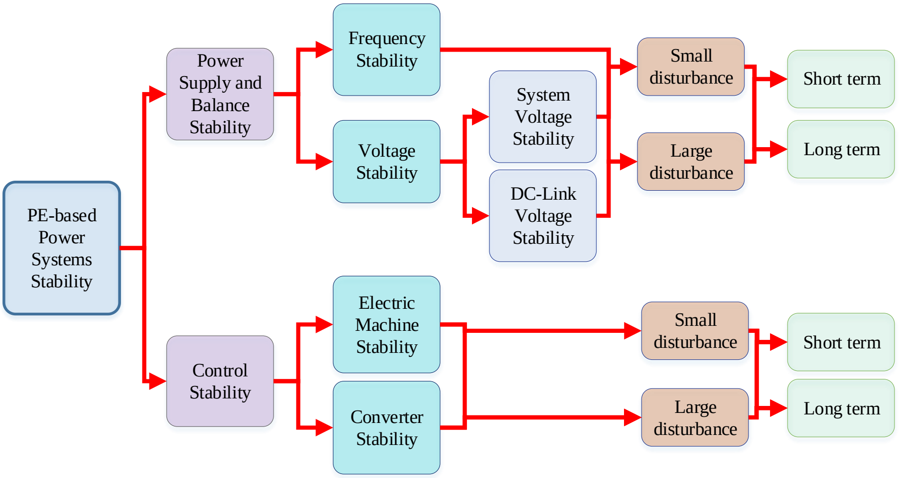

Fig. 1.5: Power electronic-based power systems stability classification [44].

It should also be noticed that in small-scale PE-based power systems, the systems variables (frequency and voltage) are strongly coupled [44]. The reason is that resistance to inductance ratio (R/X) is higher in small-scale power systems compared with the large-scale systems. This leads to a coupling between active and reactive power that are typically decoupled in the conventional power systems [47]. Therefore, an event that triggers the frequency instability may lead to the voltage instability as well. However, by increasing the scale of the system (by decreasing R/X ratio), e.g. in a large-scale power system such as in the Nordic-32 test system [48], the frequency stability and the voltage stability phenomenon can be distinguished easier than the small-scale ones [49].

Another issue regarding the PE-based power systems stability classification is the control stability category, as also shown in Fig. 1.5. This category is related to the control loops of the synchronous machines and NSGs, LCL filters (which are the output filter of the converters), and PLLs. Poor controller tuning, PLL bandwidth, system synchronization failure, harmonic instability, etc., may lead to system instability caused by the control system of NSGs (inverters), which is going to be discussed in the next paragraphs.

1.3. Voltage Source Converters

As it is mentioned before, one of the key components of PE-based power systems is voltage source converters (VSCs), which is used for RESs that are connected to the rest of the system via an interface, called the inverter. Although different control strategies are defined for VSCs, which will be discussed in Section 1.3.1, the main application of the VSCs is to transfer the energy produced by the renewable source to the power system having an appropriate voltage level and frequency. A single-phase diagram of a grid-tied VSC is shown in Fig. 1.6. Z_c and Z_g are the VSC output filter and the grid impedance, respectively. The main grid is presented as an infinite bus, which is a stiff voltage source and grid impedance. Regarding the infinite bus used in the main grid, it is assumed that $\vec{v}_g$ has a fixed magnitude and phase angle. PCC shown in Fig. 1.6 indicates the point of common coupling. In general, VSCs are used in two main modes: grid-tied mode and islanded mode [50]. The control systems of VSCs are designed and are tuned based on their applications and operation modes.

VSCs are used in the islanded mode when there is a difficulty to be connected to the main grid or due to some special circumstances [51], [52]. An application of islanded mode of VSC could be a situation that a fault occurs in the system and a part of the grid needs to work in an isolated mode. In this case, a part of the system will be disconnected from the rest of the system, and then the separated part works independently. Also, islanded mode of VSCs can be used in shipboard power systems and also other autonomous systems [52]. However, most often, VSCs are operated in their grid-tied mode in PE-based power systems.

1.3.1. Classification of the Grid-Tied VSC

Based on the specific application and the VSC's configuration, there are four main control structures of grid-tied VSCs: grid-forming, grid-feeding, current-source-based grid-supporting, and voltage-source-based grid-supporting. The schematics of these four categories are shown in Fig. 1.7. In Fig. 1.7(a), E^* and ω^* are the voltage magnitude and frequency references, respectively. By using E^* and ω^*, the reference voltage, $\mathbf{v}^*$, will be generated. In Fig. 1.7(b), P^* and Q^* are the active and reactive power references, respectively, which are used to generate the reference value for the current, $\mathbf{i}^*$. In Fig. 1.7(c) and In Fig. 1.7(d), $E^*, \omega^*, P^*,$ and Q^* are used to indicate the modified values for active (P^{**}) and reactive (Q^{**}) power.

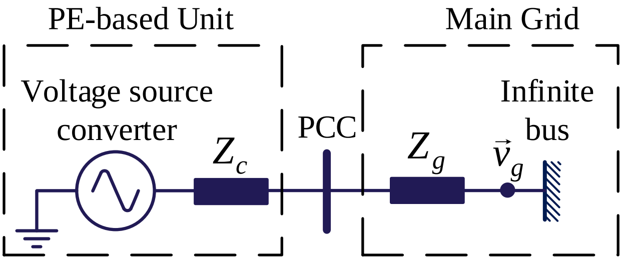

Fig. 1.6: A single-phase diagram of a grid-tied voltage source converter (VSC).

1.3.1.1 Grid-Forming Power Converters

The grid-forming power converters are designed and operated, so they represent a voltage source; see Fig. 1.7(a). The main application of the grid-forming power converters is to act like a synchronous machine. In this way, a grid-forming power converter introduces a voltage magnitude and frequency at its point of common coupling (PCC) with the rest of the grid. In the case of islanding mode for a part of the grid in which there are only PE-based energy sources, at least one grid-forming power converter is needed to form the system reference, so the other converters can be synchronized with the grid-forming power converter. A schematic block diagram of the grid-forming power converter is shown in Fig. 1.8.

Two of the main applications of grid-forming power converters is for energy storage and uninterruptable power supplies (UPSs) [53]. What can be achieved from the grid-forming power converters is also the ability to introduce inertial response [54].

The general from of the grid forming power converter is shown in Fig. 1.7(a), and the grid-forming power converter model shown in Fig. 1.8 is just a kind of grid-forming power converters. Any other control model for power converters that presents a voltage source with a magnitude and the phase angle can be named a grid forming power converter. In this regard, an interesting model implemented for the grid-forming power converters is the virtual synchronous machine model (VSM) used for the inverter control [55]. In the VSM model, it is tried to mimic the behavior of the synchronous machine. The VSM control model of the VSC is to use it to control the voltage magnitude and angle at the PCC and bring an inertial response to the active power generation and consumption unbalance. The frequency of the VSC is coupled into the VSM control. Controlling the PCC voltage angle is the same as controlling the frequency. In this way, like in synchronous machines, if the system frequency drops, the VSC injects more active power to compensate for the active power consumption. This can be done by implementing the swing equation into the active power control loop of the VSC. It is worth mentioning that in VSM control method, there is no need to use a PLL to estimate the phase angle and the system frequency in normal condition. However, the PLL might be used when the current limitation is activated [56].

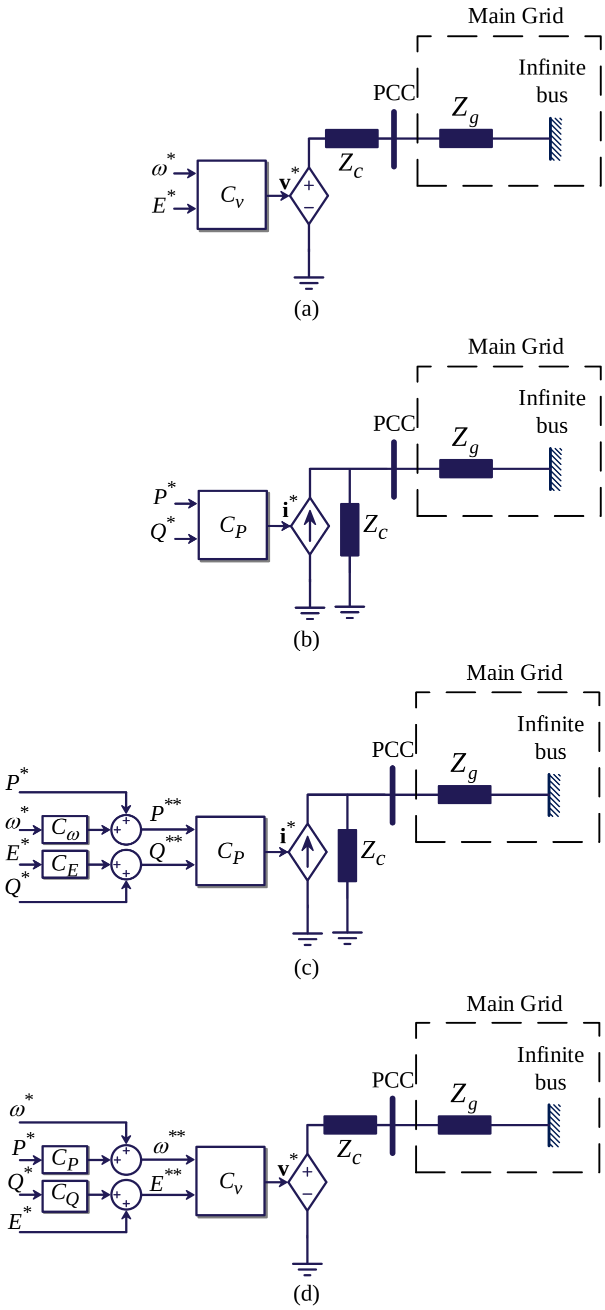

Fig. 1.7: Block-diagrams of grid-tied VSCs. (a) grid-forming, (b) grid-feeding, (c) current-source-based grid-supporting, and (d) voltage-source-based grid-supporting [57].

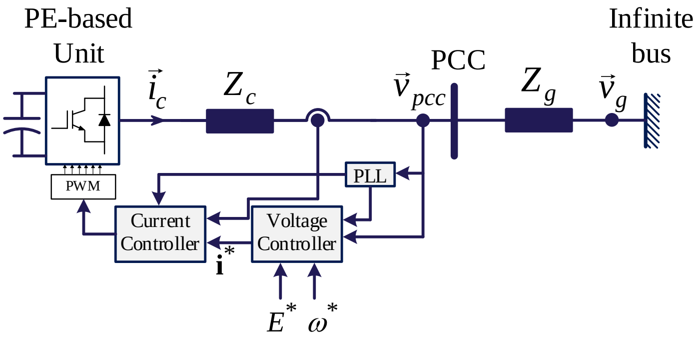

Fig. 1.8: A schematic block diagram of the grid-forming power converter [57].

1.3.1.2 Grid-Feeding Power Converters

In grid-feeding power control, the main goal is to inject the desired active and reactive power to the system. In this type of control, it is assumed that the PCC voltage magnitude and the system frequency are controlled by the grid side. This means that the only necessary controller in grid-feeding power converters is the current controller. However, other outer loop controllers such as active and reactive power controllers may be added to the control loop. In addition, a PLL is used to extract the PCC voltage angle and frequency in order to change the controller frame from *abc* to *dq*-frame and thereby keep the converter synchronized with the main grid. It should be mentioned that the controller can be designed in other coordinate systems, like the *αβ*-frame. A schematic block diagram of the grid-feeding power converter is shown in Fig. 1.9.

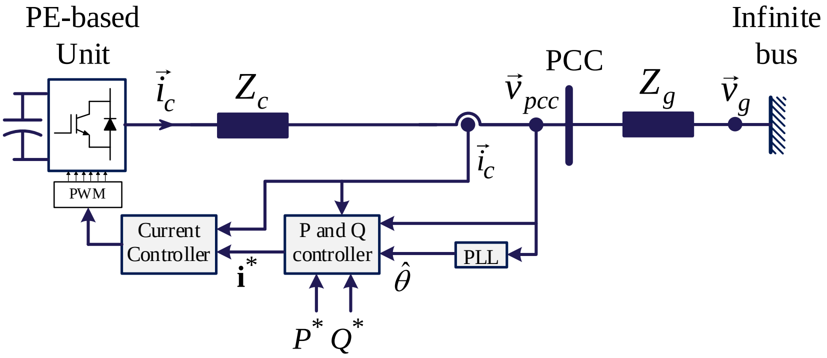

Fig. 1.9: Schematic block diagram of the grid-feeding power converter [57].

In grid-feeding power converters, it is assumed that the voltage and frequency of the PCC is controlled by the main grid side. The problem with the grid-feeding power converters is that when the number of grid-feeding power converters increases in the power system, the main system becomes weaker, and a weak grid is less able to control the system variables compared with a stiff grid. In this way, as the grid-feeding power converters control relies on the system stiffness, the VSC in grid-feeding control mode may become out of synchronization when it is connected to a weak grid [58].

1.3.1.3 Current-source-based grid-supporting

This type of controller of the VSC is very similar to the grid-feeding power converter control. The main goal is to inject active and reactive power assuming that the main grid controls the PCC voltage magnitude, voltage phase, and the system frequency. The difference between the current-source-based grid-supporting and the grid-feeding power converter is the droop control introduced in the current-source-based grid supporting converters. This is shown in Fig. 1.10.

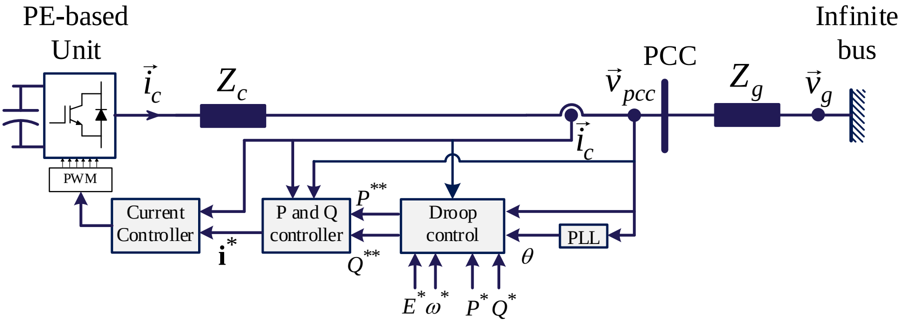

Fig. 1.10: Schematic block diagram of the current-source-based grid-supporting power converter with additional droop control [57].

In this way, it can be said that the current-source-based grid-supporting control model is an advanced version of the grid-feeding control model for the power converter.

1.3.1.4 Voltage-source-based grid-supporting

The voltage-source-based grid-supporting control mode of power converters is the modified version of the grid-forming power converters. An outer control loop for the active and reactive power is added to the grid-forming power converters controller, as shown in Fig. 1.11.

In this way, voltage-source-based grid-supporting power converters act similar to a synchronous generator [55]. In this control scheme, the active and reactive power injected into the system is dependent on the PCC voltage, $\vec{v}_{pcc}$, the grid side impedance, and the grid voltage [59]. In respect to the active and reactive power control, the idea of the droop control can be used in order to mimic the behavior of a synchronous generator. By using the droop control for the active and reactive power regulation, the active power delivered to the system decreases when the grid frequency increases, and also the reactive power decreases when the PCC voltage increases [57]. By increasing the penetration of PE-based energy sources in the power system, the frequency stability will be supported due to the inertial support of the voltage-source-based grid-supporting power converters.

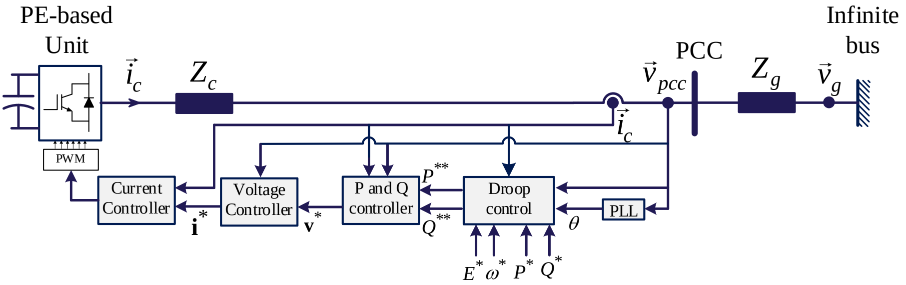

Fig. 1.11: Schematic block diagram of the voltage-source-based grid-supporting power converter [57].

1.3.1.5 The use of different grid-tied VSC in power systems

Based on the system requirement and the capability of the PE-based energy sources, each control method mentioned earlier has some applications. The grid-feeding power converters are used to set the active and reactive power reference, so e.g. the maximum power point tracking (MPPT) algorithms can be implemented for different energy sources, e.g. photovoltaics and wind turbines [60].

Grid-supporting converters may introduce different services, such as the frequency support and reactive power injection both in normal operation and during a fault, to the system. Compared with the conventional synchronous generator, the grid-supporting converters are able to act faster. However, it should be noticed that the grid-supporting converters' performance are very dependent on their energy source type and size [57], [61].

It seems that the future of the power grids is dependent on how to control the PE-based energy sources as the grid-forming power converter, and the increasing of the penetration of grid-feeding power converters may cause stability issues for the grid [53]. In this way, power converters should be able to support the system with damping power oscillations in addition to the voltage and frequency regulation [62]. Power converters should also be able to provide black-start services for the grid [57]. For this, a general guideline for using the NSGs in power systems is provided in [63].

1.3.2. Stability Challenges of the Grid-Tied VSC

In this part, it is tried to discuss different stability challenges introduced by the grid-tied VSC for the power systems. To do so, the impact of grid-tied VSC on the different systems stability categories and the grid-tied VSC stability challenges are discussed.

1.3.2.1 Grid-tied VSC Stability: Small-signal stability challenges

Considering the modeling of the grid-tied VSC, different stability challenges, such as the PWM delay impact, tuning the PLL, and the grid stiffness (stiff grid or weak grid), are contributions to some of the grid-tied VSC stability issues. In this part, the importance of different stability challenges introduced by the control system of the VSC with the grid-feeding control configuration is discussed. A more detailed discussion is done in Chapter 2. In order to do so, small-signal stability is an important issue. To assess the small-signal stability of the grid-tied VSC, an s-domain model of the controller and the system can be used. An example of the grid-feeding VSC model in the s-domain with a current and active power controller like shown in Fig. 1.12(a). Besides, the small-signal model of the PLL is shown in Fig. 1.12 (b). It should be noticed that the PCC voltage and the VSC output current are $\vec{v}_c = v_d + v_q j$ and $\vec{\imath}_c = i_d + i_q j$, respectively, while the reference values for the PCC voltage and the VSC output current are $\vec{v}_c{}^* = v_d{}^* + v_q{}^* j$ and $\vec{\imath}_c{}^* = i_d{}^* + i_q{}^* j$, respectively.

In this model, the delay caused by the pulse-width modulation (PWM) is presented by its *Padé* approximation [64]. The PWM delay model equals $e^{-T_d s}$, where T_d is the time delay introduced by the switching; however, this is a non-linear term. To present the delay in the small-signal stability model, the *Padé* approximation of the delay is presented in the following to linearize the PWM delay model:

$$e^{-T_d s} = \frac{1-0.5T_d s}{1+0.5T_d s} \tag{1.1}$$

This is an example on how the non-linear terms are linearized for small-signal stability assessment. The *Padé* approximation introduces an appropriate approximation of the delay for the small-signal analysis. However, such linearization is not credible for the large-signal stability assessment.

In addition, the PLL is a non-linear feedback control unit and it has many variants in implementation. To use it for the small-signal stability assessment, the linearized format of the PLL can be used [9]. The Synchronous Rotation Frame-PLL (SRF-PLL) is often used for the synchronization and its small-signal model is a second-order transfer function, as given by:

$$G_{PLL}\left(s\right)=\frac{\left(v_d K_{p,pll}\right)s+\left(v_d K_{i,pll}\right)}{s^2+\left(v_d K_{p,pll}\right)s+\left(v_d K_{i,pll}\right)} \tag{1.2}$$

where $K_{p,pll}$ and $K_{i,pll}$ are the proportional and integral gains of the PI control used in Fig. 1.12. It should be noticed that the PLL's response when the system is subjected to a large disturbance can be analyzed by different non-linear stability assessment methods [J3].

In this case, the grid side model shown in Fig. 1.9 is not considered in the model presented in Fig. 1.12. In fact, it is assumed that the grid is a stiff voltage source with $Z_g = 0$. This assumption is not always correct, due to the grid model may be presented as a voltage source and an impedance. It should be noticed that although this model does not present the exact behavior of the grid, the voltage source and the impedance brings a good approximation of it.

Regarding the output current of the grid-feeding power converter, it is limited by the grid voltage and its impedance. The limitation of the output current of the grid-tied VSC based on the grid characteristic is given as follows [65]:

$$\left|\vec{i}_c\right| \le \frac{\left|\vec{v}_g\right|}{\left|Z_g\right|} \tag{1.3}$$

where $\left|\vec{v}_g\right|$ is the grid voltage magnitude and $\left|Z_g\right|$is the grid impedance magnitude. $|\vec{\imath}_c|$ is the grid-tied VSC output current magnitude. The system stability margin can be detected by (1.3). The weaker grid has a larger value of $\left|Z_g\right|$. By increasing the grid impedance, the maximum VSC output current $\left(\left|\vec{v}_g\right|/\left|Z_g\right|\right)$ decreases, and for a certain output current reference, $\vec{\imath}_c^*$, the grid-tied VSC may become unstable [65].

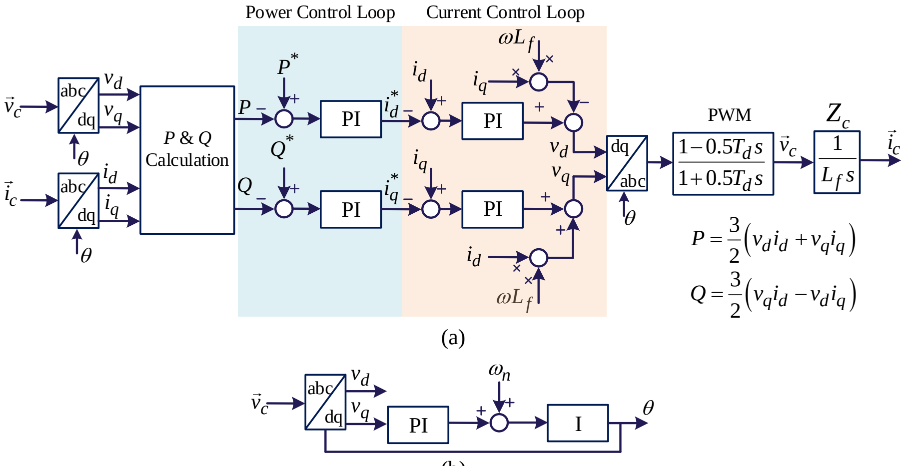

(a)

(b)

Fig. 1.12: Small-signal model of (a) the grid-feeding power converter including the current control and active power controllers and (b) the SRF-PLL [57]. Basic system is shown in Fig. 1.9.

Apart from the grid impedance impact on the system stability, the VSC control system parameters can affect the stability margin. For instance, the PLL parameters, which determine the PLL bandwidth, can affect the system stability. As a rule of thumb, a higher bandwidth for the control system represents a faster yet more vulnerable controller. With this in mind, by increasing the PLL bandwidth, the PLL can track the PCC voltage phase angle faster, which is a desired action. However, this makes the system more vulnerable to fluctuations. In addition, it is worth mentioning that an outer controller (such as the PLL and active and reactive power control loops) should be slower than the inner controller (such as the current controller). As a rule of thumb, the outer controller should be ten times slower than the inner controller in order to avoid the dynamic coupling between them [66].

If the grid-tied VSC becomes unstable as discussed in Section 1.3.2, e.g. its current reference is set higher than the maximum current limit, then it may be disconnected from the rest of the system, or it could also just keep the current fixed to the maximum limit. The case that the VSC is disconnected from the rest of the system can be translated into the loss of generation for the transmission systems operators (TSOs). Although a certain amount of loss of generation is tolerable from the TSOs point of view, a large PE-based disconnection may cause serious problems for the grid and affecting the frequency stability [67].

1.3.2.2 Grid-tied VSC Stability: Large-signal stability challenges

The transient response of the grid-tied VSC when it is subjected to a large disturbance can be analyzed based on its large-signal model. At this point, it is very important to distinguish between a large disturbance and a small one. A large disturbance is considered as an event that its impact on nonlinear terms of the dynamic model of the system cannot be omitted. For instance, considering x as a variable of a system $f(x,t)$. If the change in x is small enough, e.g. $\Delta x = 0.1$, then the change in a nonlinear term of x^2 can be omitted, as $\Delta x^2 = 0.01$ is considerably small. However, if the disturbance is large, e.g. $\Delta x = 2$, then the change in x^2 cannot be omitted from the dynamic model of $f(x,t)$, as $\Delta x^2 = 4$ is considerably large. A three-phase fault and a line trip is considered as large disturbances in the power system analysis.

As mentioned before, regarding the large-signal stability assessment of the grid-tied VSC considering its nonlinear characteristics, linear techniques such as Nyquist criterion and Bode plot analysis, cannot be used, due to these methods are useful for linear systems [68]. On the other hand, nonlinear stability assessment techniques, like the Lyapunov theory, provide a comprehensively good approach for the large-signal stability analysis of grid-tied VSCs [69]–[71]. Reference [69] is one of the first approaches that introduces the usage of the Lyapunov-based control method to guarantee the grid-tied VSCs large-signal stability, in which it is mentioned that linear techniques can only guarantee the system stability when it is subjected to a small perturbations from the operating points. In [70], a Lyapunov-based method is proposed to analyze the grid-tied VSC when it is subjected to a short-circuit fault, causing grid voltage dips. Considering the abovementioned discussion in mind, the Lyapunov-based methods are used in the stability assessment and control of the grid-tied VSCs [69], [72]. In this way, Chapter 2 is dedicated to introduce a large-signal model of the grid-tied VSC and analyze it by using different nonlinear stability techniques. However, it should be mentioned that the topic of large-signal stability assessment of the grid-tied VSC is not limited to the stability analysis of the grid-tied VSC itself, but it is also related to its impact on the main grid stability. Two main impacts of a single grid-tied VSC on the grid stability are the system frequency stability and the grid voltage stability as discussed below.

Grid-tied VSC Impact on the System Frequency Stability

One of the main impacts of grid-tied VSC on the systems stability is the reduction of overall system inertia [42]. There are three frequency related criteria that are affected by increasing the NSG penetration in power systems: frequency nadir, the rate of change of frequency (ROCOF), and the steady-state frequency deviation, as shown in Fig. 1.13 [73]. The frequency nadir is the minimum value of the frequency reached after the system is subjected to a fault [28].

There is a specific range for the frequency deviation, ROCOF, and frequency nadir in every power system that is defined by grid codes [74]. By decreasing the system inertia, the ROCOF, and the frequency nadir will increase. This may lead to some instabilities or even it may lead to the act of some protection systems, which eventually leads to a blackout or islanding of a part of the grid.

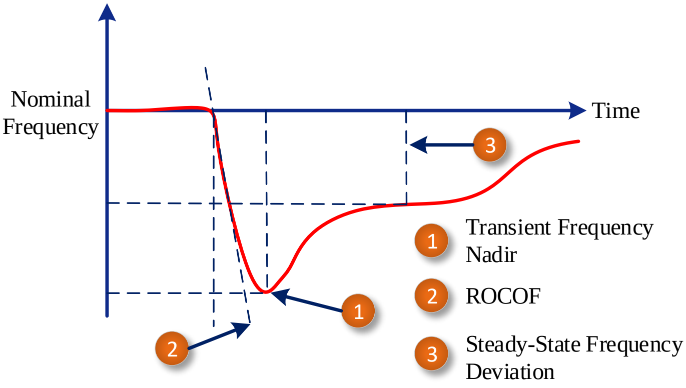

Fig. 1.13: Frequency response to a disturbance in the power system. ROCOF: Rate-of-change-of-frequency [7].

Grid-tied VSC Impact on the System Voltage Stability

Increasing the penetration of grid-tied VSCs has an impact on the voltage stability of the power systems. For instance, connecting photovoltaics at the far end of a low voltage feeder leads to an increase in the voltage magnitude at the PCC. This situation gets worse when the R/X ratio of the connecting line between the grid and the VSC is high. In this case, voltage magnitude becomes more sensitive to the active power. Therefore, when the active power is injected into the grid, the voltage magnitude rises at the PCC. This problem is called the voltage raise at the distribution system level [28], [75].

Another voltage stability problem caused by the increase of PE-based units in the system is the voltage drop. This happens when the reactive power required from the PE-based units cannot be supplied by them. Other voltage stability issues caused by the VSCs are voltage fluctuations and voltage control challenges, such as decentralized and centralized voltage control methods in the power grid [75].

1.4. Power-Electronic-based Power Systems

In this part, examples of some stability issues for PE-based power systems are discussed. After that, solutions to improve the stability of the system will be presented.

1.4.1. Stability Challenges of Modern Power Systems with High Penetration of PE-based Units- Historical Review

By increasing the penetration of NSGs in power systems, it becomes a more challenging issue to maintain system stability when the system is subjected to a disturbance. Stability challenges for some power systems with a high penetration of NSGs can lead to blackouts and a list of outages is presented in [76]. Some examples of them are discussed as follows.

An interesting case is the South Australia (SA) power grid [28]. A unique characteristic of SA power grid is that around 50% of the total demand in SA power grid is provided by NSGs, and synchronous generators provide less than 20% of the demand (the rest of the demand is provided by an interconnection system). Although the system runs in its stable mode for no-contingency condition (normal condition), some disturbances may cause stability issues, and may even lead the system into a blackout. For instance, on the 20th of September 2016, 52% of the wind generation was lost, due to a severe storm. The interconnection between SA and the rest of the Australian power system was not able to compensate for the lost generation. Therefore, the interconnection disconnected due to power flow overload. Consequently, the SA power grid collapsed and around 1.7 million people were affected with no power [76].

Different stability issues are needed to be discussed for this event. First, the buses where their stability are vulnerable to system fluctuations need to be identified by different system stability analysis methods. Then, different stability challenges, such as over-voltage issues after network separation, high ROCOF, under frequency load shedding (UFLS) malfunction due to high-frequency nadir, and frequency/voltage instability debate, need to be studied for the weak buses of the grid, and identify what the main causes of the instability are, which lead to the blackout. Based on the measured data during and after the event, it can be seen that the 20th of September 2016 blackout in SA power grid was the outcome of not a single stability issue but all the early mentioned stability issues. It is worth mentioning that by an early recognition of the network separation, the event could have been prevented from a blackout.

Another good example of the power system with high penetration of NSGs is considered in the Irish power system [77]. One of the interesting characteristics of the Irish power system is that it is a low inertia isolated electrical grid where its instantaneous NSG penetration can reach 100% of the power demand [78]. With this in mind, grid codes are defined for the Irish power system in the way that NSGs inject a certain reactive power during and after a fault [79]. Similar grid codes are also applied for other power systems with high a penetration of NSGs [80].

This unique characteristic of the Irish power system makes it vulnerable to system fluctuations. The uncertainty in its power generation, due to the probabilistic nature of the wind energy and photovoltaics, requires energy storage to be used in order to prevent frequency instability in the system [61], [81]. Because of the relatively small size of the Irish power system, high ROCOF (>0.5 Hz/s) is one of the main concerns of the operators [12]. Using different fast frequency response (FFR) solutions, such as using the energy storage at buses that are more vulnerable to the system fluctuations, is introduced in order to deal with a high ROCOF value, inertia enhancement, and frequency response to large disturbances [61]. However, the weak points of the system, which are sensitive to the disturbances, should be determined in advance.

1.4.2. PE-based Power Systems Stability Solutions

There are different solutions for compensating the lack of inertial response caused by increasing the penetration of NSGs in the systems. One of the promising solutions is to add a flexible generation to ensure a reserve capacity. Because of the stochastic nature of the renewable energy sources (RESs), by increasing the penetration of PE-based generations, electrical grids experience difficulties in how to define an appropriate reserve capacity [82]. To deal with this problem, a flexible reserve capacity concept is introduced by some researchers [82]–[84]. For instance, in [84], renewable energy sources, such as wind turbines, are used to participate in the markets by providing auxiliary services. However, to apply a flexible reserve capacity for electric grids, more financial support and dealing with a more complex calculation compared with the conventional reserve capacity calculation are needed.

Another solution is to connect the system to other grids via stronger interconnections [85]–[87]. This solution has some advantages and disadvantages. The main advantage of this solution is that the inertial response of the system will increase by connecting two grids together [85]. However, it should be noticed that the system dynamic response is heavily dependent on the technology used for the interconnection. For instance, if the high voltage direct current (HVDC) transmission lines are used for the interconnection, then the controller impact on the low-frequency electro-mechanical oscillations may affect the system stability [87].

As discussed in Section 1.4.1, one of the main solutions for stability challenges of PE-based power system is the usage of energy storage systems (ESS) [61], [88], [89], e.g. grid-scale ESS is introduced for frequency regulation service for power systems [88], [89]. In fact, ESS will introduce a new paradigm in frequency regulation services. Different grid-scale ESSs are flywheel, lithium-ion batteries, flow batteries, advanced lead-acid batteries, and super-capacitors. The power scale for the mentioned technologies are up to 50 MW and later even larger, and their time response are within few milliseconds [61]. Some challenges for ESS, such as the sizing, the placement of the ESS in the system, and the cost are also discussed in the literature [90]–[92].

Conventionally, there are three main frequency regulation services based on how fast the service is needed: primary frequency response (PFR), secondary frequency response (SFR), and the tertiary frequency response (TFR). In modern power systems with a low inertial response, a faster response for the generation/load balance is needed that is called fast frequency response (FFR). The FFR is what the ESS provides to the system. Although this service is known with different names, e.g. enhanced frequency response in the UK or fast frequency response of Ireland, they share the same mechanism.

1.5. Project Objectives and Limitation

1.5.1. Research Questions and Objectives

Keeping in mind the main goal of having a stable power system with a high penetration of PE-based units, and inherently a more vulnerable grid to system fluctuations, the main objective of this Ph.D. project can be defined as analyzing the transient stability of PE-based power systems. As a result, the following fundamental research question is considered:

- How to correctly assess the large-signal stability for PE-based power systems and its components?

Thus, subsequent research questions can be derived:

- By using the large-signal stability assessment techniques, how can a marginal point of stability for a grid-tied VSC, be determined?

- Considering a power system with a high penetration of grid-tied VSC, how does the PE-based unit affect the large-signal stability of the grid? In case that the PE-based units affect the grid stability, how can the marginal point of transient stability be determined?

Based on the above raised questions, the following objectives can be set for this Ph.D. project:

Development of the nonlinear-based method to analyze the grid-tied VSC large-signal stability

To address the large-signal stability assessment for grid-tied VSCs, an in-depth analysis of VSC's components impact on the system stability will be carried out in this Ph.D. project. The expected outcome of this assessment is to introduce a large-signal model of the grid-tied VSC based on its energy function. Moreover, the PLL large-signal behavior, as one of the most common components that is used to synchronize the VSC with the grid, is also expected to be explored.

Transient stability assessment of power systems with a high penetration of PE-based units

To address the concerns related to the large-signal stability of PE-based power system, a credible model of the grid that presents its transient behavior will be explored in this project. The main source of the instability for grids with a high penetration of PE-based units, which is their low system inertia, will be analyzed, and based on that, the grid's transient stability margin will be investigated.

1.5.2. Project Limitations

Several details affect the large-signal stability of whether grid-tied VSC or even the large-scale PE-based power systems. Regarding the grid-tied VSC stability, DC-link voltage control is not considered in this work; however, this may have impact on the system large-signal stability. Also, the grid model is assumed as a simplified voltage source with an impedance for the grid-tied VSC stability assessment. Moreover, this project is also focused on the grid-feeding power converters, while grid-forming power converters large-signal stability assessment is not considered.

Regarding the large-signal stability of the large-scale PE-based power systems, only a simple grid-feeding power converters are considered as the NSG units. However, it should be noticed that the PE-based units could also include different types of NSGs, such as photovoltaics and PE-based energy storage systems.

A very important feature used in NSGs control during a large disturbance, which is defined in grid codes, is their FRT capability. This is not considered specific in the analysis here; however, the modeling of such a control system can be done using the methods discussed in this project.

1.6. Thesis Outline

The outcome and results of the Ph.D. project is summarized in this Ph.D. thesis based on a collection of the papers published during the Ph.D. study. The document is structured into two main parts: *Report* and *selected publications*. The thesis structure is illustrated in Fig. 1.3, and providing a guideline for how the content in the Report is connected to the Publications. This Ph.D. thesis has four chapters.

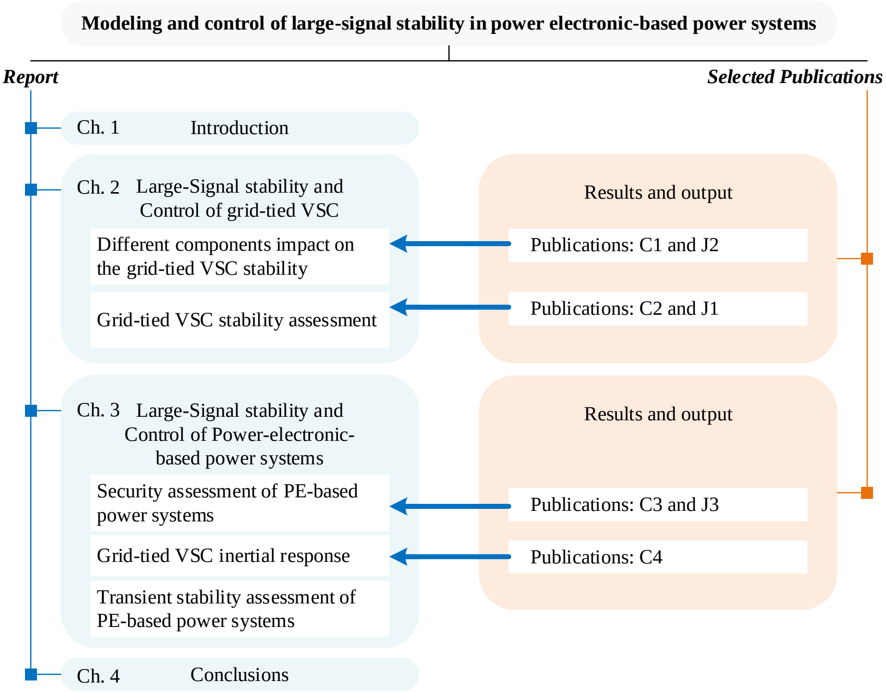

Fig. 1.14: Thesis structure and related published papers of each part.

In Chapter 1, the introduction of the Ph.D. project is presented, where the background of the research topic and the main objectives of the work are discussed. It starts with an introduction to the grid-tied VSC stability challenges. Then, it continues with the stability challenges of the PE-based power systems. Afterwards, the importance of the topic is discussed by introducing different stability challenges for some power systems, such as the South Australia power system and the Irish electric grid.

In Chapter 2, the large-signal stability of one grid-tied VSC is discussed. In this part, first, the grid-tied VSC model is presented. Then, each part of the grid-tied VSC, like the current controller, the PWM switching delay, the PLL, and the grid stiffness impact of the system stability are discussed in details.

In Chapter 3, the large-signal stability of PE-based power system is discussed. To study a large-scale power system with PE-based energy sources, PE-based unit is considered as simple as possible, and focus more on the stability of the whole system instead of a single unit. This enables a general guideline for assessing the stability and security of PE-based power systems and it is introduced. Also, a method to assess the large-signal stability of the PE-based power systems is presented.

In Chapter 4, a summary of the Ph.D. thesis is presented as well as futures trend of this work is discussed as well.

1.7. List of Publications

The research outcomes of the Ph.D. study have been disseminated in several forms of publications: Journal papers (Jx) and Conference papers (Cx), as listed below. Most of them are used in the Ph.D. thesis as previously listed.

Publications in Refereed Journals

Publications in Refereed Journals

- **J1.** **B. Shakerighadi**, E. Ebrahimzadeh, F. Blaabjerg, and C. L. Bak, ‘‘Large-signal stability modeling for the grid-connected VSC based on the Lyapunov method,’’ in Energies, vol. 11, p. 1-16, Oct. 2018.
- **J2.** **B. Shakerighadi**, E. Ebrahimzadeh, M. G. Taul, F. Blaabjerg and C. L. Bak, "Modeling and Adaptive Design of the SRF-PLL: Nonlinear Time-Varying Framework," in IEEE Access, vol. 8, pp. 28635-28645, 2020.
- **J3.** **B. Shakerighadi**, S. Peyghami, E. Ebrahimzadeh, M. G. Taul, F. Blaabjerg and C. L. Bak, " A New Guideline for Security Assessment of Power Systems with a High Penetration of Wind Turbines," in Appl. Sci., 10, 3190, p. 1-16, 2020.

Publications in Refereed Conferences

- **C1.** **B. Shakerighadi**, E. Ebrahimzadeh, F. Blaabjerg and C. L. Bak, "Lyapunov- and Eigenvalue-based Stability Assessment of the Grid-connected Voltage Source Converter," 2018 IEEE International Power Electronics and Application Conference and Exposition (PEAC), Shenzhen, 2018, pp. 1-6.
- **C2.** **B. Shakerighadi**, E. Ebrahimzadeh, C. L. Bak and F. Blaabjerg, " Large Signal Stability Assessment of the Voltage Source Converter Connected to a Weak Grid," Proceedings of Cigre Symposium Aalborg 2019, 2019, pp. 1-12.
- **C3.** **B. Shakerighadi**, S. Peyghami, E. Ebrahimzadeh, F. Blaabjerg and C. L. Bak, "Security Analysis of Power Electronic-based Power Systems," IECON 2019 - 45th Annual Conference of the IEEE Industrial Electronics Society, Lisbon, Portugal, 2019, pp. 4933-4937.
- **C4.** **B. Shakerighadi**, E. Ebrahimzadeh, F. Blaabjerg and C. L. Bak, "Large Signal Stability Assessment of the Grid-Connected Converters based on

its Inertia," 2019 21st European Conference on Power Electronics and Applications (EPE '19 ECCE Europe), Genova, Italy, 2019, pp. 1-7.

The below-mentioned journal publication also published in the Ph.D. period but not considered/summarized in this Ph.D. thesis:

- **B. Shakerighadi**, A. Anvari-Moghaddam, J. C. Vasquez, J. M. Guerrero, “Internet of Things for Modern Energy Systems: State-of-the-Art, Challenges, and Open Issues,” Energies, vol. 11, no. 5, p. 1252, May 2018.
- **B. Shakerighadi**, A. Anvari-Moghaddam, E. Ebrahimzadeh, F. Blaabjerg, and C. L. Bak, ‘‘A hierarchical game theoretical approach for energy management of electric vehicles and charging stations in smart grids,’’ IEEE Access, vol. 6, pp. 67223–67234, 2018.

Chapter 2.

Large-Signal stability and Control of grid-tied voltage source converters

2.1. Abstract

In this chapter, the large-signal stability of a single grid-feeding power converter is studied. The first part is dedicated to the modeling of the grid-connected VSC. Then, a method is proposed that is based on the Lyapunov function to assess the large-signal stability. The impact of different control loops on the system stability in addition to the large-signal stability assessment of the PLL are also discussed in this chapter.

2.2. Background and motivation

Grid-tied VSCs are becoming an inevitable part of PE-based power systems. To assess the large-signal stability of a PE-based power system, first, the behavior of a single grid-tied VSC should be well studied. Based on the control model of the grid-tied VSC and its topology, different large-signal models have been presented previously to study its large-signal stability behavior [24], [54], [65], [93]; In all these references, the grid is modeled as a voltage source and an impedance. Although this simplified model (Thevenin equivalent model) does not provide the exact dynamic response of the grid, it presents an acceptable behavior of the grid. In [24], the grid-tied VSC is modeled as a current source, in which the current controller and the PLL dynamics are considered in the modelling. In [65], the same approach is presented, where the grid impact on the system stability is analyzed. In [94], the grid-tied VSC stability is analyzed by using a phase portrait criterion concept; where the model used for the grid-tied VSC is the same as presented in [65].

A grid-tied VSC in a wind turbine system is shown in Fig. 2.1, where the grid is modeled as a voltage source and an impedance. The DC-link voltage control system is eliminated from the system for the sake of simplicity and it is assumed that it remains to have a constant value during a large disturbance; however, its impact on the large-signal stability of the grid-tied VSC is an interesting topic to investigate. The model presented in Fig. 2.1 is the benchmark model that is used in this chapter, and also later in the next chapter for the stability assessment of power system with high penetration of NSGs. Before starting the large-signal stability assessment of the grid-tied VSC, different nonlinear techniques to be used, such as phase portrait and the Lyapunov stability concepts, are discussed. After describing the nonlinear techniques, these methods are used to assess the large-signal stability of grid-tied VSCs.

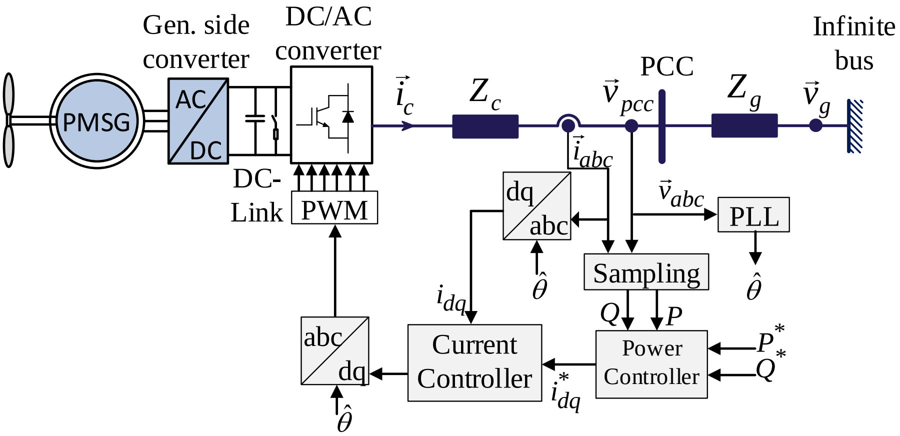

Fig. 2.1: A schematic of a grid-tied wind turbine, where focus is put on the voltage source converter (DC/AC converter) [57].

2.3. Large-signal Stability Assessment Techniques

PE-based power systems are inherently nonlinear systems that can be described by nonlinear differential equations. If the operating range of a control system is small, then it may be reasonable to approximate the differential equations by using linearization techniques. However, when the system is subjected to a large disturbance, then it makes sense to analyze the system by using nonlinear techniques. In this part, two basic nonlinear techniques, the Lyapunov function and the phase portrait concept, that are used to assess nonlinear systems are described [95].

2.3.1. Fundamentals of Lyapunov Theory

The most useful approach to assess the stability of nonlinear control systems is known as the Lyapunov stability criteria [95]. Here, a simplified description of the Lyapunov theory is presented, as a detailed explanation of it is out of scope of this project.

The dynamics of a nonlinear system can be presented by a set of nonlinear differential equations given as follows:

$$\dot{\mathbf{x}} = \mathbf{f}(\mathbf{x}, \mathbf{u}, t) \tag{2.1}$$

where $\mathbf{f}$ and $\mathbf{x}$ are a $n\times1$ nonlinear vector function and the $n\times1$ state vector, respectively. $\mathbf{u}$ presents the control input. An equilibrium state of the system, $\mathbf{x}^*$, is defined as a state that if once $\mathbf{x}(t) = \mathbf{x}^*$, then it remains to it for all future time, which means $\mathbf{f}(\mathbf{x}^*) = 0$. Now, let us define the basic concepts of stability and instability:

Definition [95]**:** The equilibrium $\mathbf{x} = 0$ is stable if, for any $R > 0$, there exists $r > 0$, such that if $\|\mathbf{x}(0)\| < r$, then $\|\mathbf{x}(t)\| < R$ for all $t \geq 0$. Otherwise, the equilibrium point is unstable.

The abovementioned definition of the stability indicates that if an equilibrium point, $\mathbf{x}(0)$, is stable, then if the system state equals $\mathbf{x}(0)$ for all $t \geq 0$ the system state remains with a certain area (limited area). This leads to the definition of the Lyapunov function. Considering a stable physical system, *S*, the energy of *S*, including its potential and kinetic energies, is limited to a certain value, if the system is stable. Therefore, for a stable state of *S*, called $\mathbf{x}(0)$, the energy of the system will remain limited. Let us define the energy of *S* as *V*. If *V* is a positive value and its derivative with respect to the time is negative, then $\lim_{t\to\infty} V = 0$, which means that the state of the system will remain inside a certain zone. In other words, if $V(\mathbf{x}) > 0$, $\dot{V}(\mathbf{x}) < 0$, and $V(\mathbf{x}) \to \infty$ as $\|\mathbf{x}\| \to \infty$, then the equilibrium point at the origin is stable. For instance, considering the nonlinear mass-damper-spring system that its dynamic equation is:

$$m\ddot{x} + b\dot{x}\left|\dot{x}\right| + k_0 x + k_1 x^3 = 0 \tag{2.2}$$

where $\dot{x}|\dot{x}|$ represents nonlinear damping, and $(k_0 x + k_1 x^3)$ is a nonlinear spring term. Considering *V* as the total mechanical energy of the system, which is the sum of its kinetic and potential energies defined as follows:

$$V\left(x,t\right) = \frac{1}{2}m\dot{x}^2 + \int_0^x \left(k_0 x + k_1 x^3\right) dx = \frac{1}{2}m\dot{x}^2 + \frac{1}{2}k_0 x^2 + \frac{1}{4}k_1 x^4 \tag{2.3}$$

and $\dot{V}$ as follows:

$$\dot{V}\left(x,t\right) = m\dot{x}\ddot{x} + \left(k_0 x + k_1 x^3\right)\dot{x} = \dot{x}\left(-b\dot{x}\left|\dot{x}\right|\right) = -b\left|\dot{x}\right|^3, \tag{2.4}$$

the Lyapunov function is always positive, and its derivative is always negative until $\dot{x} = 0$. Therefore, the system presented in (2.2) is a stable system.

Now consider the system described by:

$$\begin{aligned} \dot{x}_1 &= 2x_2 + x_1\left(x_1^2 + x_2^4\right) \\ \dot{x}_2 &= -2x_1 + x_2\left(x_1^2 + x_2^4\right). \end{aligned} \tag{2.5}$$

By defining the Lyapunov function as follows:

$$V(x,t)=\frac{1}{2}\left(x_1^2+x_2^2\right) \tag{2.6}$$

which is a positive definite function, its derivative is:

$$\dot{V}(x,t)=\left(x_1^2+x_2^2\right)\left(x_1^2+x_2^4\right). \tag{2.7}$$

The Lyapunov function and its derivative are always positive, which means that the system is not stable.

The concept of the Lyapunov theory is valid for nonlinear and linear systems. For a linear system, $\dot{\mathbf{x}}=\mathbf{Ax}+\mathbf{Bu}$, if all eigenvalues of A are in the left-half of the complex plane, then the equilibrium is stable. This last sentence is another expression of the Lyapunov function.

2.3.2. Phase Portrait concept

The phase plane method is usually used for the stability analysis of second-order systems described by

$$\begin{aligned}\dot{x}_1 &= f_1(x_1,x_2)\\ \dot{x}_2 &= f_2(x_1,x_2)\end{aligned} \tag{2.8}$$

where x_1 and x_2 are the state variables of the system, f_1 and f_2 are nonlinear functions. This nonlinear stability analysis technique is of interest in this project, as some control loops can be modeled as a second-order nonlinear control system. As it is discussed later in Sections 2.4.3 and 2.5.3, the SRF-PLL is a nonlinear feedback control loop that can be modeled as a second-order system. In this way, the phase portrait concept is used to analyze the large-signal stability of such a system; see Section 2.5.3 [J2].

The state space that includes x_1 and x_2 indicates the phase plane. For a stable equilibrium point, $\dot{\mathbf{x}}=0$, $f_1(x_1,x_2)=f_1(x_1,x_2)=0$. For a second-order system that is represented as $\ddot{x}+f(x,\dot{x})=0$, the dynamics can be presented as $\dot{x}_1=x_2$ and $\dot{x}_2=-f_1(x_1,x_2)$ with $x_1=x$ and $x_2=\dot{x}$. In this way, by constructing the phase plane trajectories it can be seen whether the system becomes stable or not. Different analytical methods, such as Lienard's method and Pell's method can be used to construct the phase plane trajectories [95].

2.4. Grid-tied VSC's Component Modelling

A grid-tied VSC includes different parts based on its control mode. Here, the grid-feeding mode of the VSC is considered to study. However, the analysis presented in this section can be extended to other modes of the VSC like discussed in Chapter 1.

The control system of a grid-feeding power converter includes a current control loop, active and reactive power control loops and a SRF-PLL. Here, the current control loop, the delay caused by the PWM switching, and the SRF-PLL model are described and modeled.

2.4.1. Current control loop

The current control is the fastest controller used in a grid-feeding power converter control system. Following the VSC current, $\vec{i}_c$, can be determined as follows:

$$\vec{v}_g = \vec{v}_c + R_T \vec{i}_c + L_T \frac{d}{dt} \vec{i}_c \tag{2.9}$$

where $\vec{v}_c$ and $\vec{v}_g$ are the converter output voltage and the grid voltage, respectively. $Z_c = R_c + jL_c$ and $Z_g = R_g + jL_g$ are the converter output filter and the grid impedance, respectively. $L_T = L_c + L_g$ and $R_T = R_c + R_g$. Rewriting (2.9) in the *dq*-frame that rotates with an angular speed ω is given as follows [66], [96]:

$$\begin{aligned} v_{g.d} &= R_T i_d + L_T \frac{d}{dt} i_d + v_{c.d} - \omega L_T i_q \\ v_{g.q} &= R_T i_q + L_T \frac{d}{dt} i_q + v_{c.q} + \omega L_T i_d \end{aligned} \tag{2.10}$$

where $\vec{v}_c = (v_{c.d} + jv_{c.q})e^{j\omega t}$, $\vec{v}_g = (v_{g.d} + jv_{g.q})e^{j\omega t}$, and $\vec{i}_g = (i_d + ji_q)e^{j\omega t}$. As it can be seen from (2.10), d and q terms of the voltage are coupled by terms of $-\omega L_T i_q$ and $+\omega L_T i_d$, which can be eliminated in the controller as shown in Fig. 2.2. In this controller, the grid is assumed to be a stiff voltage source and the VSC output filter, Z_c, includes only an inductance.

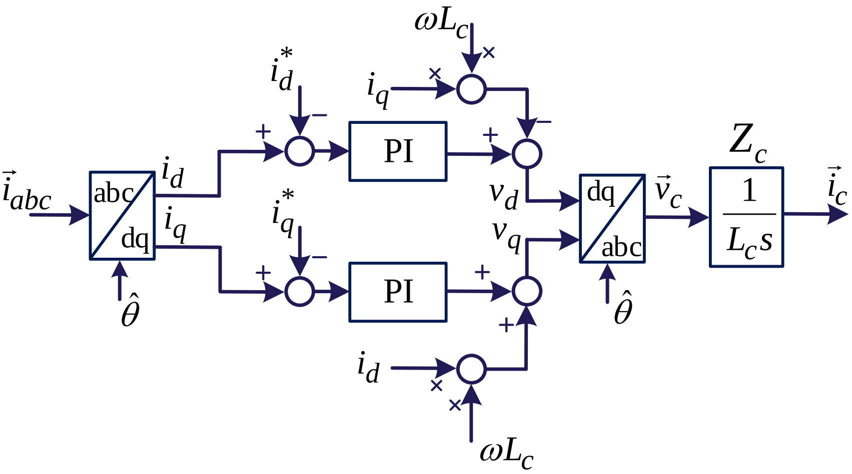

Fig. 2.2: Grid-tied VSC current control in *dq*-axis including decoupling terms [57].

2.4.2. Delay caused by the PWM switching

Although different approaches can be used for the modeling of the PWM switching delay, a simple method can be presented by the *Padé* approximation as follows [97]:

$$G_{pwm} = e^{-T_d s} \approx \frac{1-0.5T_d s}{1+0.5T_d s} \tag{2.11}$$

where T_d indicates the time delay of digital control and PWM.

2.4.3. SRF-PLL

In order to synchronize the grid-tied VSC with the grid, a synchronization unit should be used. A standard synchronization unit that is widely used is the SRF-PLL. The SRF-PLL is a nonlinear feedback control that is used to estimate the voltage phase angle and frequency of the PCC, or $\hat{\theta}$, as we can see in block diagram shown in Fig. 2.3 [9]. A standard form of the SRF-PLL is shown in Fig. 2.3, where Fig. 2.3(a) shows the schematic block-diagram of the SRF-PLL, where the input is the $\vec{v}(t) = \frac{2}{3}\left[e^{j0}v_a(t) + e^{j\frac{2\pi}{3}}v_b(t) + e^{j\frac{4\pi}{3}}v_c(t)\right]$, in which $v_a(t) = V_{pcc}\cos(\omega t + \varphi)\, v_b(t) = V_{pcc}\cos\left(\omega t + \varphi - \frac{2\pi}{3}\right)$, and $v_c(t) = V_{pcc}\cos\left(\omega t + \varphi - \frac{4\pi}{3}\right)$. Fig. 2.3(b) presents a nonlinear form of the SRF-PLL, while, Fig. 2.3(c) indicates its linear form. The linearization form is achieved by considering that $\sin(\theta - \hat{\theta}) \approx \theta - \hat{\theta}$ for small values of $\theta - \hat{\theta}$.

The PLL is used to estimate the PCC grid voltage magnitude, frequency (ω), and the phase angle (θ) as follows:

$$\hat{\upsilon}(t) = \hat{V}_{pcc}\cos\Big(\overbrace{\hat{\omega}t+\hat{\varphi}}^{\hat{\theta}}\Big) \tag{2.12}$$

where $\hat{v}(t)$ is the estimated value of the input signal (here it is the voltage of the PCC). $\hat{V}_{pcc}$, $\hat{\omega}$, $\hat{\varphi}$, and $\hat{\theta}$ are the estimated values for the voltage magnitude, frequency, the initial phase, and the phase angle, respectively.

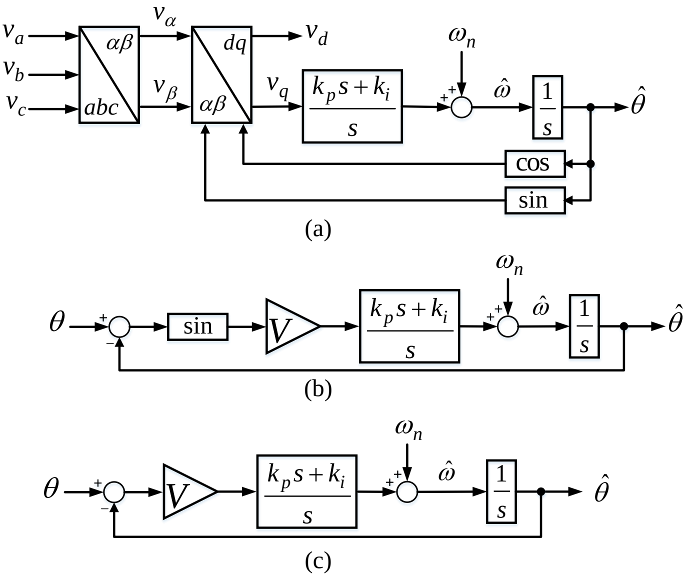

Fig. 2.3: A schematic block-diagram of an SRF-PLL. (a) The complete model, (b) its nonlinear equivalent, (c) and its linear model [9].

2.5. Grid-tied VSC signal stability analysis

In this part, the grid-tied VSC large-signal stability is assessed by using the techniques discussed in Section 2.3 and the models presented in Section 2.4.

A schematic block-diagram of a grid-feeding power converter is shown in Fig. 2.4. This is the same model as presented in Fig. 2.1; however, the DC-link model is eliminated. This is because it is assumed that the DC-link voltage is constant and the grid side fluctuations do not have any effect on it. In a real-world condition, a DC-link voltage control should be added to the control system. Therefore, it is expected that the analysis presented here is slightly different from the behavior of grid-tied VSCs in real-world condition.

It is also worth mentioning that the output signal of the PLL is $\hat{\theta}$; however, if it is needed to eliminate the impact of the PLL (for the sake of simplicity), it can be assumed that the PLL works ideally, which means that it can estimate the PCC voltage phase angle (θ) instantly, as shown in Fig. 1.9.

The grid-feeding power converters have different control loops such as the current controller, power controller, and PLL to be synchronized to the grid, as discussed in Section 2.4. To present a large-signal stability model of a grid-feeding power converter, let start with the simplest form of the system, where only the current controller is considered. Here, it is assumed that the PLL works ideally and there is no delay caused by the PWM switching in the control loop. By considering the simplest form of a grid-feeding power converter, its schematic in the *s*-domain is shown in Fig. 2.5. However, it should be noticed that the PLL is considered as an instant phase estimator, which means that $\theta = \hat{\theta}$. In addition, the active and reactive power control is not considered in the model shown in Fig. 2.5. It is worth mentioning that although the model presented in Fig. 2.5 is the small-signal model of the grid-tied VSC, it can assessed by large-signal stability assessment techniques, which is shown later in this chapter.

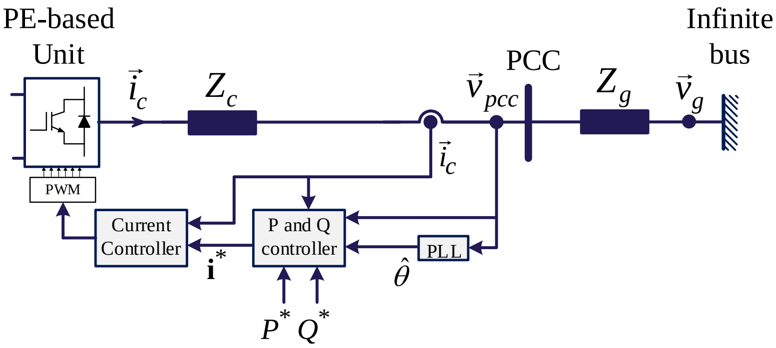

Fig. 2.4: A schematic block-diagram of a grid-feeding power converter as shown in Fig. 1.9 [57].

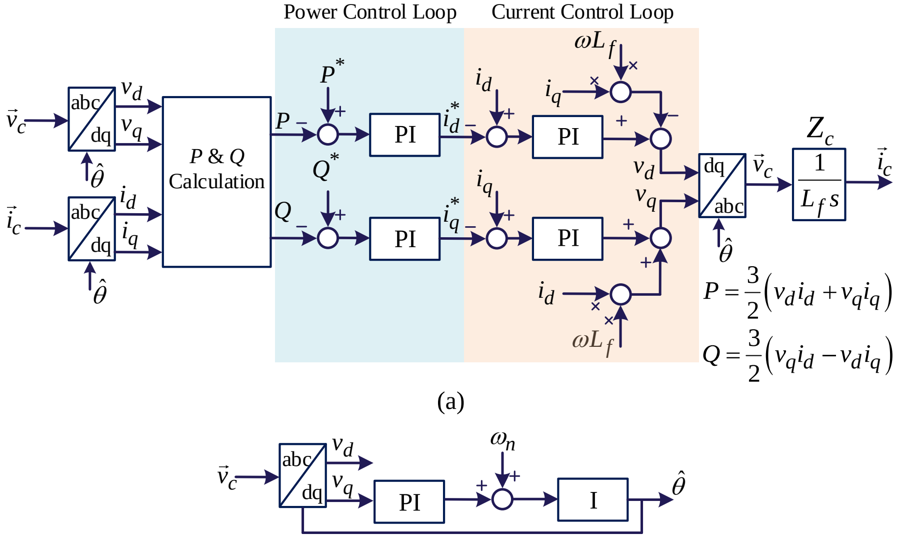

(a)

(b)

Fig. 2.5: Small-signal model of (a) the grid-feeding power converter including the current control and active power controllers and (b) the SRF-PLL as shown in [57].

2.5.1. Lyapunov- and Eigenvalue-based Stability Assessment of the Grid-connected Voltage Source Converter

The small-signal model of the grid-feeding power converter, as shown in Fig. 2.5, can be represented as follows:

$$\begin{pmatrix} \dot{x}_1 \\ \dot{x}_2 \end{pmatrix} = \begin{pmatrix} 0 & -K_i \\ \frac{1}{L_f} & -\frac{K_p}{L_f} \end{pmatrix} \begin{pmatrix} x_1 \\ x_2 \end{pmatrix} + \begin{pmatrix} K_i \\ \frac{K_p}{L_f} \end{pmatrix} . I_{ref} \tag{2.13}$$

where (x_1, x_2) are the system state variables. K_p and $K_i$are the proportional and integral gains of the current controller, respectively. L_f (L_c as it is presented in Section 2.4.1) is the filter inductance. For simplicity, the grid is considered as ideal, which means that its impedance is equal to zero ($L_g = 0$). For more simplicity, it can be assumed that the reactive power is set to zero, and just the controller for *d*-axis is discussed here. In order to assess the small-signal stability of the system, the real part of eigenvalues of the state space model should be in the left half plane of the s-plane (with real and imaginary axis). The eigenvalues of the system can be derived as follows:

$$\lambda_{1,2} = \frac{-\left(\frac{K_p}{L_f}\right) \pm \sqrt{\left(\frac{K_p}{L_f}\right)^2 - 4\frac{K_i}{L_f}}}{2} \tag{2.14}$$

where $\lambda_{1,2}$ are the system eigenvalues. As it can be seen from the system eigenvalues, as long as K_p and $K_i$are positive, both eigenvalues have a negative real part, which means that the system is working in its stable mode. It is worth mentioning that the small-signal model of the system represented here can also be used to tune the converter controllers [98]. To tune the parameters, the proportional and integral gains are typically selected so the closed-loop poles have the optimum damping factor of 0.7, and the desired bandwidth, given as ω [99], [100]. Considering a system with an equivalent transfer function as:

$$G(s) = \frac{as+b}{s^2 + 2\zeta\omega_n s + \omega_n^2} \tag{2.15}$$

where ζ is the damping factor of the system and ω_n is the natural frequency.

Now, in order to assess the system stability by using a large-signal analysis technique, first, a Lyapunov function should be defined for the system. A second-order Lyapunov function, $V(\mathbf{x},t)$, can be defined for a system based on its state-space variables, as follows:

$$V(\mathbf{x},t) = \mathbf{x}^{\mathbf{T}}.\mathbf{P}.\mathbf{x} \tag{2.16}$$

where $\mathbf{x} = \binom{x_1}{x_2}$ is the state-variable vector and $\mathbf{x}^{\mathbf{T}}$ is its transpose. **P** is a positive definite matrix. $V(\mathbf{x},\mathrm{t})$ is the Lyapunov function of the system. In this way, V has always a positive value. However, its derivative with respect to the time can be negative, as follows:

$$\dot{V}(\mathbf{x},t) = \left(\mathbf{x}^{\mathbf{T}}.\mathbf{P}.\mathbf{x}\right)' = -\mathbf{x}^{\mathbf{T}}.\mathbf{Q}.\mathbf{x} \tag{2.17}$$

where $\mathbf{Q} = -(\mathbf{A}^{\mathbf{T}}\mathbf{P} + \mathbf{P}\mathbf{A})$. In case that **Q** is a positive definite matrix, then the derivative of the Lyapunov function is negative, which further means that the systems is stable [101].

In general, by defining a Lyapunov function for a system ($V(\mathbf{x},t)$), its derivative with respect to the time can be calculated ($\dot{V}(\mathbf{x},t)$). If the Lyapunov function of the system and its derivative with respect to the time are positive definite and negative definite, respectively, then it can be concluded that the system is globally stable as also discussed in Section 2.3.1 [101], [102].

For the abovementioned model of the grid-feeding power converter, the **P** matrix can be defined in its parametric form, as follows:

$$\mathbf{P} = \begin{pmatrix} s_{11} & s_{12} \\ s_{21} & s_{22} \end{pmatrix} \tag{2.18}$$

where s_{11}, s_{12}, s_{21}, and s_{22} are real numbers that satisfy the following inequality for any non-zero real numbers of a and b:

$$a^2 s_{11} + ab\left(s_{12} + s_{21}\right) + b^2 s_{22} \rangle\ 0. \tag{2.19}$$

In this way, **P** is a positive definite matrix, which leads to a positive value for $V(\mathbf{x},t)$. Based on that, **Q** can be calculated as follows:

$$\mathbf{Q} = \begin{pmatrix} \dfrac{\left(s_{12} + s_{21}\right)}{L_f} & s_{11}K_i + \dfrac{K_p}{L_f^2} s_{22}s_{12} \\ s_{11}K_i + \dfrac{K_p}{L_f^2} s_{22}s_{21} & \left(s_{12} + s_{21}\right)K_i + 2\dfrac{K_p}{L_f} s_{22} \end{pmatrix} \tag{2.20}$$

where **Q** is positive definite when K_p and K_i are positive. In that case, the system is stable. Considering a fixed integral gain and different proportional gains for the current controller the step responses are as shown in Fig. 2.6. For this simulation, the main grid is considered as an ideal one, which means that $Z_g = 0$. In addition, $L_f = 10\ mH$. The reactive power is set to zero, while the active power is set to 4 kW.

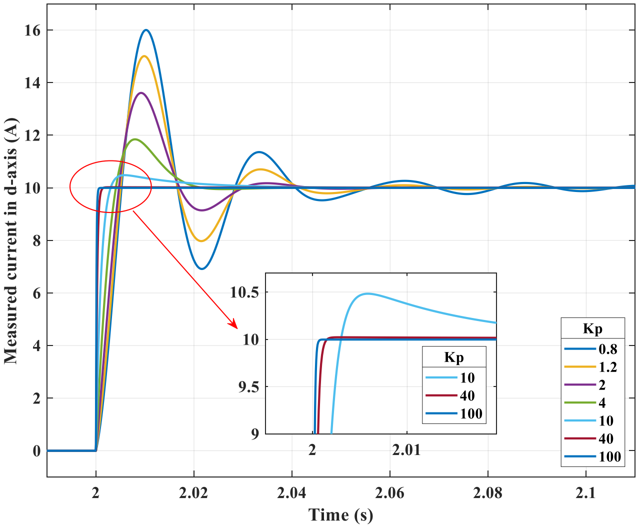

Fig. 2.6: Step response of the current control in time domain simulation (Matlab). K_i = 800, and K_P increasing from 0.8 to 100 [C1].

However, it can be seen that by increasing K_p, the real part of eigenvalues become larger except one of them as shown in Fig. 2.7, where the all eigenvalues that their real become larger are indicated by the green arrow and the eigenvalue that its real part become smaller is indicated by the red arrow. This makes the system to behave like a first order transfer function. The system eigenvalues for different K_p is shown in Fig. 2.7.

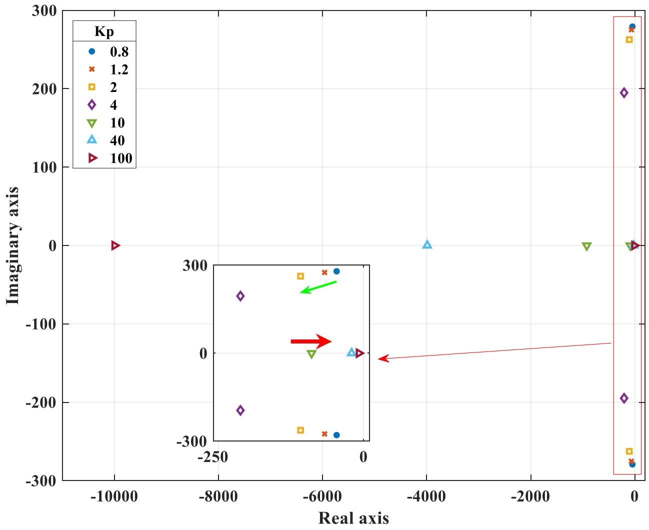

Fig. 2.7: Eigenvalues of the current control $K_i = 800$, and K_p increasing from 0.8 to 100 [C1].

Considering the system Lyapunov function and its derivative with respect to the time as discussed in (2.16) and (2.17), for all positive values of $K_p + R$ and K_i, the system remains stable. This is schematically shown in Fig. 2.8.

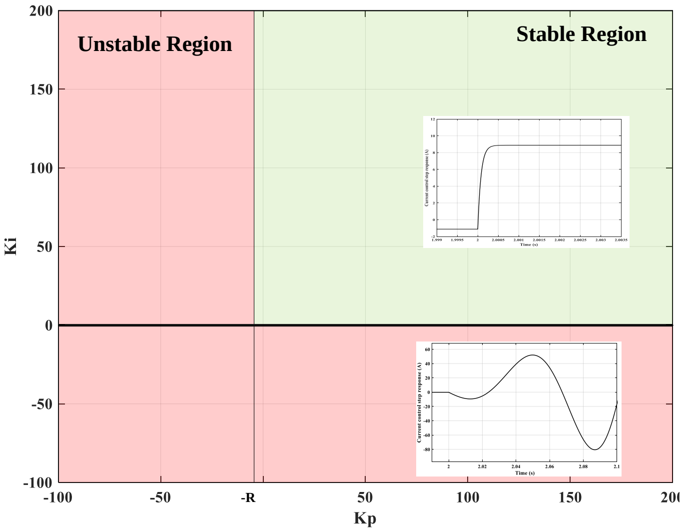

Fig. 2.8: Stability region for the current control of the grid connected VSC.

Up to here, only the current controller is considered in the grid-tied VSC control loop. Next, let us try to assess the grid stiffness impact on the large-signal system stability of the grid-tied VSC considering the active power control loop, which is also presented in [C2]. In addition, it is worth mentioning that the Lyapunov function that is defined in (2.16) is just a way of defining it. There are different ways of defining a Lyapunov function, and as long as it satisfies the stability conditions, it can be used for the stability assessment. In this way, the following Lyapunov function that is defined as follows, is used for the stability assessment.

$$V\left(\delta,\omega\right)=\frac{1}{2}M\omega^2-P_{ref}\left(\delta-\delta_2\right)-P_{\max}\left(\cos\left(\delta\right)-\cos\left(\delta_2\right)\right) \tag{2.21}$$

where M presents the moment of inertia for the VSC. It is worth mentioning that M is dependent on the configuration of the control system. P_{max} and P_{ref} are the maximum and the reference active power of the VSC, respectively. δ and δ_2 are the PCC actual voltage angle and its post-fault value, respectively. Previously, the PCC voltage angle is mentioned as θ. P_{max} is defined as follows:

$$P_{\max}=\frac{\left|\vec{v}_c\right|\left|\vec{v}_g\right|}{\left|Z_c+Z_g\right|}. \tag{2.22}$$

The output active power of the VSC, P_e, can be determined as follows:

$$P_e=\left|\vec{v}_c\right|\left|\vec{i}_c\right|\cos\delta. \tag{2.23}$$

By monitoring the Lyapunov function defined in (2.21), the stability of the grid-tied VSC can be diagnosed. To test the credibility of the Lyapunov function in (2.21) three scenarios are defined as follows: Scenario 1: Stiff grid ($SCR = 5.09\, p.u.$), Scenario 2: Weak grid ($SCR = 2.54\, p.u.$), and Scenario 3: Very weak grid ($SCR = 1.36\, p.u.$). The control system is as presented in Fig. 2.5, where the impact of the PLL is not considered in the control system and analysis.

Scenario 1: Changing the reference for the active power

In case that the active power reference is changed from 4 kW to 10 kW, where the grid is stiff, it will remain stable. However, here, the grid is not considered ideally stiff, where the grid impedance is 10 mH. The active power and the Lyapunov function of the system are shown in Fig. 2.9 and Fig. 2.10, respectively.

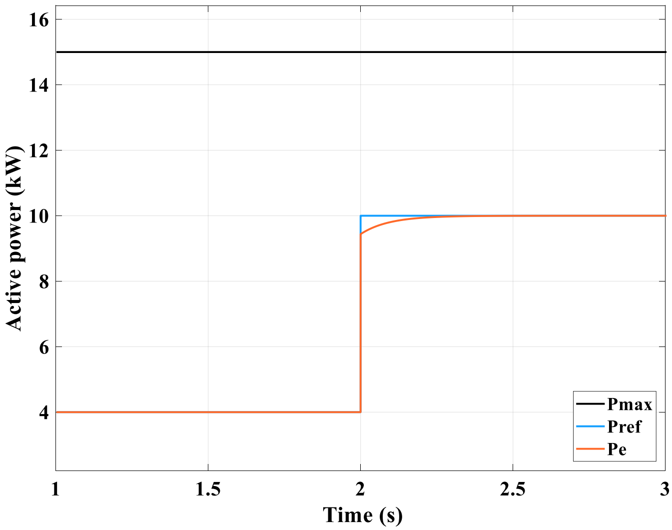

Fig. 2.9: Maximum transferable (P_{max}), reference (P_{ref}), and output active power (P_e) of the grid-connected VSC with a step change in the active power reference at t = 2 s [C2].

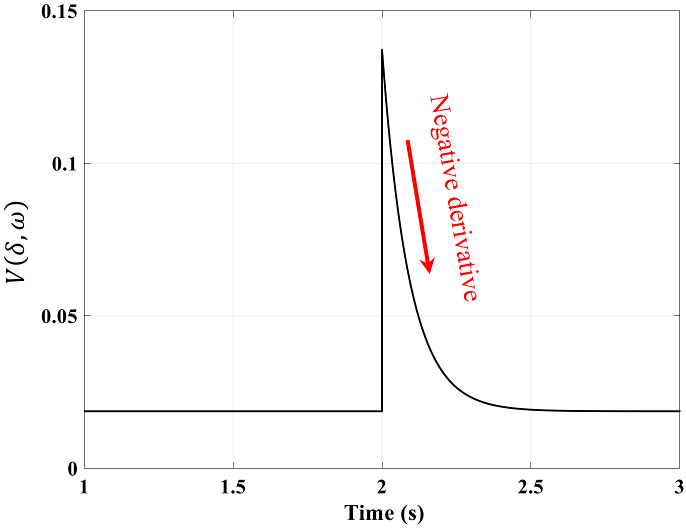

Fig. 2.10: The energy function value of the grid-connected VSC when the active power reference is changed at t = 2 s [C2].

Regarding the large-signal stability assessment based on the Lyapunov functions, it can be seen from Fig. 2.10 that the energy function has a positive value and its derivative with respect to the time is negative. This means that the system is stable.

Scenario 2: Weak grid scenario

In this scenario, the system configuration is changed to demonstrate the weak grid impact on the system stability. To do so, the grid impedance is considered having two parallel lines with 20 mH inductance. Then, it is assumed that one of the lines are disconnected. This means that the SCR becomes half of the initial value (from 5.09 pu to almost 2.54 pu). Here, the grid with 2.54 is considered as a weak grid. It should be noticed that this definition for the weak grid could vary for different power systems.

The active power and the energy function are shown in Fig. 2.11 and Fig. 2.12, respectively.

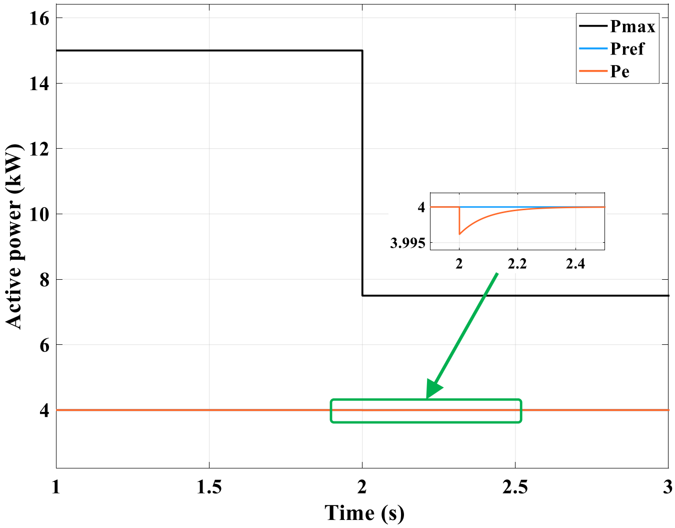

Fig. 2.11: Maximum transferable (P_{max}), reference (P_{ref}), and output active power (P_e) of the grid-connected VSC when the grid impedance is changed in L_g from 10 mH to 20 mH [C2].

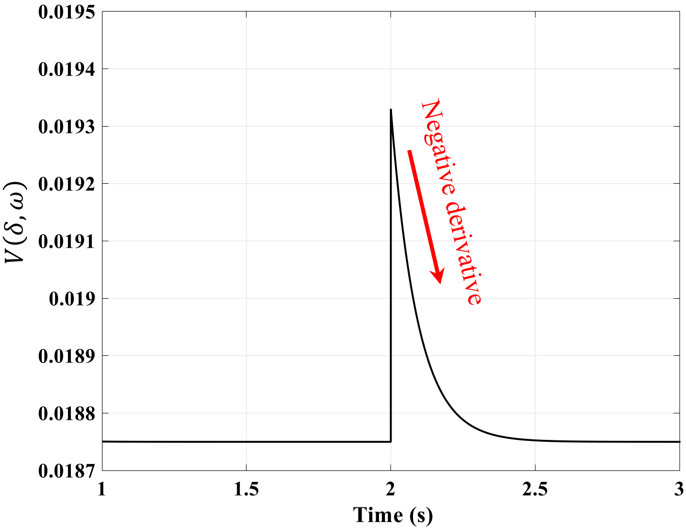

Fig. 2.12: The energy function value of the grid-connected VSC when L_g is changed from 10 mH to 20 mH [C2].

Although the grid is weak, the system remains stable for this case study. This can also be seen from Fig. 2.12, where the energy function and its derivative with respect to the time is positive and negative, respectively. The time-domain simulation results for the VSC output current and the PCC voltage magnitude are shown in Fig. 2.13.

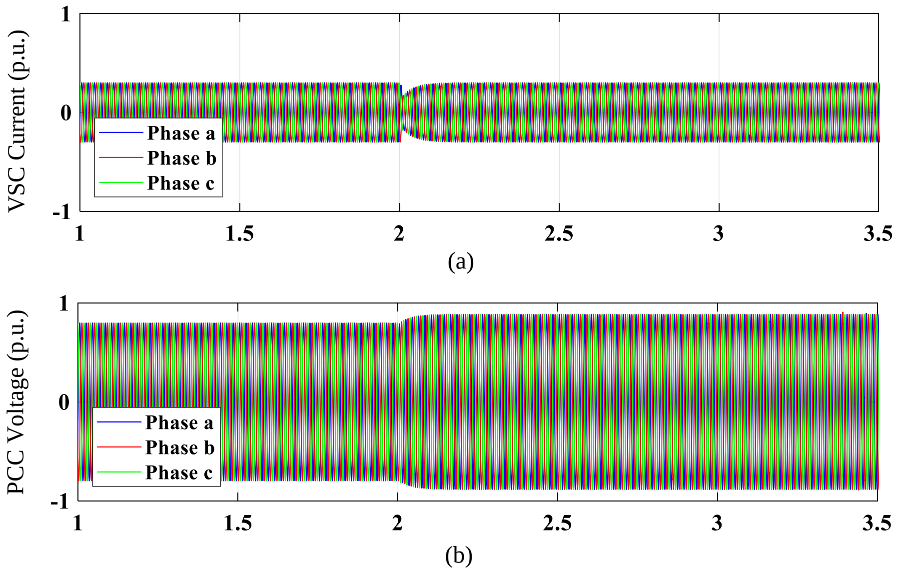

Fig. 2.13: (a) Three-phase output current of the grid-tied VSC and (b) PCC three-phase voltage for Scenario 3, when the SCR of the grid changes from 5.09 pu to 2.54 pu.

Scenario 3: Very weak grid scenario

Here, the main grid SCR changes from 5.09 pu to 1.36 pu. The system cannot be run in this case, due to the fact that the output active power is larger than the maximum transferable active power, as shown in Fig. 2.14, where a mathematical model of the system is presented. Therefore, it does not show the instability, however, it can be seen that the output active power is larger than the maximum active power, which is not feasible in time-domain simulation.

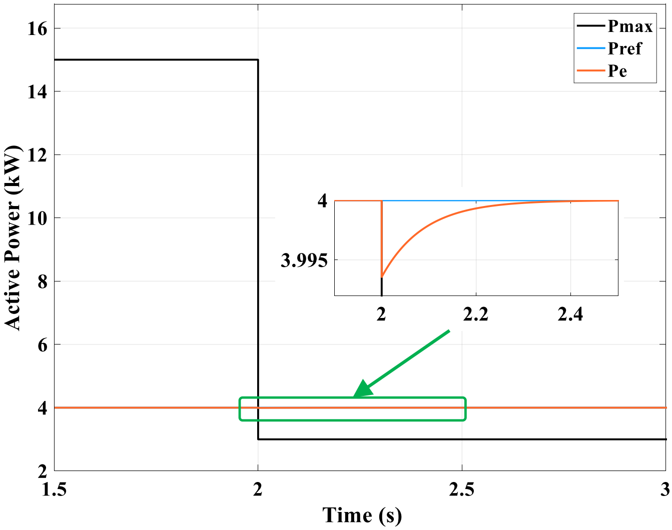

Fig. 2.14: Maximum transferable (P_{max}), reference (P_{ref}), and output active power (P_e)of the grid-connected VSC with a step change in Lg from 10 mH to 50 mH [C2].

A time-domain simulation for this scenario is presented in Fig. 2.15, where the PCC voltage and the VSC output current for this scenario are shown. The grid impedance changes from 10 mH to 50 mH at $t = 2\ s$, which makes the system unstable.

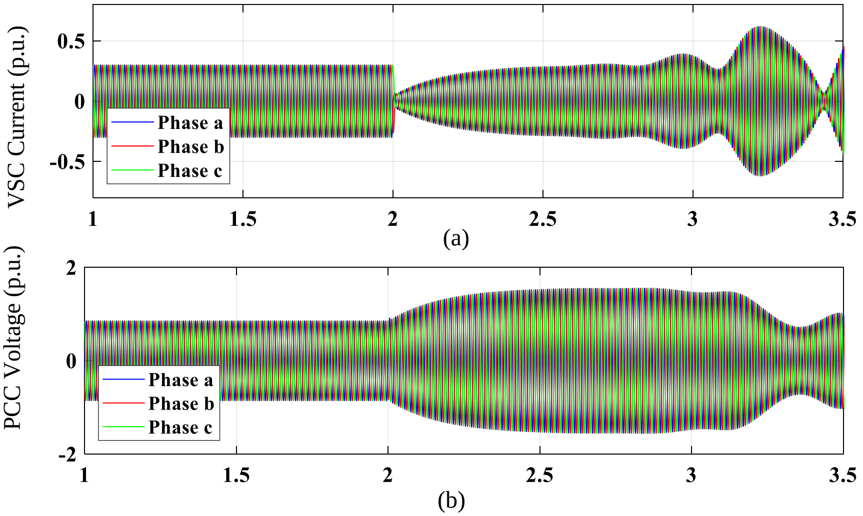

Fig. 2.15: (a) Three-phase output current of the grid-tied VSC and (b) PCC three-phase voltage for Scenario 3, when the SCR of the grid changes from 5.09 pu to 1.36 pu.

Based on the Lyapunov function definition, its value stands constant. However, its derivative with respect to the time becomes zero at this point. This means that the system cannot recover to its base energy value in the case that the Lyapunov function increases.

2.5.2. Large-Signal Stability Modeling for the Grid-Connected VSC Based on the Lyapunov Method

Next, to make the assessment more realistic, the PWM switching delay is added to the system model. As it has been mentioned previously, the delay can be modeled by using the *Padé* approximation given as follows:

$$e^{-T_d s} = \frac{1-0.5T_d s}{1+0.5T_d s} \tag{2.24}$$

where T_d is the time delay. The grid-tied VSC model that is used here is presented in Fig. 2.16. The PLL impact is still neglected, hence $\theta = \hat{\theta}$. For simplicity, the reactive power is considered to be zero ($\vec{i}_q^* = 0$); however, the study can be generalized for the reactive power as well.

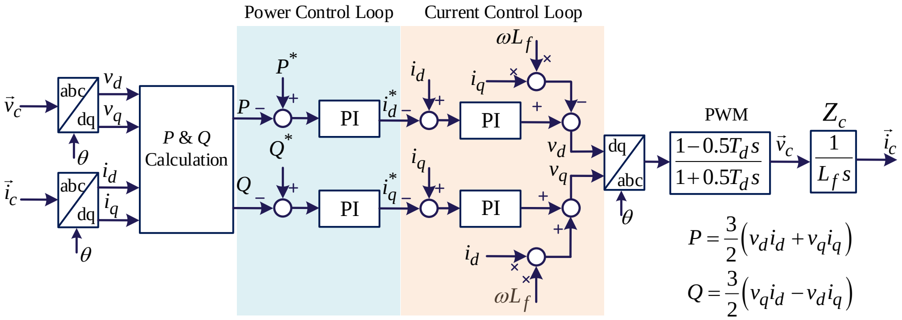

Fig. 2.16: Small-signal model of the grid-feeding power converter including the current control, active power controllers, and the PWM switching delay model.

This makes the state-space model of the system as follows:

$$\begin{aligned}\dot{\mathbf{x}} &= \mathbf{A}\mathbf{x}+\mathbf{B}i_d^* \\ i_d &= \mathbf{C}\mathbf{x}\end{aligned} \tag{2.25}$$

where **x** is the state variable vector, and **A**, **B**, and **C** are as follows:

$$A=\begin{pmatrix} 0 & 0 & -K_i \\ \dfrac{1}{0.5T_d} & -\dfrac{1}{0.5T_d} & -\dfrac{K_P}{0.5T_d} \\ -\dfrac{1}{L} & \dfrac{2}{L} & \dfrac{K_P-R}{L} \end{pmatrix} \quad \mathbf{B}=\begin{pmatrix} K_i \\ \dfrac{K_P}{0.5T_d} \\ -\dfrac{K_P}{L} \end{pmatrix} \\ \mathbf{C}=\begin{pmatrix}0 & 0 & 1\end{pmatrix} \tag{2.26}$$

The Lyapunov function and its derivative with respect to the time can be defined as follows:

$$\begin{cases} V(x,t)=\mathbf{x}^{\mathbf{T}}\mathbf{P}\mathbf{x} \\ \dot{V}(x,t)=\dfrac{dV(x,t)}{dt}=\dfrac{d\left(\mathbf{x}^{\mathbf{T}}\mathbf{P}\mathbf{x}\right)}{dt}=\left(\dfrac{d\left(\mathbf{x}^{\mathbf{T}}\right)}{dt}\right)\mathbf{P}\mathbf{x}+\mathbf{x}^{\mathbf{T}}\mathbf{P}\left(\dfrac{d\left(\mathbf{x}\right)}{dt}\right) \\ =\mathbf{x}^{\mathbf{T}}\left(\mathbf{A}^{\mathbf{T}}\mathbf{P}+\mathbf{P}\mathbf{A}\right)\mathbf{x}=-\mathbf{x}^{\mathbf{T}}\mathbf{Q}\mathbf{x} \end{cases} \tag{2.27}$$

where **x** is the state variables vector. In order to check the large-signal stability of the system by using the Lyapunov function, a parametric negative definite value is defined for the Lyapunov derivative with respect to the time, and it should be checked whether the Lyapunov function value is positive definite or not. To do so, **Q** is defined as follows:

$$\mathbf{Q} = \begin{pmatrix} 2\times a & a & a \\ a & 2\times a & a \\ a & a & 2\times a \end{pmatrix} \tag{2.28}$$

where a is a positive real number. **P** is given as follows:

$$\mathbf{P} = \begin{pmatrix} P_{11} & P_{12} & P_{13} \\ P_{21} & P_{22} & P_{23} \\ P_{31} & P_{32} & P_{33} \end{pmatrix}. \tag{2.29}$$

Considering $\mathbf{Q} = -(\mathbf{A^T P} + \mathbf{PA})$ as mentioned in (2.27) and writing the state-space model based on **P** and **Q**, the following equations are obtained based on (2.26), (2.27), (2.28), and (2.29) :

$$\begin{cases} \frac{2}{L}P_{13} - \frac{2}{0.5T_d}P_{12} = 2a \\ \frac{1}{0.5T_d}P_{12} - \frac{2}{L}P_{13} - \frac{1}{0.5T_d}P_{22} + \frac{1}{L}P_{23} = a \\ K_i P_{11} + \frac{K_P}{0.5T_d}P_{12} - \frac{K_P}{L}P_{13} - \frac{1}{0.5T_d}P_{23} + \frac{1}{L}P_{33} = a \\ \frac{2}{0.5T_d}P_{22} - \frac{4}{L}P_{23} = 2a \\ K_i P_{12} + \frac{K_P}{0.5T_d}P_{22} + \left(\frac{1}{0.5T_d} - \frac{K_P}{L}\right)P_{23} - \frac{2}{L}P_{33} = a \\ 2K_i P_{13} + \frac{2K_P}{0.5T_d}P_{23} - \frac{2K_P}{L}P_{33} = 2a \end{cases}. \tag{2.30}$$

By solving the above equations, **P** can be determined. Then, the Lyapunov function and its derivative with respect to the time can be determined.

To validate the abovementioned study, the following simulation results are presented. For the grid-tied VSC, considering a fixed value for the integral gain of the current controller and increasing the proportional gain of the current controller, the system might become unstable. This is because of the delay in PWM switching. This also means that for a large value of the proportional gain, the **P**'s eigenvalues become negative. The eigenvalues for a negative value of proportional gain is expected to be negative. Although the negative gain for the controllers is not a realistic assumption, it is presented here to show the validity of the mathematical model.

The eigenvalues of **P** for different values of the proportional gain are shown in Fig. 2.17 and Fig. 2.18. Although eigenvalues for the negative gains of K_P are shown in Fig. 2.18, it is not further discussed, due to a negative gain for a controller is rarely used.

Other parameters of the system are presented as follows: $L_f = 10\ mH$, $|\vec{v}_g| = 400\ V$ (rms phase to phase voltage), $f = 50\ Hz$, $T_d = 1.5e - 4\ s$.

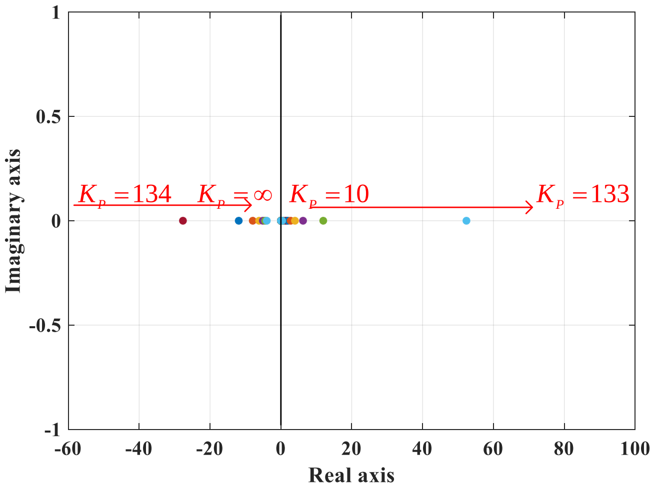

Fig. 2.17: Eigenvalues of the P matrix for positive values of K_P and K_i = 600 [J1].

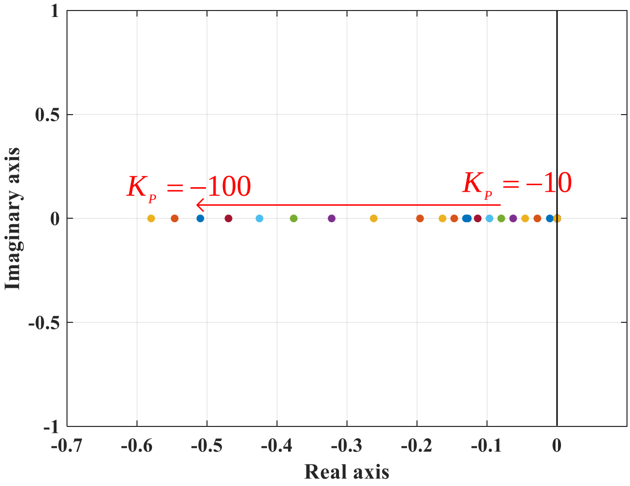

Fig. 2.18: Eigenvalues of the P matrix for negative values of of K_P and K_i = 600 [J1].

The Lyapunov function for stable the case studies are shown in Fig. 2.19.

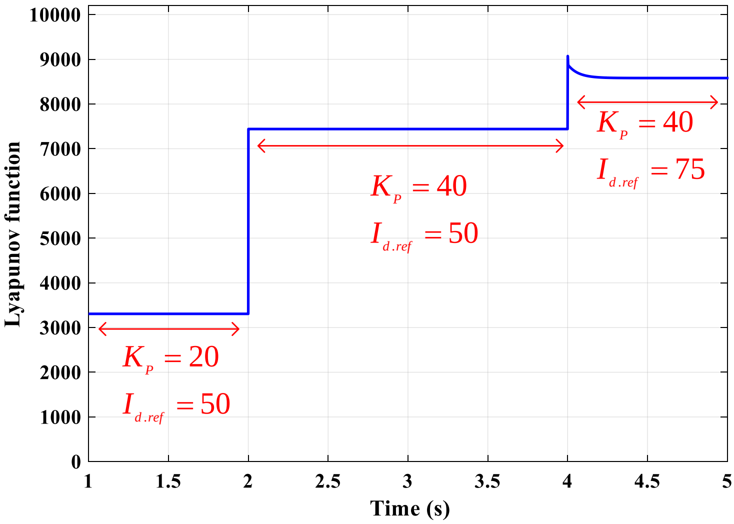

Fig. 2.19: Lyapunov function of the grid-connected VSC considering different values of the K_P and a step change in the reference current at t = 4 s [J1].

The output current for a step change in the current reference for the relevant case study is shown in Fig. 2.20.

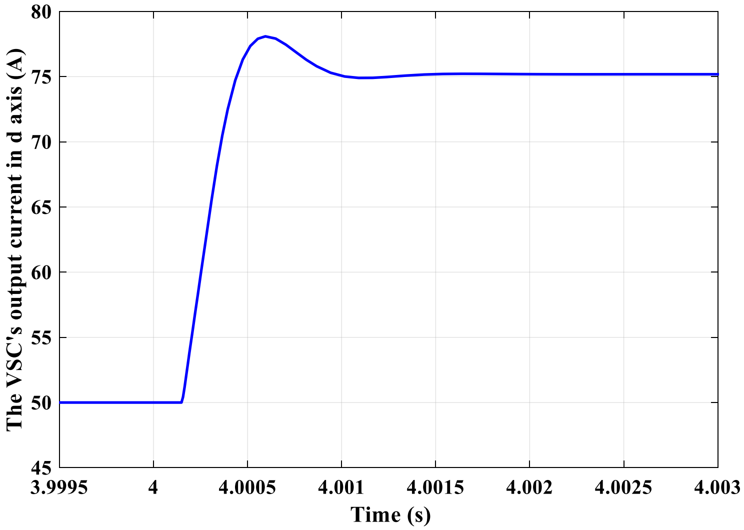

Fig. 2.20: The VSC's output current response to the step change in current reference from 50 A to 75 A at t = 4 s with K_p = 40 [J1].

The Lyapunov function for an unstable case is shown in Fig. 2.21, while its time-domain simulation is shown in Fig. 2.22. For this case, the current reference maintain 50 A, while the K_P is changed from 70 to 140 at $t = 2\ s$. It can be seen from Fig. 2.17 that for that for K_P more than 134, the system is unstable. The energy function is calculated by $V = \mathbf{x}\mathbf{x}^{\mathbf{T}}$, where **P** considered to be 1. More simulation results are shown in [J1].

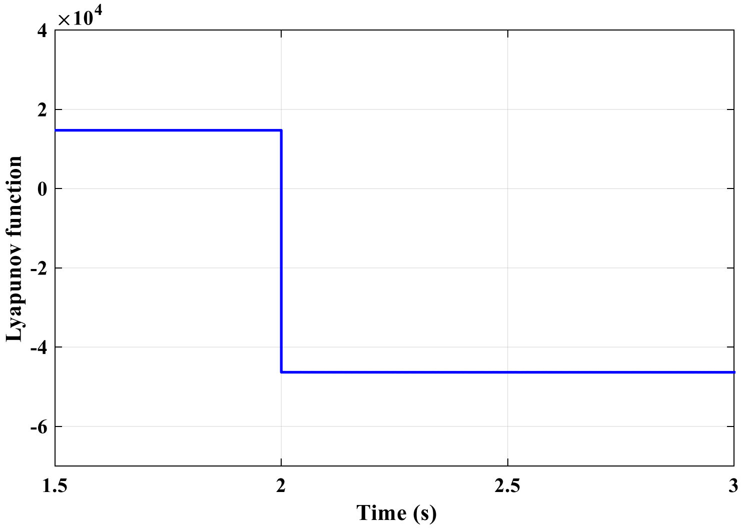

Fig. 2.21: Lyapunov function of the system with $I_{d.ref}$ = 50 A and change in K_p from 80 to 160 at t = 2 s [J1].

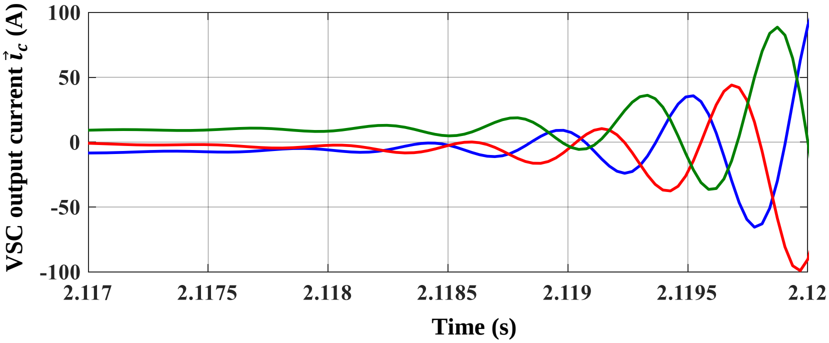

Fig. 2.22: The VSC's output current for the unstable case study, which is related to a step change in K_P value from 80 to 160 at $t = 2\ s$ [J1].

2.5.3. Modeling and Adaptive Design of the SRF-PLL: Nonlinear Time-Varying Framework

Next, to make the analysis more realistic and complete, the PLL large-signal stability assessment should be added to the analysis. The estimated phase angle can be calculated as follows using the PLL operation shown in Fig. 2.3(b):

$$\hat{\theta} = \int \left[V_{pcc} K_p \sin\left(\theta - \hat{\theta}\right) + K_i \int V_{pcc} \sin\left(\theta - \hat{\theta}\right) dt + \omega_n \right] dt \qquad (2.31)$$

To assess the large-signal stability of the SRF-PLL, a large disturbance in the input signal is considered. All variables ($\hat{V}_{pcc}$, $\hat{\omega}$, $\hat{\varphi}$, and $\hat{\theta}$) can be considered as the case studies. However, the SRF-PLL can be normalized to its input's magnitude, so it will be insensitive to $\hat{V}_{pcc}$. On the other hand, $\hat{\varphi}$ and $\hat{\theta}$ are dependent variables. Hence, only changes in $\hat{\omega}$ and $\hat{\theta}$ are considered in the case studies. A change in θ is considered as a phase jump, and change in ω is considered as the frequency deviation.

Considering the phase jump as the input, the model can be rewritten as follows:

$$\ddot{\hat{\theta}} = \left(\dot{\theta} - \dot{\hat{\theta}}\right) V_{pcc} K_p \cos\left(\theta - \hat{\theta}\right) + V_{pcc} K_i \sin\left(\theta - \hat{\theta}\right). \tag{2.32}$$

By defining $x_1 = \left(\theta - \hat{\theta}\right)$ and $x_2 = \left(\dot{\theta} - \dot{\hat{\theta}}\right)$, the model can be represented as follows:

$$\begin{cases} \dot{x}_1 = x_2 \\ \dot{x}_2 = -\left[V_{pcc} K_p x_2 \cos\left(x_1\right) + V_{pcc} K_i \sin\left(x_1\right)\right]. \end{cases} \tag{2.33}$$

However, if the frequency deviation is considered as a disturbance in the input, the model can be represented as follows:

$$\hat{\omega} = \omega_n + \left(K_p + K_i \int \right)\left[V_{pcc} \sin\left(\omega t - \hat{\omega} t\right)\right] \tag{2.34}$$

which leads to:

$$\dot{\hat{\omega}} = \dot{\omega} + \left[\frac{V_{pcc} K_p \left(\omega - \hat{\omega}\right) \cos\left(\omega t - \hat{\omega} t\right)}{1 + V_{pcc} K_p t \cos\left(\omega t - \hat{\omega} t\right)} + \frac{V_{PCC} K_i \sin\left(\omega t - \hat{\omega} t\right) - \dot{\omega}}{1 + V_{pcc} K_p t \cos\left(\omega t - \hat{\omega} t\right)} - \frac{\dot{\omega}}{1 + V_{pcc} K_p t \cos\left(\omega t - \hat{\omega} t\right)}\right]. \tag{2.35}$$

The large-signal stability assessment of the PLL can be derived based on the aforementioned models. However, before getting to that point, it is worth to take a look at the phase portrait of the nonlinear model of the PLL as shown in Fig. 2.23.

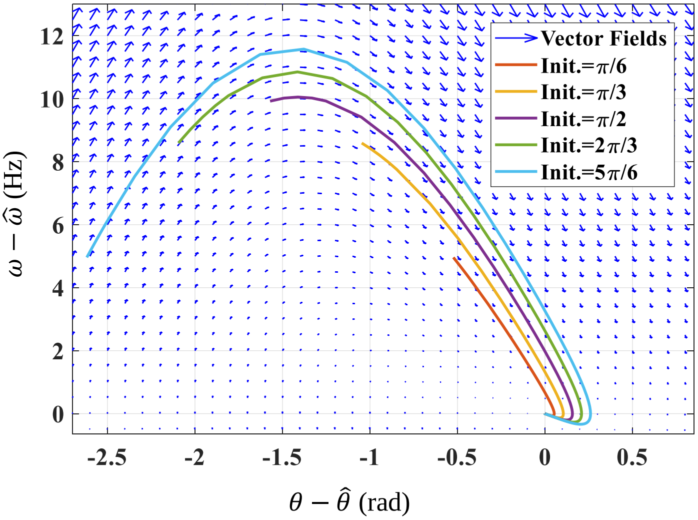

Fig. 2.23: Phase portrait of a phase jump state trajectory of the nonlinear model of the PLL described in (2.33) for different initial values (Init.) of the phase jump [J2].

As it can be seen from Fig. 2.23, no matter where the initial value for the phase jump is, the state trajectories will always become stable in infinite time. However, for the frequency deviation in the input signal, the following limitations should be calculated. Considering (2.35**)**, if the system becomes stable after the transient, then $\dot{\hat{\omega}} - \dot{\omega} = 0$, which leads to the following equation:

$$\lim_{t\to\infty}\left[\frac{V_{PCC}K_p\left(\omega-\hat{\omega}\right)\cos\left(\omega t-\hat{\omega}t\right)}{1+V_{PCC}K_p t\cos\left(\omega t-\hat{\omega}t\right)}+\frac{V_{PCC}K_i\sin\left(\omega t-\hat{\omega}t\right)-\dot{\omega}}{1+V_{PCC}K_p t\cos\left(\omega t-\hat{\omega}t\right)}-\frac{\dot{\omega}}{1+V_{PCC}K_p t\cos\left(\omega t-\hat{\omega}t\right)}\right]=0.$$

(2.36)

Considering the stable mode for the PLL, the infinite value of *t* will be much larger than ω, $\widehat{\omega}$, and their deviation. With this in mind, the second and third terms in **(2.36)** are zero. Then, **(2.36)** can be simplified as follows:

$$\lim_{t\to\infty}\frac{V_{PCC}K_p\left(\omega-\hat{\omega}\right)\cos\left(\omega t-\hat{\omega}t\right)}{1+V_{PCC}K_p t\cos\left(\omega t-\hat{\omega}t\right)}=\lim_{t\to\infty}\frac{\omega-\hat{\omega}}{t}=0. \tag{2.37}$$

If the frequency deviation can be modeled as a first-order function, then the system will be stable. However, for the order more than one, a nonlinear stability analysis technique should be used to evaluate the system stability.

To evaluate the global stability of the SRF-PLL control system shown in Fig. 2.3, a Lyapunov function can be used as follows:

$$V = \frac{1}{2}\mathrm{P}\left(\hat{\omega} - \omega\right)^2 \tag{2.38}$$

Considering (2.35) and (2.38),the Lyapunov function derivative with respect to a time can be calculated as follows:

$$\dot{V} = \left[\mathrm{P}\left(\hat{\omega} - \omega\right)\right] \times \left[\frac{V_{pcc}K_p\left(\omega - \hat{\omega}\right)\cos\left(\omega t - \hat{\omega}t\right) + V_{pcc}K_i\sin\left(\omega t - \hat{\omega}t\right) - \dot{\omega}}{1 + V_{pcc}K_p t\cos\left(\omega t - \hat{\omega}t\right)}\right] \tag{2.39}$$

which leads to:

$$\dot{V} = \underbrace{\frac{-\mathrm{P}V_{pcc}K_p\left(\hat{\omega} - \omega\right)^2\cos\left(\left(\omega - \hat{\omega}\right)t\right)}{1 + V_{pcc}K_p t\cos\left(\omega t - \hat{\omega}t\right)}}_{-} + \underbrace{\frac{\mathrm{P}V_{pcc}K_i\left(\hat{\omega} - \omega\right)\sin\left(\left(\omega - \hat{\omega}\right)t\right)}{1 + V_{pcc}K_p t\cos\left(\omega t - \hat{\omega}t\right)}}_{-} + \underbrace{\frac{-\mathrm{P}\dot{\omega}\left(\hat{\omega} - \omega\right)}{1 + V_{pcc}K_p t\cos\left(\omega t - \hat{\omega}t\right)}}_{+}. \tag{2.40}$$

For the positive and negative value of $\dot{\omega}$, the following inequality can be obtained:

$$\frac{\dot{\omega} - V_{pcc}K_p\left(\omega - \hat{\omega}\right)}{V_{pcc}K_i\left(\omega - \hat{\omega}\right)} \leq t. \tag{2.41}$$

By multiplying both sides of the inequality in (2.41) to $\left|V_{pcc}K_i(\omega - \hat{\omega})\right|$, it can be rewritten as follows:

$$\left|\dot{\omega}\right| \leq K_p\left|V_{pcc}\left(\omega - \hat{\omega}\right)\right| + K_i t\left|V_{pcc}\left(\omega - \hat{\omega}\right)\right|. \tag{2.42}$$

In this manner, for a conservative case, to satisfy the Lyapunov stability constraints, the following inequality should be satisfied:

$$\left|\dot{\omega}\right| \leq K_p V_{pcc}\left|\omega - \hat{\omega}\right|. \tag{2.43}$$

This means that if the inequality in **(2.43)** is satisfied, the system will remain stable. In this manner, a modified SRF-PLL is proposed in [J2], which is also shown in **Fig. 2.24**, where λ_{fc} is an adaptive gain (which is a real positive number). $\widehat{\omega}$ and $\hat{\delta}$ are the estimated frequency and the estimated initial phase of the input signal. λ_{fc} acts as a gain that damps the transient fluctuation of the estimated frequency, as it is later shown and discussed in Fig. 2.28 and Fig. 2.29.

By applying the proposed adaptive SRF-PLL, the following inequality is satisfied, which leads to global stability:

$$1 \leq \frac{K_p V_{pcc}\left|\theta - \hat{\theta}\right|}{\left|\omega\right|}. \tag{2.44}$$

More results are presented in [J2]. It is worth mentioning that the adaptive gain shown in **Fig. 2.24** will become smaller and smaller as the estimated phase angle gets closer to its actual value. This means that the proposed adaptive SRF-PLL will act as a common SRF-PLL in the steady-state mode of the system.

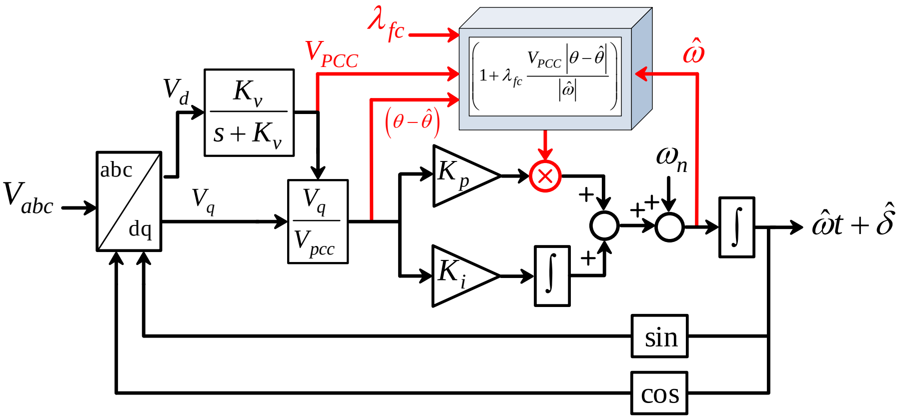

Fig. 2.24: Block diagram of the proposed adaptive SRF-PLL [J2].

The estimated frequency by the SRF-PLL, shown in Fig. 2.3, with different phase jumps are shown in Fig. 2.25.

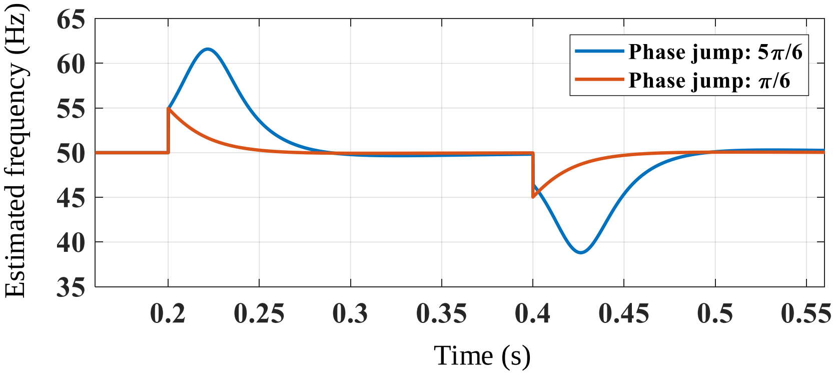

Fig. 2.25: Time domain simulations of the SRF-PLL subjected to different phase jumps for system shown in Fig. 2.3 [J2].

Experimental tests for the same scenarios are shown in Fig. 2.26 and Fig. 2.27.

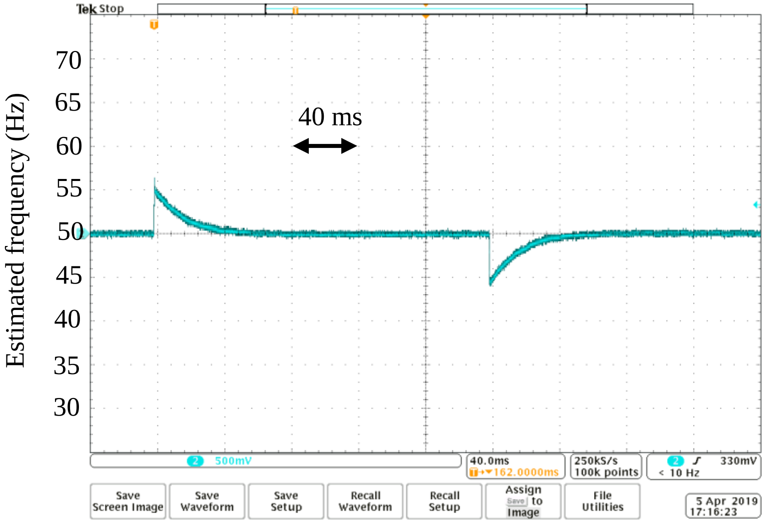

Fig. 2.26: The SRF-PLL estimated frequency for different phase-jumps (experimental results). π/6 phase jump implement to the PLL and it is cleared after 200 ms [J2].

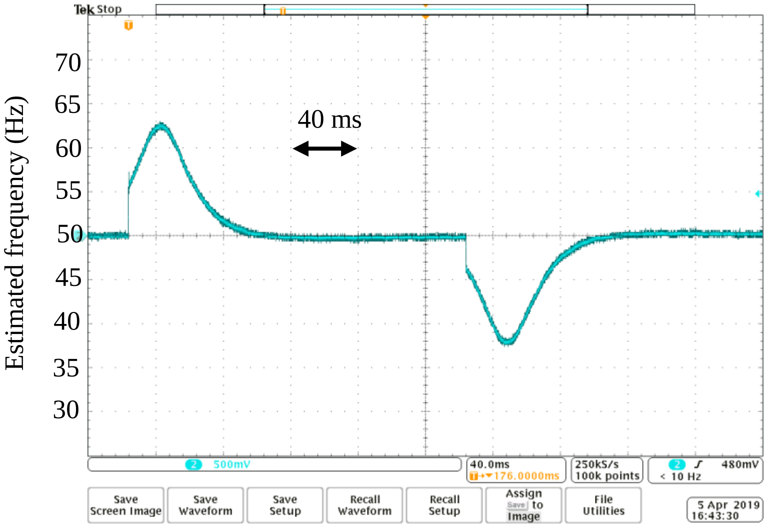

Fig. 2.27: The SRF-PLL estimated frequency for different phase-jumps (experimental results). 5π/6 phase jump implement to the PLL and it is cleared after 200 ms [J2].

By using the adaptive SRF-PLL, the performance of the system improved as shown in Fig. 2.28 and Fig. 2.29. Its experimental verification are presented in [J2]. In Fig. 2.28, the frequency is estimated by the standard SRF-PLL as shown in Fig. 2.3 (green dashed line), and also it is estimated by the adaptive SRF-PLL shown in Fig. 2.24 with two different adaptive gain values. For this case study, the input frequency is changed from 50 Hz to 48.5 Hz within 0.01 s. In Fig. 2.29, the same conventional SRF-PLL and the adaptive SRF-PLL is tested for 30º phase jump in the input. As it can be seen from Fig. 2.28 and Fig. 2.29, the input frequency estimation is improved by using the adaptive SRF-PLL in comparison with the conventional one. Values for λ_{fc} are chosen randomly, however, this can be tuned for a specific case study.

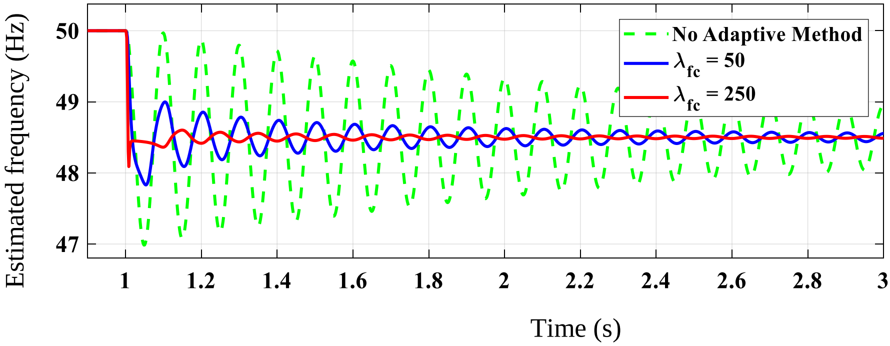

Fig. 2.28: Estimated frequency by the SRF-PLL for second-order input frequency deviation from t = 1 s to t = 1.01 s using the proposed adaptive tuning method with different damping factors [J2].

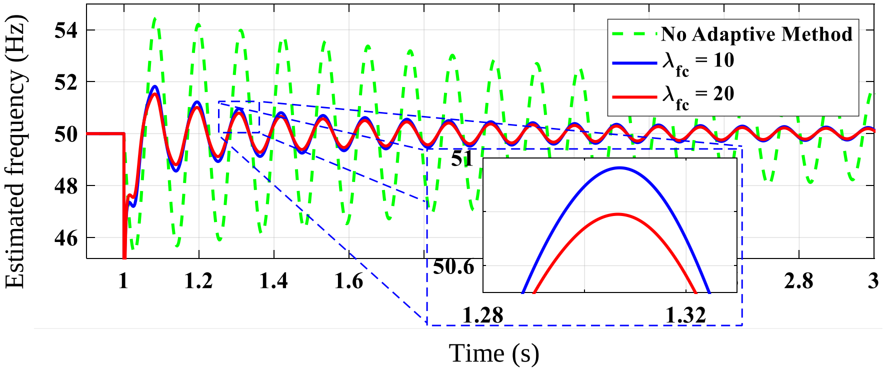

Fig. 2.29: Estimated frequency by the SRF-PLL for 30º phase jump at t = 1 s using the proposed adaptive tuning method with different damping factors [J2].

2.6. Summary

Grid-feeding power converters are becoming more popular in power systems, and this chapter study the large-signal stability of the grid-tied VSCs. It starts with highlighting the importance of grid-feeding power converters stability assessment. Then, align with the main focus of this Ph.D. project, a large-signal model of the grid-tied VSC using the Lyapunov stability theory is presented. Furthermore, the SRF-PLL nonlinear model stability is analyzed by using the portrait phase concept and the Lyapunov theory. In addition, two nonlinear stability assessment techniques are discussed, as they are used for large-signal stability analysis of the nonlinear models.

Related Publications

J1. **B. Shakerighadi**, E. Ebrahimzadeh, F. Blaabjerg, and C. L. Bak, ‘‘Large-signal stability modeling for the grid-connected VSC based on the Lyapunov method,’’ in Energies, vol. 11, p. 2533, Oct. 2018.

Main contribution:

In this paper, the large-signal model of the grid-tied VSC based on its Lyapunov function is proposed. The time delay caused by the PWM switching is also considered in the model. A systematic approach is developed to find the parametric Lyapunov function of the grid-tied VSC.

J2. **B. Shakerighadi**, E. Ebrahimzadeh, M. G. Taul, F. Blaabjerg and C. L. Bak, "Modeling and Adaptive Design of the SRF-PLL: Nonlinear Time-Varying Framework," in IEEE Access, vol. 8, pp. 28635-28645, 2020.

Main contribution:

In this paper, a non-linear time varying (NTV) model of the PLL is developed in order to assess the large-signal stability of it. Both the phase portrait method and the Lyapunov function are used to analyze the PLL large-signal stability. An adaptive model of the SRF-PLL is proposed to improve its performance for large disturbances.

C1. **B. Shakerighadi**, E. Ebrahimzadeh, F. Blaabjerg and C. L. Bak, "Lyapunov- and Eigenvalue-based Stability Assessment of the Grid-connected Voltage Source Converter," 2018 IEEE International Power Electronics and Application Conference and Exposition (PEAC), Shenzhen, 2018, pp. 1-6.

Main contribution:

The stability of the grid-tied VSC is assessed by using two methods: A small-signal stability and the large-signal stability. It is shown that for a grid-tied VSC, how the second order Lyapunov function should be defined. It is shown that in analyzing a linear system, the large-signal stability assessment leads to the same result as small-signal methods.

C2. **B. Shakerighadi**, E. Ebrahimzadeh, C. L. Bak and F. Blaabjerg, " Large Signal Stability Assessment of the Voltage Source Converter Connected to a Weak Grid," Proceedings of Cigre Symposium Aalborg 2019, 2019, pp. 1-12.

Main contribution:

In this paper, the impact of the weak grid on the large-signal stability of the system is modeled and is assessed.

Chapter 3.
Large-Signal stability of Power-electronic-based power systems

3.1. Abstract

In this Chapter, relevant topics regarding the security and the large-signal stability of large-scale the PE-based power systems are presented. The chapter starts with proposing a guideline for security assessment of modern power systems. Then, a discussion regarding the inertial response of a single grid-tied VSC is presented. Finally, a proposed method for the large-signal stability assessment of PE-based power systems is presented, where a method to aggregate inertia is presented.

3.2. Background and motivation

PE-based units play an important role in modern power systems stability, security, and reliability assessments [6], [53]. Increasing the penetration of PE-based energy sources, such as wind turbines and photovoltaics, introduces new challenges in stability and security of power system [76]. It is interesting to know how the maximum penetration of PE-based energy sources should be determined for a power system in order to make sure that system remains stable for a credible contingency [42]. Talking about a credible contingency, the assessment of large disturbances in PE-based power systems needs a more careful consideration and analysis to have a better understanding of the grid stability. The main goal of this chapter is to analyze how a large disturbance can affect a PE-based power system stability. A key point is the system inertial response, due to the increase the PE-based unit's penetration, the system equivalent inertia will decrease as it is discussed later.

3.3. Security Assessment of PE-based Power Systems

As the scale of the power systems increases from a grid-tied VSC to a large-scale power system, the large-signal stability assessment needs to use a different approach. In respect to the single grid-tied VSC, a detailed control system model can be used to assess the stability; however, in large-scale power systems, the grid behavior is more important than the detailed model of the system. The reason is that using the detailed model of the large-scale power system is impractical, while, it might be of importance for the system stability analysis. Besides, most often, the detailed model of the power systems, including all component details, is not available[1].

As mentioned previously, the stability challenges of modern power systems[2] may lead to blackouts [28], [103], which is not only important from the stability point of view, but it is also a great deal for the system security. An overall schematic of the security assessment of power systems with a high penetration of PE-based units is shown in Fig. 3.1.

The power systems security is defined as its ability to maintain its stability when it is subjected to a contingency [27]. Based on that, the modern power system security analysis can be categorized as shown in Fig. 3.2, where it is divided into three categories: static security, dynamic and transient security, and cyber security. In static security, static constraints of the system in its normal condition and when it is subjected to a contingency are checked. Regarding the dynamic and transient security, system oscillatory modes and transient stability during the normal and contingency conditions are checked. The cyber security assessment of modern power systems is related to its ability to remain stable when it is subjected to a cyber-attack like false data injection [97]. The first two security subcategories are studied here, and the cyber-security assessment is trended as out of the scope of this project but becomes more and more important.

---

[1] Most often, renewable energy-related companies, such as wind turbine manufacturers, are not willing to share their product models with system operators (or anyone out of their companies), due to the market competition and technology. In this circumstance, although specific grid codes are required from wind turbine manufacturers, the system operators do not have the full model of the system, and they are analyzing the grid stability based on their knowledge of the system model that they have. Therefore, this makes the system operators to rely on the system variables that could be measured, like the bus voltages and the system frequency, rather than the detailed system models.

[2] Stability challenges of the power system are categorized into three main subcategories: rotor angle stability, frequency stability, and voltage stability.

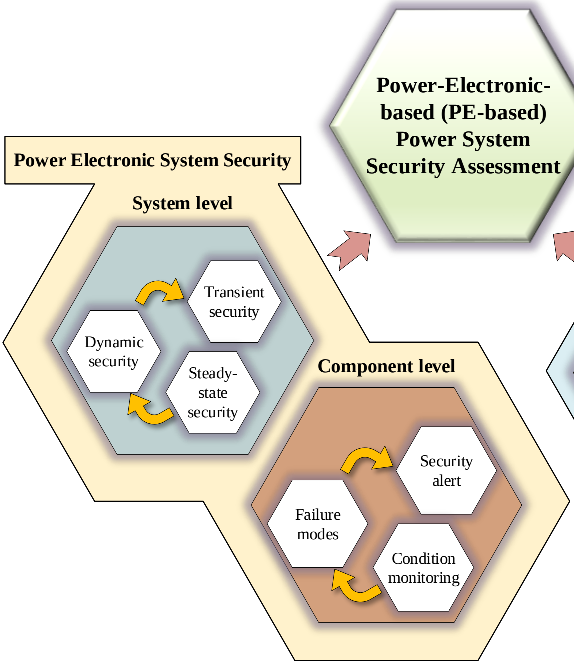

Fig. 3.1: Overall schematic of the security assessment of power systems with a high penetration of PE-based units [J3].

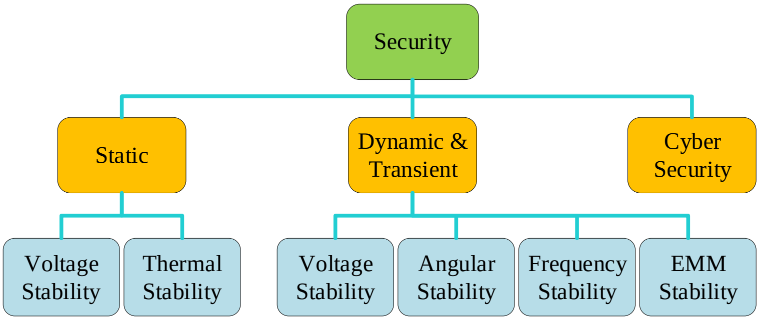

Fig. 3.2: Power system security assessment categories including both static and dynamic analysis [J3].

A guideline for the security assessment of the PE-based power systems is proposed and it is shown in Fig. 3.3 and Fig. 3.4. In this guideline, the importance of PE-based units on the system security is highlighted. The security assessment of PE-based power systems may be done in three steps: static security assessment, dynamic security assessment, and the transient security assessment. In the static security assessment, just like the security assessment of the conventional systems, the load flow of the system in its normal condition as well as N-1 contingency situation is derived to check the static security constrains. The static security constrains, for instance, include the line thermal constrains and their maximum transferrable active power. If the system passes all the static security checks, then the dynamic security constrains of the system should be checked. In this phase, first a small-signal model of the system in the normal operation and N-1 contingency conditions are used to further check the oscillatory modes of the system. If all oscillatory modes of the system are damped both locally and globally, then the system is dynamically secure. Next, the transient security of the system should be checked. At this stage, the transient stability of the system is subjected to a large (and small) disturbances and should be analyzed, and if the system provides sufficient response that meets the grid codes, then the system is called transient secure. This process is shown in Fig. 3.3 and Fig. 3.4, respectively.

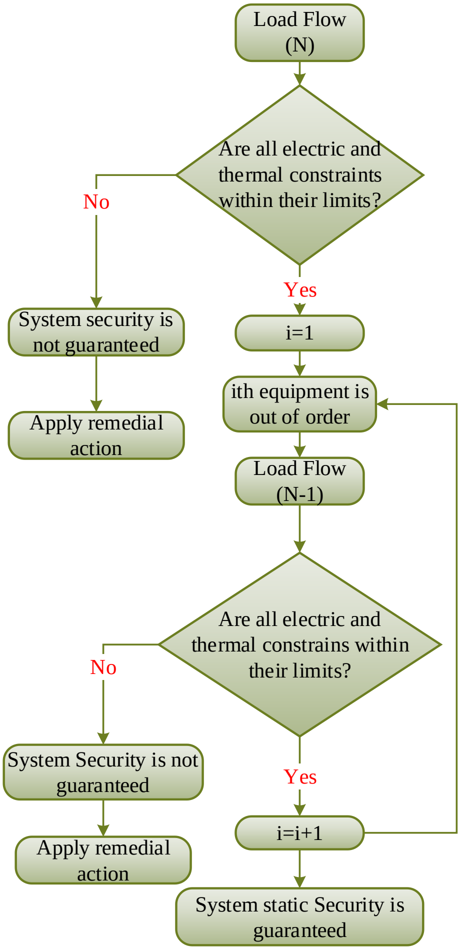

Fig. 3.3: PE-based power system security assessment: Static security assessment [J3].

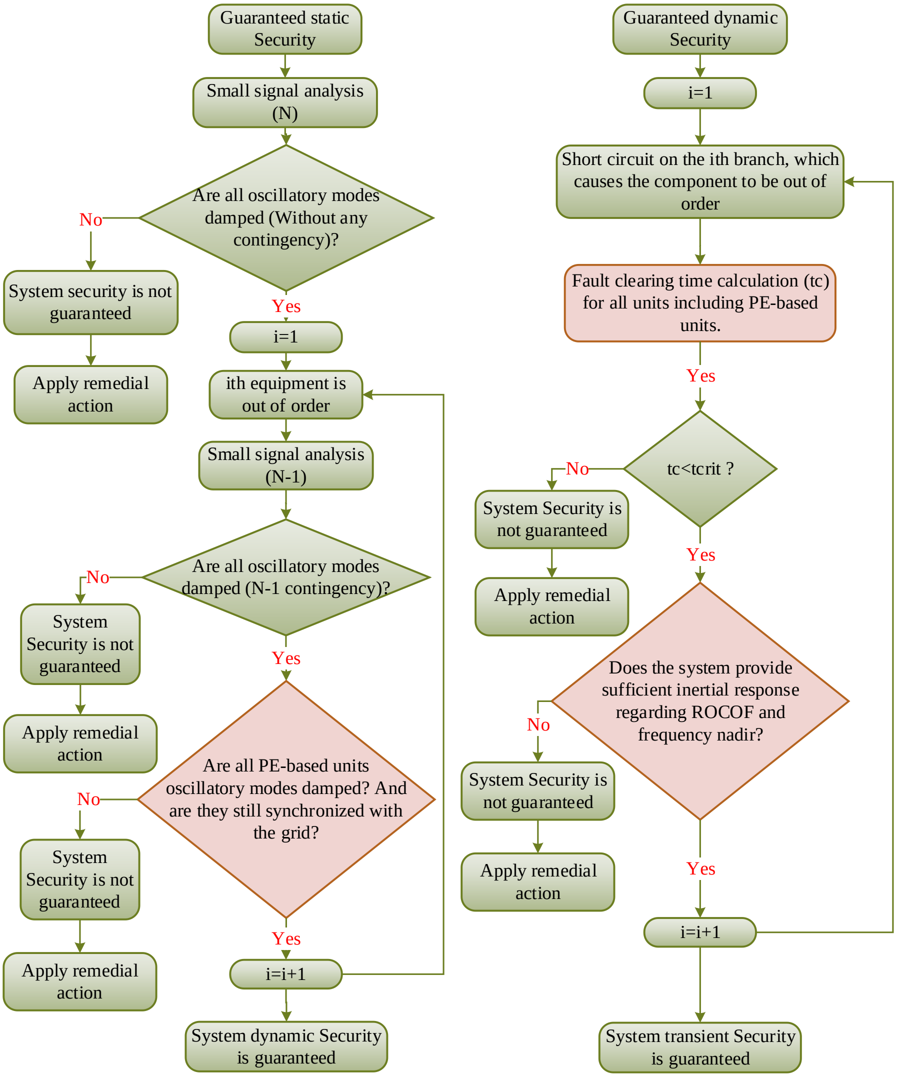

(a) (b)

Fig. 3.4: PE-based power system security assessment: (a) dynamic security assessment, (b) and transient security assessment [J3].

In order to demonstrate the guidelines introduced in Fig. 3.3 and Fig. 3.4, a three-phase fault in the IEEE 39-bus test systems, shown in Fig. 3.5, is studied to show the performance of a PLL [104]. The synchronous generator sizes are presented in . Here, the transient security is discussed as an illustrative example. A three-phase fault in the middle of line 22-23 for 100 ms is triggered in order to study the impact of the large disturbance on the grid-tied VSC. In this scenario, it is assumed that instead of the generator connected at bus 22, a wind turbine with the same power rating is substituted. The wind turbine is modeled as a grid-feeding power converter as discussed in 2.5. The voltage magnitude and phase angle at bus 22 are shown in Fig. 3.6. As it can be seen from Fig. 3.6(b), a three-phase short circuit fault causes a 20º phase angle change at bus 22. The PLL response for the aforementioned fault at line 22-23 is shown in Fig. 3.7, where a 20º phase angle deviation leads to a more than 3 Hz frequency estimation error. If the protection system of the PE-based unit is sensitive to this frequency deviation, the unit may be disconnected from the system as a result of a false frequency estimation [67]. As it is mentioned before, this simulation is presented as an illustrative example. More details are discussed later in Scenario 1-3.

Table 3.1: IEEE 39-bus test system generator sizes.

Generator	**Type**	**Size**		
		Rating power [MVA]	Active power [MW]	Voltage magnitude at the output terminal [p.u.]
G1	PV	10000	1000	1.03
G2	Slack	630	0	0.982
G3	PV	720	585	0.9831
G4	PV	720	568	0.9972
G5	PV	270	229	1.0123
G6	PV	720	585	1.0493
G7	PV	630	504	1.0635
G8	PV	900	747	1.0278
G9	PV	1000	830	1.0265
G10	PV	1000	250	1.0475

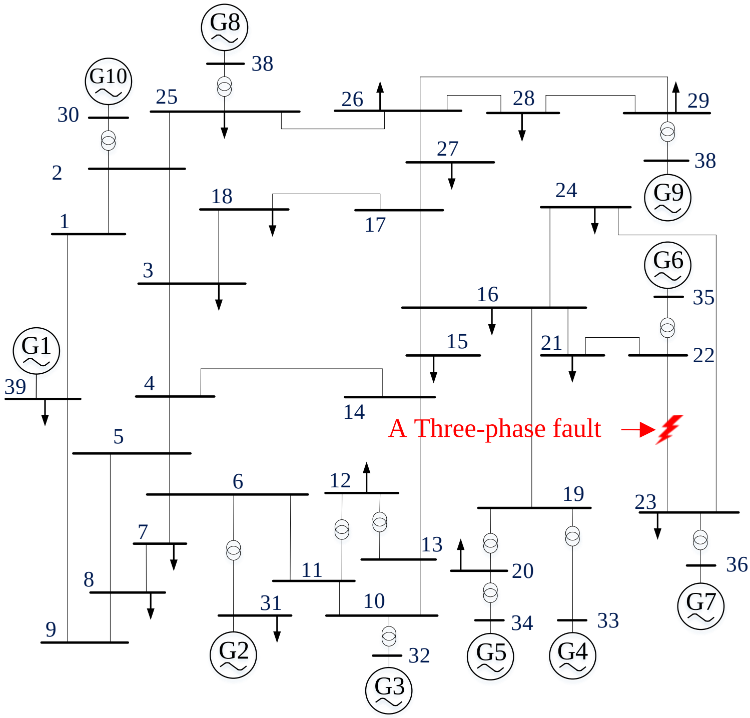

Fig. 3.5: IEEE 39-bus test system used for security assessment, where a three-phase short circuit is indicated in the middle of line 22-23 [104]**.**

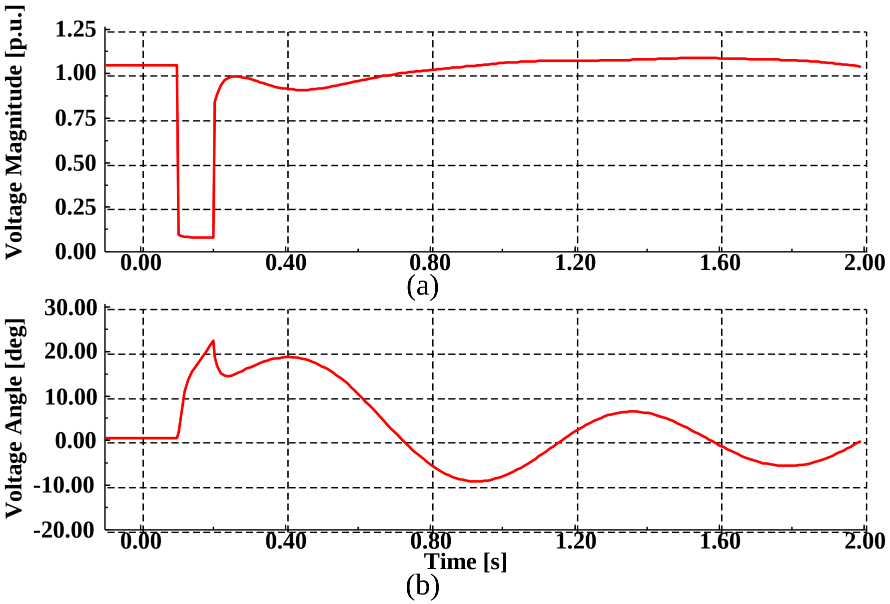

(a)

(b)

Fig. 3.6: Bus 22 (a) voltage phase angle, (b) and its voltage magnitude, for a three-phase fault happening at *t* = 100 ms, and cleared at *t* = 200 ms [C3].

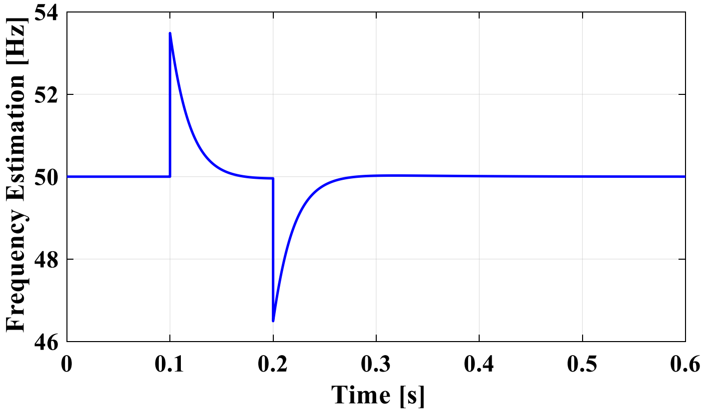

Fig. 3.7: Frequency estimation of the PLL for 20°-phase-jump at t = 100 ms caused by a near three-phase fault, which is cleared at t = 200 ms [C3].

Three scenarios are discussed in this system to show the impact of increasing the PE-based units' penetration in power systems. The first scenario explains the conventional stability issues, while in the next two scenarios the grid stability with different NSG penetration levels is discussed. Case studies are derived on the same IEEE 39-bus test system and developed in DigSILENT PowerFactory, like shown in

Fig. 3.5. For these scenarios, the NSG is considered as a fully controlled wind turbine that has a current controller, active and reactive power controller, active power reduction for the over-frequency, and two PLLs as shown in **Fig. 3.8**. One PLL is used for estimating system phase angle that is used for the current controller and the other one (that is slower than the first PLL) is used for measuring the frequency for over-frequency active power reduction. It should be mentioned that the over-frequency active power reduction will not be activated in Scenario 1 to 3 due to low over frequency. Accordingly, the wind turbine controller can be simplified as a current controller and active and reactive power controllers, which represents a grid-feeding power converter discussed in **Chapter 2**. The wind turbine controller parameters used here for the simulation are given in **Table 3.2**. There are also more specific details regarding the wind turbine controller that is used here, which is presented in [105]. It is also should be mentioned that the size of the wind turbine is considered as if it replaced with a synchronous generator, it produce the same rating power. To do so, for instance, to replace a 600 MVA synchronous generator, 240 wind turbines with 2.5 MVA rating power that are connected in parallel, are used. In this way, the same steady-state behavior will be presented by changing the NSG penetration, however, a different dynamic response is introduced.

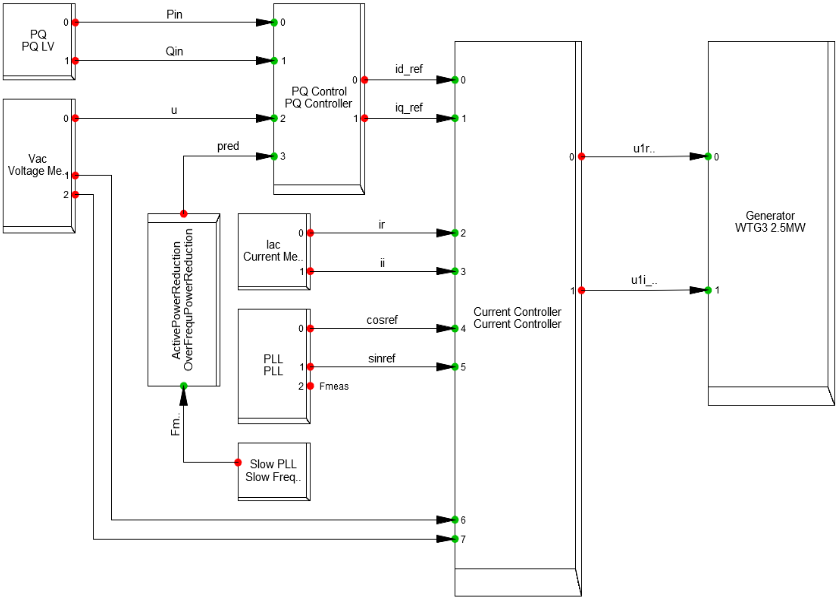

Fig. 3.8: Wind turbine control block diagram used in the IEEE 39-bus test system for the security assessment of the grids with different level of NSG penetration.

Table 3.2: Wind turbine current controller and active and reactive power controllers parameters.

Controller parameter	**value**	**Description**
K_q	1	Gain reactive current controller [-]
T_q	0.002	Integrator time constant reactive current controller [s]
K_d	1	Gain active current controller [-]
T_d	0.002	Integrator time constant active current controller [s]
K_p	0.5	Active power control gain [p.u.]
T_p	0.002	Active power control time constant [s]
K_q	0.5	Reactive power control gain [p.u.]
T_q	0.02	Reactive power control time constant [s]
i_{max}	1	Current magnitude limit [p.u.]

Scenario 1: Conventional power system

In this scenario, it is assumed that all generators are based on conventional energy sources (synchronous generators). G2 is considered as the reference synchronous machine. A generation trip is studied for all case studies. Here, G5 is tripped at t = 50 s and it is considered as the large disturbance. The voltage magnitude at Bus 6, 25, and 28 as well as the system frequency are shown in Fig. 3.9 and Fig. 3.10, respectively. Fig. 3.10 presents the frequency response of the system, where the synchronous generators' governor response is shown in Fig. 3.10(a). It is worth mentioning that the governor response is slower than the inertial response of the synchronous generator [106].

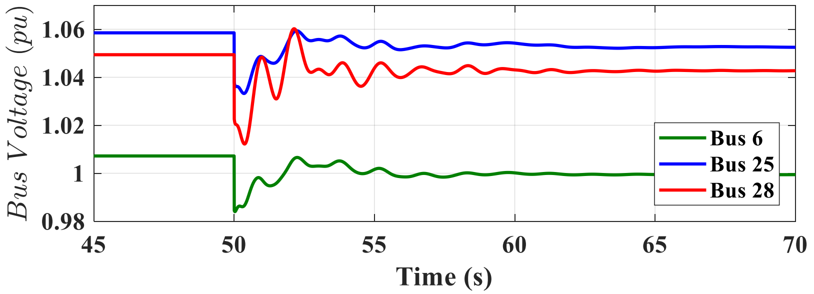

Fig. 3.9: Bus 6, 25, and 28 voltage magnitude response to G5 trip at t = 50 s for the conventional power system case study (Scenario 1) [J3].

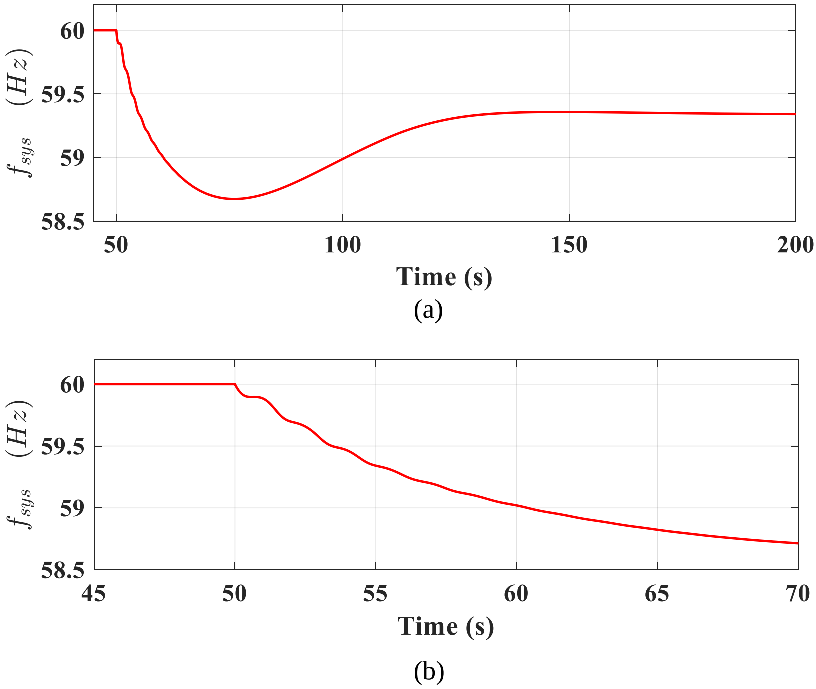

(a)

(b)

Fig. 3.10: System frequency response to the G5 trip at t = 50 s (a) including the governor response, and (b) zoom in figure with the same time scale of Fig. 3.9 (Scenario 1) [J3].

As it can be seen from **Fig. 3.10**, the loss of generation causes imbalance between the load and generation that leads to drop in frequency. This means that rotor speed in the other generators drop right after the fault occur with respect to each generator's inertia. However, this event converge to a new stable operating point. This large disturbance causes a fluctuation in voltage magnitude of grid nodes as shown in Fig. 3.9.

Scenario 2: PE-based power systems with a penetration level of 11.2%

In this scenario, instead of G4, a wind farm with the same power rating is substituted. The NSG penetration is 11.2% for this case study. The NSG used here is the wind turbine, which model is presented in Fig. 2.1, and also discussed in [105], where active and reactive current controller proportional gains are 1 and its integrator time constants for active and reactive powers are 0.002. The voltage magnitudes at Bus 6, 25, and 28 and system frequency are shown in Fig. 3.11 and Fig. 3.12 for the same event of that discussed in Scenario 1, respectively.

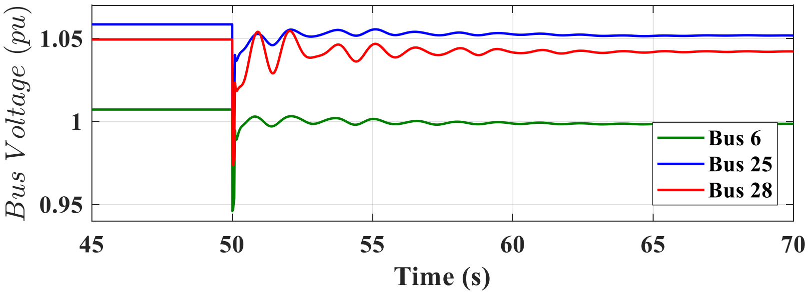

Fig. 3.11: Bus 6, 25, and 28 voltage magnitude response to generator 5 trip at t = 50 s for the PE-based power system case study (Scenario 2) [J3].

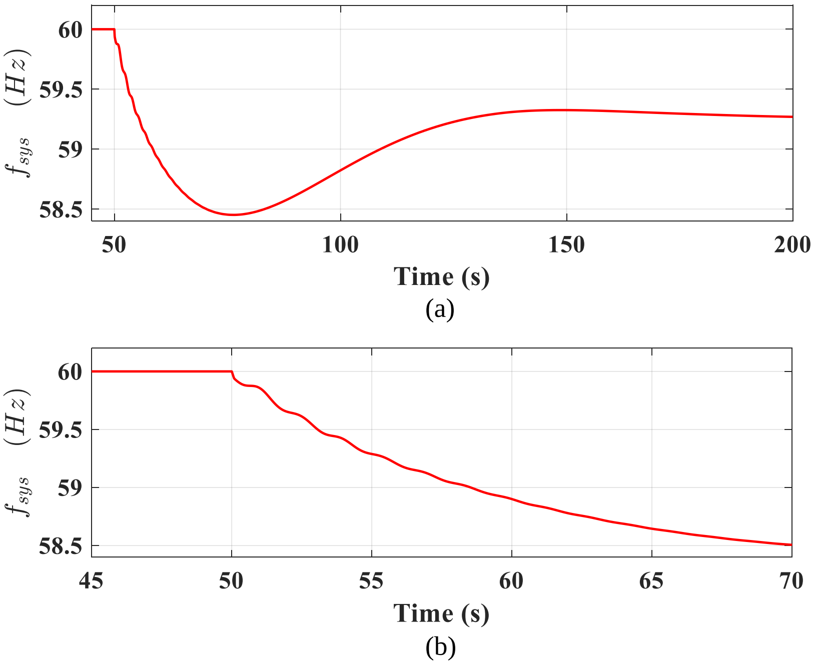

Fig. 3.12: The PE-based power system frequency response to the generator 5 trip at t = 50 s for the PE-based power system Case study (a) including the governor response, and (b) zoom in figure with the same time scale of Fig. 3.11 (Scenario 2) [J3].

The equivalent inertia of the grid with 11.2% wind turbine penetration is less than the grid with 100% synchronous generators. A proposed method to determine the equivalent grid inertia is discussed later in this chapter; however, It can be seen that a system with a higher penetration of RES has a lower inertial response. This can be seen by comparing Fig. 3.10 and Fig. 3.12, as the frequency nadir is lower in the case with a higher wind turbine penetration. The relatively low frequency nadir in Fig. 3.12 leads to a higher voltage magnitude fluctuation shown in Fig. 3.11, in comparison with the voltage magnitude fluctuation shown in Fig. 3.9. The grid is still stable in this case study, while it faces more voltage and frequency fluctuations in comparison with the case study discussed in Scenario 1.

Scenario 3: PE-based power systems with high penetration of wind power (43.6% penetration level)

In this scenario, G3, G4, G6, G7, and G8 are substituted with wind farms with the same power rating. The NSG penetration is 43.6% for this case study. The voltage magnitude at Bus 6, 25, and 28 and system frequencies are shown in Fig. 3.13 and Fig. 3.14, respectively.

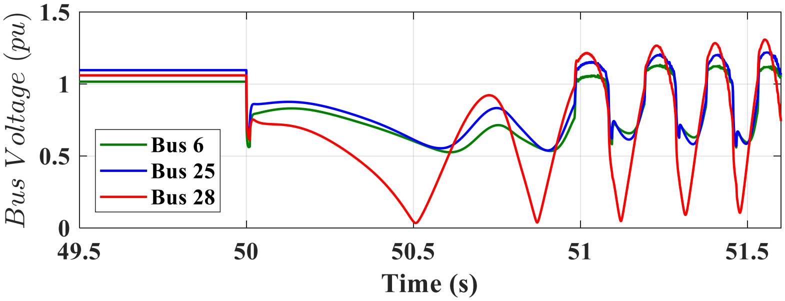

Fig. 3.13: Bus 6, 25, and 28 voltage magnitude response to G5 trip at t = 50 s for the system with high penetration of wind turbine (43.6%) (Scenario 3).

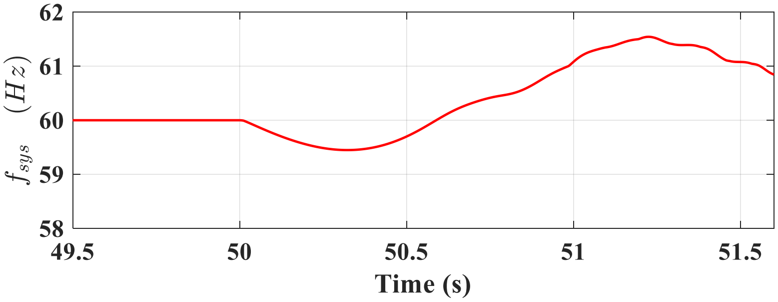

Fig. 3.14: The PE-based power system frequency response to the G5 trip at t = 50 s for the system with high penetration of wind turbine (43.6%) (Scenario 3) [J3].

As it can be seen from Fig. 3.13 and Fig. 3.14, the grid becomes unstable in this case study. The wind turbine penetration is relatively high (43.6%); however, the wind turbine penetration is not distributed in the grid at the same rate in all generation points. With the same penetration level of wind turbines in the grid for all generation points (G1-10), a higher penetration of wind turbine can be achieved without becoming unstable, as discussed in the next part.

Although the abovementioned analysis indicates stability challenges introduced by the increase of PE-based unit's penetration in power system, a mathematical model that describes the transient stability of such a system is needed, which is proposed in Section 3.5.

3.4. Semi-inertial response of the grid-feeding power converters

Although it has been mentioned in the literature that the grid-feeding power converter does not provide any inertial response, in this section the large-signal stability of the grid-tied VSC is assessed based on its semi-inertial response [7], [C4]. It should be mentioned that this chapter is dedicated to the large-signal stability of large-scale power systems, while the inertial response of a single grid-tied VSC is assessed in this section. The analysis of inertial response of a single grid-tied VSC is prerequisite for the inertial response of large-scale PE-based power systems, as it is studied in the next section.

Considering the grid-feeding power converter as it is shown in Fig. 2.4 and Fig. 2.5, the output active power and current can be given as follows:

$$\begin{cases} P_e = 3V_G I_d \cos\left(\delta\right) \\ I_d = \dfrac{V_G \sin\left(\delta\right)}{X_L} \end{cases} \tag{3.1}$$

where I_d is the output current of the VSC in the d-axis. Considering the aforementioned equations, the output power can be calculated as follows:

$$P_e = 1.5\frac{V_G^2}{X_L}\sin\left(2\delta\right). \tag{3.2}$$

Based on the current control loop, the VSC current can be determined as follows:

$$I_d = \left(K_P + K_i\int\ \right)\times\left(P^* - 1.5\frac{V_G^2}{X_L}\sin\left(2\delta\right)\right). \tag{3.3}$$

Based on that, the derivative of the phase angle can be determined as follows:

$$\dot{\delta} = \frac{K_i X_L\left(P^* - 1.5\dfrac{V_G^2}{X_L}\sin\left(2\delta\right)\right)}{V_G\cos\left(\delta\right) + 3K_P V_G^2\cos\left(2\delta\right)}. \tag{3.4}$$

Considering the following calculation for the second order derivative of the phase angle as:

$$\frac{d^2\delta}{dt^2}=\frac{d}{dt}\left(\frac{d\delta}{dt}\right)=\frac{d}{dt}\left(\dot{\delta}\right)=\frac{d\dot{\delta}}{d\delta}\times\frac{d\delta}{dt}=\frac{d\dot{\delta}}{d\delta}\times\dot{\delta}, \tag{3.5}$$

it can be calculated as follows:

$$\begin{aligned}\frac{d^2\delta}{dt^2}&=\left(K_i X_L\right)^2\left(P^*-1.5\frac{V_G^2}{X_L}\sin\left(2\delta\right)\right)\times\\&\left[\frac{\left(-3\frac{V_G^2}{X_L}\cos\left(2\delta\right)\right)\times\left(V_G\cos\left(\delta\right)+3K_PV_G^2\cos\left(2\delta\right)\right)}{\left(V_G\cos\left(\delta\right)+3K_PV_G^2\cos\left(2\delta\right)\right)^3}\right.\\&\left.+\frac{\left(V_G\sin\left(\delta\right)+6K_PV_G^2\sin\left(2\delta\right)\right)\times\left(P^*-1.5\frac{V_G^2}{X_L}\sin\left(2\delta\right)\right)}{\left(V_G\cos\left(\delta\right)+3K_PV_G^2\cos\left(2\delta\right)\right)^3}\right].\end{aligned} \tag{3.6}$$

By defining the following index based on the similar behavior of the synchronous generator's swing equation, called semi-moment of inertia (SMOI), the system stability can be diagnosed:

$$SMoI\left(\delta,V_G,t\right)=\frac{\left(P^*-P_e\right)}{\frac{d^2\delta}{dt^2}}. \tag{3.7}$$

For positive values of *SMoI*, the system is stable, while if the index becomes negative, the system is unstable. The stability margin is reached when *SMoI* equals zero. Considering the grid-feeding model presented in Fig. 2.4 and Fig. 2.5 with the configuration presented in Table 3.3, three case studies are done to assess the proposed mathematical model.

Table 3.3: System parameters of a grid-tied VSC [C4].

System parameter	Value	Explanation
L_f-filter	10 mH	An L-filter is considered at the output of the VSC to smooth the system output current.
L_g	0 mH-10 mH-100 mH	The 0 mH introduces the stiff grid, while 10 mH and 100 mH are used for the weak grid and very weak grid conditions, respectively.

		Considering $S_{base} = 15\,kVA$ and $V_{base} = 400\,V$, the SCR for 0 mH, 10 mH, and 100 mH equal infinite, 4 p.u., and 0.4 p.u., respectively.
V_g	400 V (rms phase to phase)	An ideal three-phase voltage source is used for assessing the inertial response.
System frequency	50 Hz	
T_s	10^{-4} s	The sampling frequency is 10 kHz.
S_{max}	15 kVA	Maximum apparent power (power level)

Case study 1: Impact of increasing the VSC output power on the system stability and its relation to the *SMoI* index

In this case study, the output power reference is changed from 4 kW to 14 kW, as shown in Fig. 3.15. As it can be seen from Fig. 3.16, the output power follows its reference. However, as the output power gets closer to the maximum transferrable active power, the *SMoI* index decreases, which means that the operating point is getting closer to its stability margin[3].

---

[3] The definition of the maximum transferrable active power is discussed in Section 2.5.1, specifically in (2.22). The same concept is used here as well.

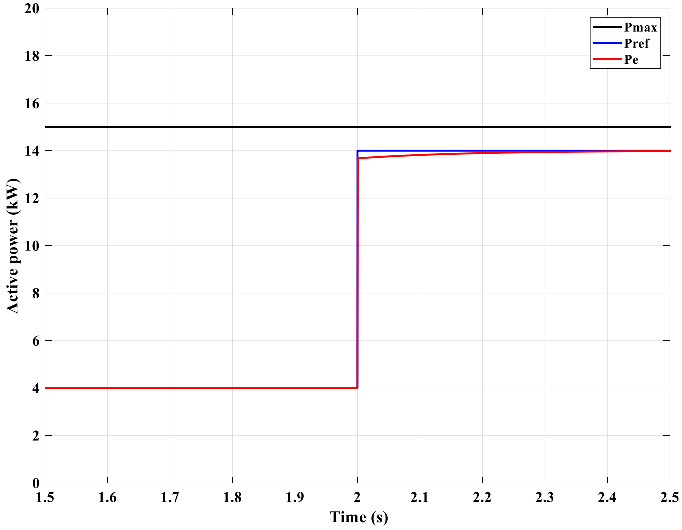

Fig. 3.15: Maximum transferable (P_{max}), reference (P_{ref}), and output active power (P_e) of the grid-connected VSC with a step change in the active power reference at t = 2 s from 4 kW to 14 kW [C4].

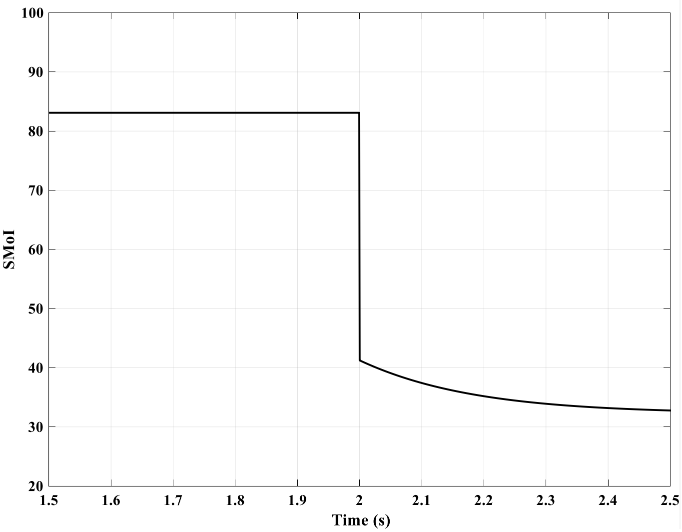

Fig. 3.16: The Semi-Moment of Inertia (SMoI) of the grid-connected VSC with a step change in active power reference at t = 2 s from 4 kW to 14 kW [C4].

Case study 2: Impact of the weak grid on the system stability and its relation to the *SMoI* index

Here, the impact of the grid impedance on the system stability and its relation with the *SMoI* index is studied. To do so, the grid impedance is doubled at $t = 2\ s$, which leads to a decrease in maximum transferrable active power, as shown in Fig. 3.17. Like in Case study 1, the SMoI decreases as the operating point gets closer to the stability boundary, as shown in Fig. 3.18.

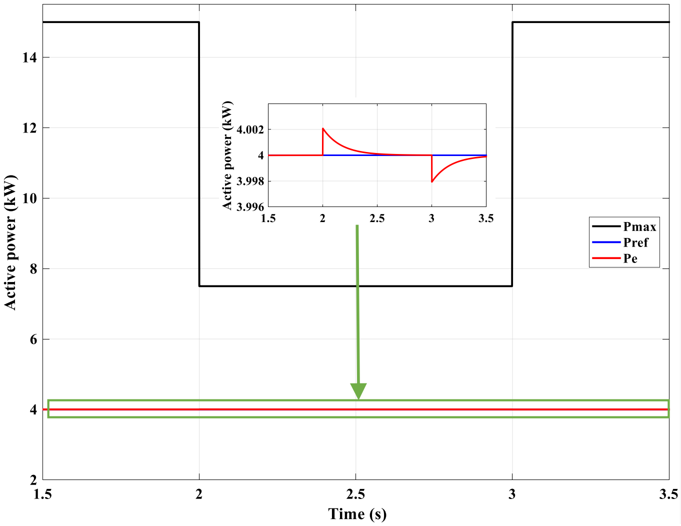

Fig. 3.17: Maximum transferable (P_{max}), reference (P_{ref}), and output active power (P_e) of the grid-connected VSC with a step change in Z_g (making Z_g twice of its initial value) at t = 2 s and 3 s [C4].

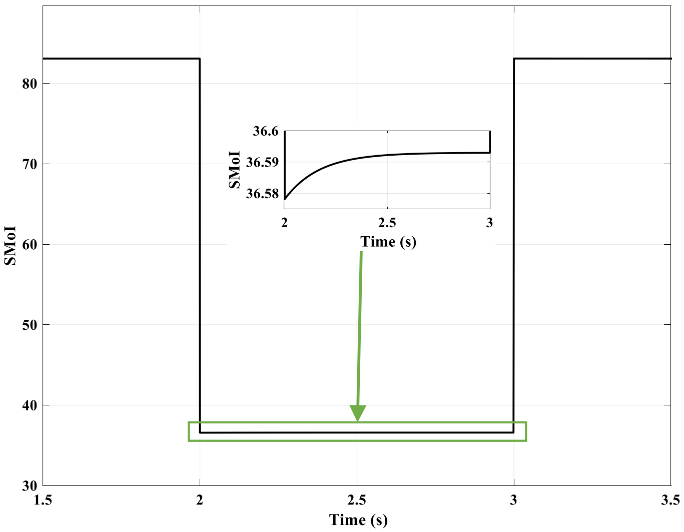

Fig. 3.18: The Semi-Moment of Inertia (*SMoI*) index of the grid-connected VSC with a step change in Z_g (making Z_g twice of its initial value) at t = 2 s and 3 s [C4].

Case study 3: analyzing the stability marginal point by using the *SMoI* index

The marginal point of stability is when the *SMoI* index becomes zero. In this circumstance, the system introduces a negative semi-inertial response, which is physically unstable condition. To demonstrate this scenario, grid impedance is changes into a large value (eight times of the base value). Then, when the active power reference is larger than the maximum transferrable power, the system will become unstable. The active power reference, the output active power, and the maximum active power are shown in Fig. 3.19. The *SMoI* index is also shown in Fig. 3.20, where it can be seen that the index becomes negative for the period that the system works in its unstable mode.

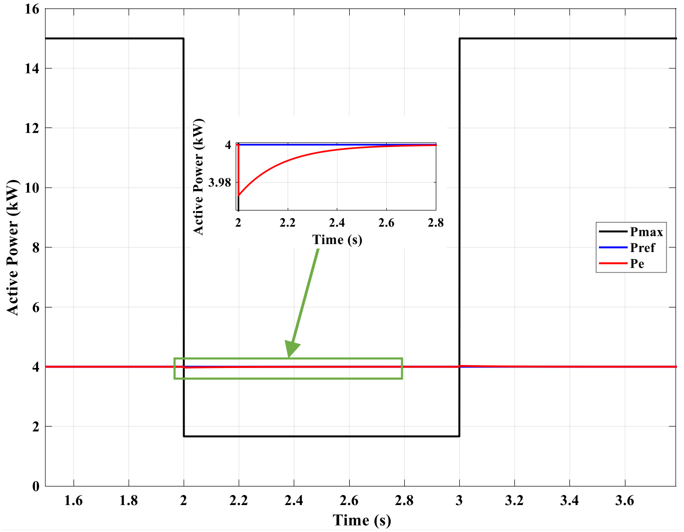

Fig. 3.19: Maximum transferable (P_{max}), reference (P_{ref}), and output active power (P_e) of the grid-connected VSC with a large step change (eight times) in Z_g at t = 2 s and 3 s [C4].

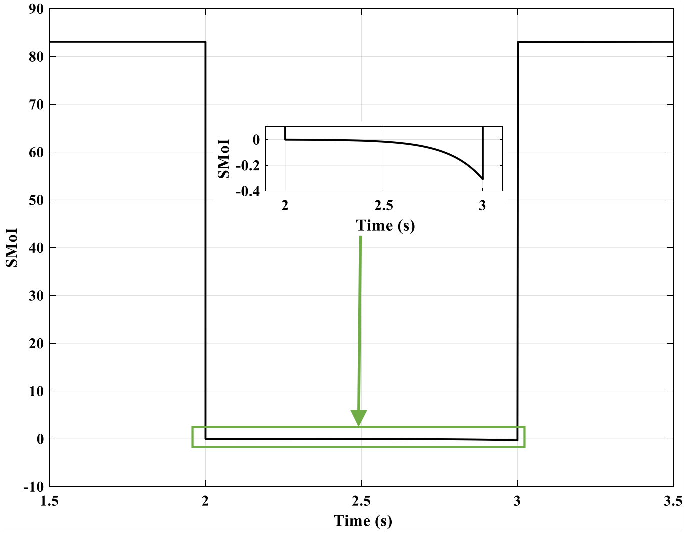

Fig. 3.20: The Semi-Moment of Inertia (*SMoI*) index of the grid-connected VSC with a with a large step change (eight times) in Z_g at t = 2 s and 3 s [C4].

It should be mentioned that the mathematical model is presented in Fig. 3.19 and Fig. 3.20. The time-domain simulation results of this scenario derived in Matlab/Simulink is presented in **Fig. 3.21**, where the instability can be seen from the VSC three-phase current.

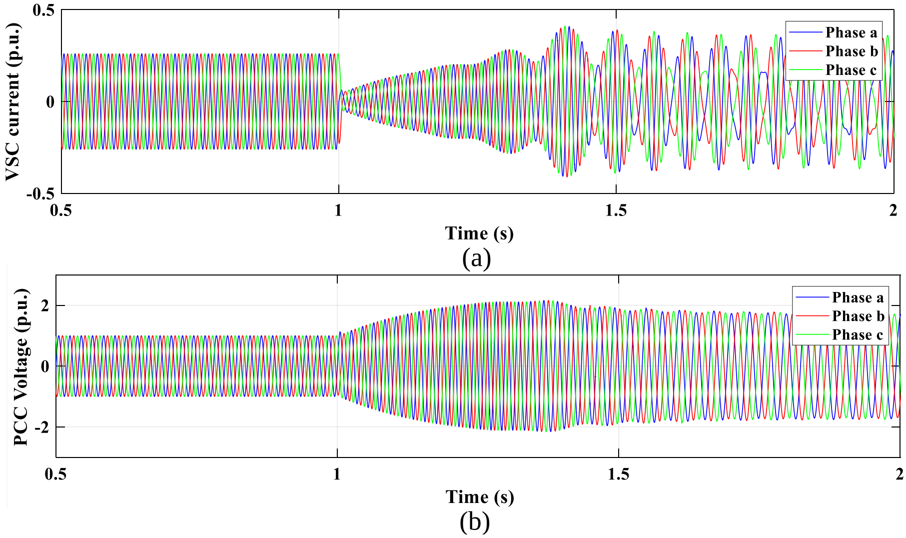

Fig. 3.21: Time-domain simulation for the unstable case study (Case study 3). (a)VSC three-phase output current and (b) the PCC three-phase voltage.

In conclusion of this part, it is shown that the grid-feeding power converter introduce a semi-inertial response to the system fluctuations, which can be determined by *SMoI* index. This inertial response is provided by the lag between the reference and actual active power of the VSC, due to the integral gain included in the active power control loop.

3.5. Transient stability of power-electronic-based power systems

In order to do transient stability analysis of large-scale PE-based power systems, the Lyapunov function theory and the equal area criterion can be used [59]. In this way, the same concept developed for the grid-tied synchronous generator can be extended to analyze the large-scale PE-based power system stability. Considering a grid-tied synchronous generator as shown in Fig. 3.22.

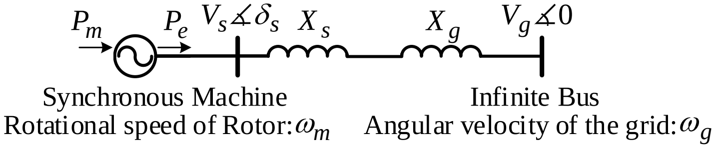

Fig. 3.22: A single-line diagram of the synchronous machine with impedance X_s connected to the grid through a line with impedance X_g.

The active power transferred to the grid is given as:

$$P_e = \frac{V_s V_g}{X_g + X_s}\sin\delta_s \tag{3.8}$$

where P_e is the transferred active power. Based on that, the swing equation can be derived as follows:

$$P_m - P_e = \omega_m J\frac{d\omega_m}{dt} \tag{3.9}$$

where P_m is the mechanical power. ω_m and J are the rotational speed and moment of inertia, respectively. By using the concept of equal area criterion, the transient stability of the grid-tied synchronous machine can be explained [22]. The inertia constant H [s] is furthermore defined as:

$$H = \frac{E_r}{S_B} = \frac{J{\omega_{m0}}^2}{2S_B} \tag{3.10}$$

Here, E_r is the rotational energy in the machine [J], ω_{m0} is the nominal rotational speed of the machine [rad/s], and S_B is the [MVA] rating of the machine. Based on (3.8), (3.9), and (3.10), the voltage angle between V_s and V_g can be determined as follows:

$$\frac{d^2\delta_s}{dt^2} = \frac{\omega_{e0}\left(P_m - P_e\right)}{2S_B H} \tag{3.11}$$

where ω_{e0} is the steady state value of the SG's voltage angle velocity. In this way, by integrating (3.11) twice, δ_s can be determined at the critical clearing time[4] as follows:

$$\delta_s\left(t\right)\Big|_{t=t_{cr}} = \frac{\omega_{e0}\left(P_m - P_e\right)t^2}{4S_B H} + \delta_0 \tag{3.12}$$

---

[4] The critical clearing time is the largest duration for the fault that the system remain stable after clearing the fault [110].

where δ_0 is the synchronous generator's voltage angle before the fault. Based on (3.12), the critical clearing time can be calculated as follows:

$$t_{cr} = \sqrt{\frac{4S_B H\left(\delta_{cr} - \delta_0\right)}{\omega_{e0}\left(P_m - P_e\right)}}. \tag{3.13}$$

For the aggregation of multiple synchronous machines, the model can be developed as follows:

$$H_A = \frac{J\omega_{m1}{}^2 + J\omega_{m2}{}^2 + \ldots J\omega_{mN}{}^2}{2\left(S_{B1} + S_{B2} + \ldots S_{BN}\right)} = \frac{E_{rA}}{S_{BA}} \tag{3.14}$$

In transient stability analysis, the marginal stability is determined by the critical clearing time of the fault. The critical clearing time can be determined as follows:

$$t_{cr} = \sqrt{\frac{4S_B H_A\left(\delta_{cr} - \delta_0\right)}{\omega_{e0}\left(P_m - P_e\right)}} \tag{3.15}$$

where $\delta_{cr} = \frac{\omega_{e0}\left(P_m - P_e\right)t^2}{4S_B H} + \delta_0$. To expand the theory to two grid areas A and B connected via a long transmission line, the following equation can be assumed for each of them:

$$\frac{d^2\delta_{eA}}{dt^2} = \frac{\omega_{e0}\left(P_{mA} - P_{eA}\right)}{2S_A H_A} = \frac{\omega_{e0}\left(P_{mA} - P_{eA}\right)}{2E_A} \tag{3.16}$$

$$\frac{d^2\delta_{eB}}{dt^2} = \frac{\omega_{e0}\left(P_{mB} - P_{eB}\right)}{2S_B H_B} = \frac{\omega_{e0}\left(P_{mB} - P_{eB}\right)}{2E_B} \tag{3.17}$$

where E_A and E_B are the total rotational energy for each area. Considering the voltage phase angle difference between two areas as $\delta_{eAB}= \delta_{eA}-\delta_{eB}$, the following equation can be derived:

$$\frac{d^2\delta_{eAB}}{dt^2} = \frac{\omega_{e0}\left(P_{mA} - P_{eA}\right)}{2E_A} - \frac{\omega_{e0}\left(P_{mB} - P_{eB}\right)}{2E_B} = \frac{\omega_{e0}\left(E_B\left(P_{mA} - P_{eA}\right) - E_A\left(P_{mB} - P_{eB}\right)\right)}{2E_A E_B}.$$

(3.18)

In steady-state, $P_{mA0}=P_{eA0}=-P_{mB0}=-P_{eB0}$. During a fault due to the interruption in a transmission line, a surplus of power is created in area A and a deficit of power in area B. $P_{eA} = P_{mA0} - \Delta P$, $P_{eB} = P_{mB0} + \Delta P$. Then,

$$\frac{d^2\delta_{eAB}}{dt^2} = \frac{\omega_{e0}\left(E_B\Delta P - E_A\left(-\Delta P\right)\right)}{2E_AE_B} = \frac{\omega_{e0}\Delta P\left(E_B + E_A\right)}{2E_AE_B}. \tag{3.19}$$

Defining,

$$H_{eq} = \frac{E_AE_B / S_{base}}{E_B + E_A} \tag{3.20}$$

yields

$$\frac{d^2\delta_{eAB}}{dt^2} = \frac{\omega_{e0}\Delta P}{2H_{eq}S_{base}}. \tag{3.21}$$

Integrating twice up to the critical clearing angle as discussed in (3.12):

$$\delta(t)\Big|_{t=t_{cr}} = \frac{\omega_{e0}\Delta P {t_{cr}}^2}{4S_{base}H_{eq}} + \delta_0. \tag{3.22}$$

Based on (3.22), the critical clearing time for the two-area system can thus be derived as

$$t_{cr} = \sqrt{\frac{4S_{base}H_{eq}\left(\delta_{cc} - \delta_0\right)}{\omega_{e0}\Delta P}}. \tag{3.23}$$

Note that S_{base} can be chosen with an arbitrary value. A conclusion from (3.23) is the relationship between the critical clearing time and the system inertia constant is given as follows:

$$t_{cr} = k\sqrt{H_{eq}}. \tag{3.24}$$

Another simpler form of this equation is

$$t_{cr} = \sqrt{\frac{4E_{eq}\left(\delta_{cc} - \delta_0\right)}{\omega_{e0}\Delta P}} \tag{3.25}$$

in which the equivalent rotational energy is defined as:

$$E_{eq} = \frac{E_AE_B}{E_B + E_A}. \tag{3.26}$$

An important conclusion from (3.20) and (3.26) is that if the inertia in one of the areas is low, then the equivalent inertia will be low consequently. This means that if E_A is much larger than E_B, then $E_{eq} = E_B$. In practice, if the NSG penetration is not distributed normally in the system, then a region with a high penetration of NSG determines the whole system inertial response.

3.5.1. Simulation results

In this part, two case studies on the Kundur two-area test system [59] and the Nordic 23-machine test system [107] are presented to verify the theory discussed in Section 3.5.

3.5.1.1 Testbed 1: Kundur two-area test system

The Kundur two-area test system is shown in Fig. 3.23 [59]. Some basic information regarding this test system can be found in Table 3.4, in which N is the abbreviation of Node, e.g. N5 indicates Node 5. The generators are equipped with automatic voltage regulators (AVR), power system stabilizers (PSS), and SGs 1 and 3 are also equipped with turbine governors.

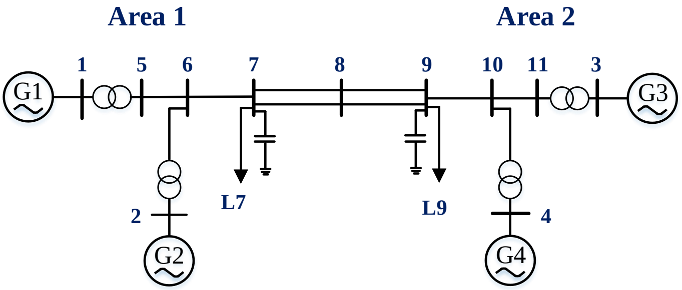

Fig. 3.23: Kundur two-area test system [59].

Table 3.4: Kundur two-area test system information.

Line length N5-N6	25 km
Line length N6-N7	10 km
Line length N9-N10	10 km
Line length N10-N11	25 km
Line length N7-N9	220 km
L7 (including shunt compensation)	P=967 MW, Q=-100 MVA
L7 (including shunt compensation)	P=1767 MW, Q=-250 MVA
G1	Sb=900 MVA, P=700 MW, Q=175 MVA, Uset=1.03 p.u.
G2	Sb=900 MVA, P=700 MW, Q=235 MVA, Uset=1.01 p.u.

G3 (slack bus)	Sb=900 MVA, P=720 MW, Q=160 MVA, Uset=1.02 p.u.
G4	Sb=900 MVA, P=700 MW, Q=202 MVA, Uset=1.01 p.u.
P7-9	400 MW (200 MW per line)

To evaluate the inertia-based stability assessment method discussed in Section 3.5, which is determining the critical clearing time of a fault in the system, two case studies are developed in the Kundur test system in DigSILENT PowerFactory software: Case study 1, in which the NSG penetration is only increased in Area 1 in Fig. 3.23, and Case study 2, in which the NSG penetration is increased equally in both areas. The results of the critical clearing time based on the equivalent inertia is presented in Fig. 3.24. A fault in node 7 is used for both case studies. In Fig. 3.24(a), the increase of the penetration only in Area 1 is considered, whereby increasing the NSG penetration, the equivalent inertia decreases as well as the critical clearing time. The actual critical clearing time in Fig. 3.24 is obtained by repeating the simulation and increasing the clearing time of the fault until the system becomes unstable. Almost the same behavior can be seen for the increase of NSG penetration in both areas normally, as shown in Fig. 3.24(b). The theory developed in Section 3.5 is compared with the simulation results as shown in Fig. 3.24(d).

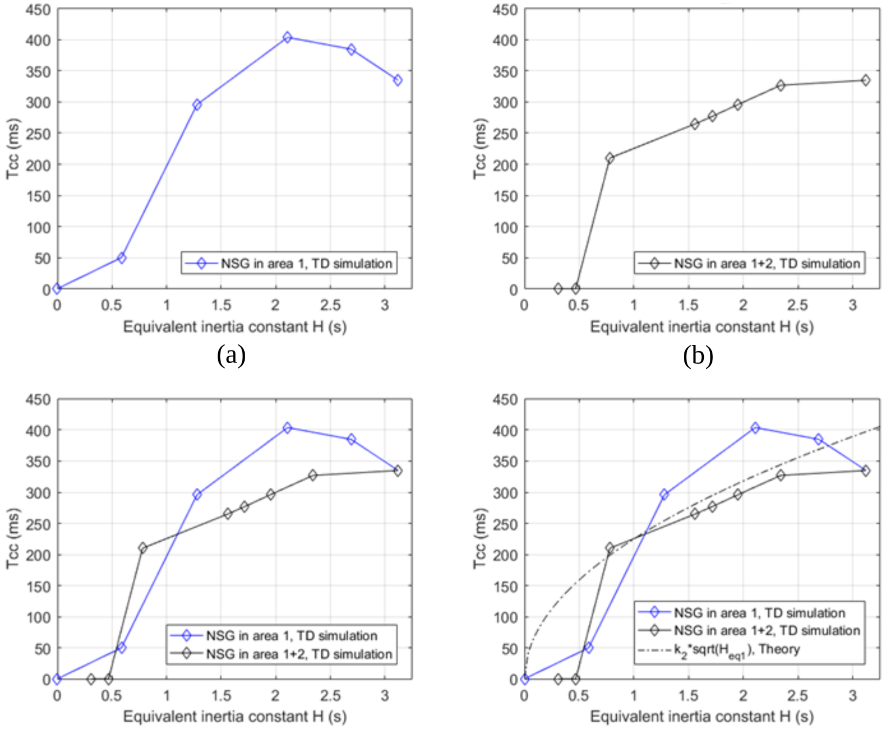

(a) (b)

(c) (d)

Fig. 3.24: Critical clearing time results for a fault in node 7. (a) increasing the NSG penetration only in Area 1, (b) increasing the NSG penetration in both areas, (c) comparing the uniformed distribution of NSG penetration vs. the non-uniformed distribution of NSG penetration, and (d) estimation of the critical clearing time based on the proposed method.

As it can be seen from Fig. 3.24(d), the proposed method is confirmed by the simulation results. However, it should be mentioned that there are some other nonlinear terms beyond the swing equation of synchronous machines, such as the dynamic response of the loads, which affect the results and cause the mismatch between the proposed method and the time-domain simulation results.

3.5.1.2 Testbed 2: Nordic 23-machine test system

The Nordic 23-machine test system is developed on DigSILENT PowerFactory for the time-domain stability assessment of large-scale power systems, which is shown in Fig. 3.25 [107].

Some details regarding the Nordic 23-machine test system are presented in Table 3.5 and Table 3.6. AVR's are modeled as SEXS (Simplified Excitation System IEEE acc. To PowerFactory library). AVR compensating system (droop) is set to Xc= 0.05 p.u. at all units. Hydro-Governors are positioned in North & External areas; the Governors in External have slightly different droop settings.

Table 3.5: Detailed information of Nordic 23-machine test system's synchronous generators.

		Synchronous Generator				**AVR - SEXS**				**Hydro - Governor**		
Name	**Area**	**S_{gn}**	**P_{gini}**	**H**	**U_{set}**	**Tb**	**Ta**	**K**	**Te**	**Tr**	**Tw**	**Tg**
		MVA	**MW**	**s**	**pu**	**s**	**s**	**pu**	**s**	**s**	**s**	**s**
sym_1012_1	North	800	400	3	1.13	20	4	50	0.1	5	1	0.2
sym_1013_1		600	300	3	1.15	20	4	50	0.1	5	1	0.2
sym_1014_1		700	550	3	1.16	20	4	50	0.1	5	1	0.2
sym_1021_1		600	400	3	1.10	20	4	50	0.1	5	1	0.2
sym_1022_1		250	200	3	1.07	20	4	50	0.1	5	1	0.2
sym_2032_1		850	750	3	1.10	20	4	50	0.1	5	1	0.2
sym_4011_1		1000	633	3	1.01	20	4	50	0.1	5	1	0.2
sym_4012_1		800	500	3	1.01	20	4	50	0.1	5	1	0.2
sym_4021_1		300	250	3	1.00	20	4	50	0.1	5	1	0.2
sym_4031_1		350	310	3	1.01	20	4	50	0.1	5	1	0.2
sym_1042_1	Central	400	360	6	1.00	50	5	120	0.1	No Governor modelled		
sym_1043_1		200	180	6	1.00	50	5	120	0.1			
sym_4041_1		300	0	2	1.00	20	4	50	0.1			
sym_4042_1		700	630	6	1.00	50	5	120	0.1			
sym_4047_1		600	540	6	1.02	50	5	120	0.1			
sym_4047_2		600	540	6	1.02	50	5	120	0.1			
sym_4051_1		700	600	6	1.02	50	5	120	0.1			
sym_4051_2		700	400	6	1.02	50	5	120	0.1			
sym_4062_1	South	600	530	6	1.00	50	5	120	0.1			
sym_4063_1		600	530	6	1.00	50	5	120	0.1			
sym_4063_2		600	530	6	1.00	50	5	120	0.1			
sym_4071_1	Ext	500	300	3	1.01	20	4	50	0.1	5	1	0.2
sym_4072_1		4500	2000	3	1.01	20	4	50	0.1	5	1	0.2

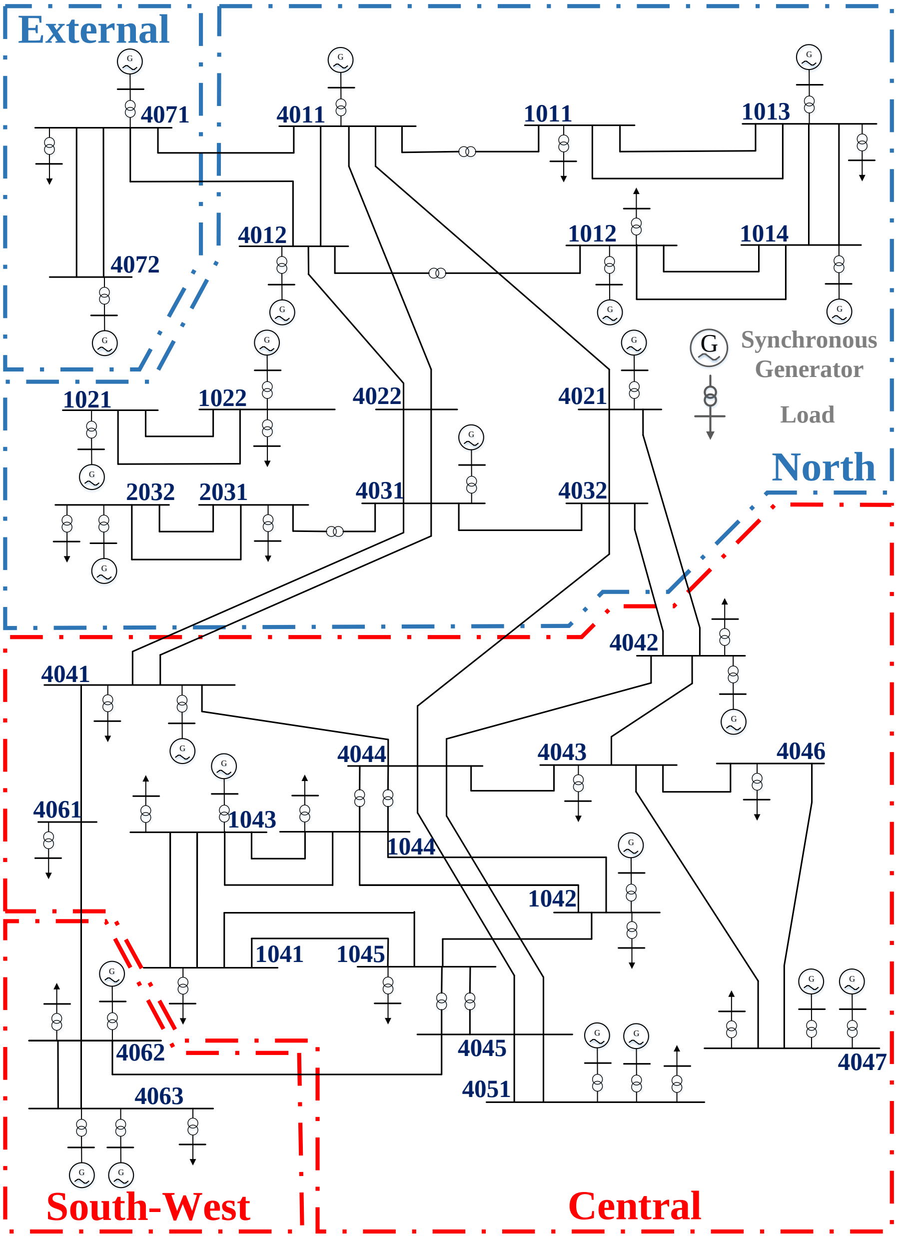

Fig. 3.25: Nordic 23-machine test system to be used for transient stability analysis [107]**.**

Table 3.6 shows line parameters of North-Central interconnection lines.

Table 3.6: Line characteristics of the North-Central interconnecting lines.

Lines		R1 Ohm	X1 Ohm
lne_4031_4041_1	Line 1	9.6	64
lne_4031_4041_2		9.6	64
lne_4021_4042_1	Line 2	16	96
lne_4032_4042_1	Line 3	16	64
lne_4032_4044_1		9.6	80

The simulation results for a three-phase fault for 40% NSG penetration (NSG distributed over all areas) are shown in Fig. 3.26.

Based on the theory derived in Section 3.5, the equivalent inertia of a two-area system can be expressed as $H_{eq} = \frac{E_{A1}E_{A2}/S_{Btot}}{E_{A1}+E_{A2}}$, where E_{A1} and E_{A2} are rotating energy in areas A1 and A2, where A1 indicated External and North regions and A2 indicated South-West and Central regions. S_{Btot} is the base rating of the system (may be arbitrarily chosen, e. g. the total installed base of SGs in the grid).

This expression can be applied in the prevailing grid structure. In consideration of the given network, an area split is most likely to happen between Northern- and Southern areas, due to the long lines interconnecting them. The rotating energies in these areas are equivalent to the sum of the inertia times the rating of the machines $E_{A1} = \sum H_{Gen} \cdot S_{Gen}$ in North and External grid, and $E_{A2} = \sum H_{Gen} \cdot S_{Gen}$ in the Center and South-West. H_{Gen} is the machine inertia constant and S_{Gen} is the machine rating power.

The equivalent inertia variable will also be dependent on the fault location, assuming the grid is split at the fault. It is especially useful when grid areas are clearly separated by long transmission lines.

As an example calculation for the area External at 100% SG:

Sym_4071_1, S_{G_4071}=500 MVA, H_{4071}= 3 s

Sym_4072_1, S_{G_4072}=4500 MVA, H_{4072}= 3 s

$E_{Ext} = S_{G_{4071}} \cdot H_{4071} + S_{G_{4072}} \cdot H_{4072} = 15\ GWs$

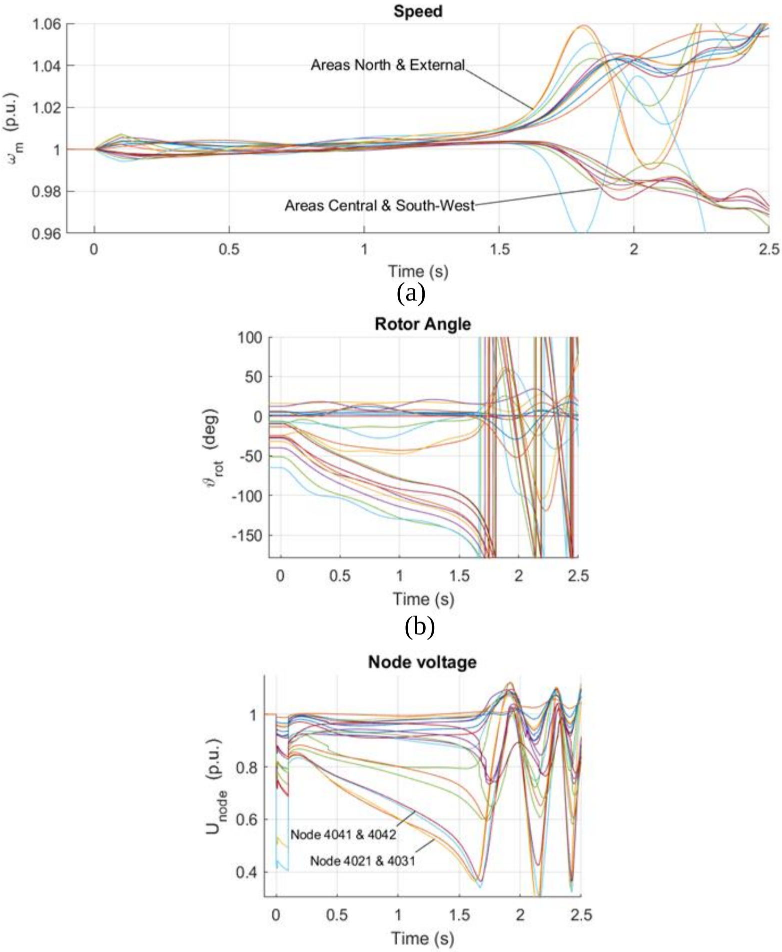

(a)

(b)

(c)

Fig. 3.26: Grid with 40% NSG, distributed in all areas (a) synchronous generators' rotor speed, (b) synchronous generators' rotor angle, and (c) bus voltages. Fault on line between bus 4031 and bus 4041; t_{clear} = 100ms.

The rotating energies of the other grid areas are:

$$E_{North} = 18.75\ GWs,\ E_{Central} = 24\ GWs,\ E_{South-W} = 10.8\ GWs$$

S_{Btot}, which is an arbitrary parameter, is selected to $S_{Btot} = 10\ GW$.

Therefore, the equivalent inertia constant of the grid with 100% SG considering faults on the long lines interconnecting North and Central is

$$H_{eq_{100\%SG}} = \frac{(15+18{,}75)\cdot(24+10{,}8)/10}{15+18{,}75+24+10{,}8} = 1.71\ s$$

The equivalent inertia of the grid is depending on the NSG distribution pattern chosen as shown in **Fig. 3.27**. As the rating of the machines in each area decreases, so does the rotating energy and consequently also the equivalent inertia.

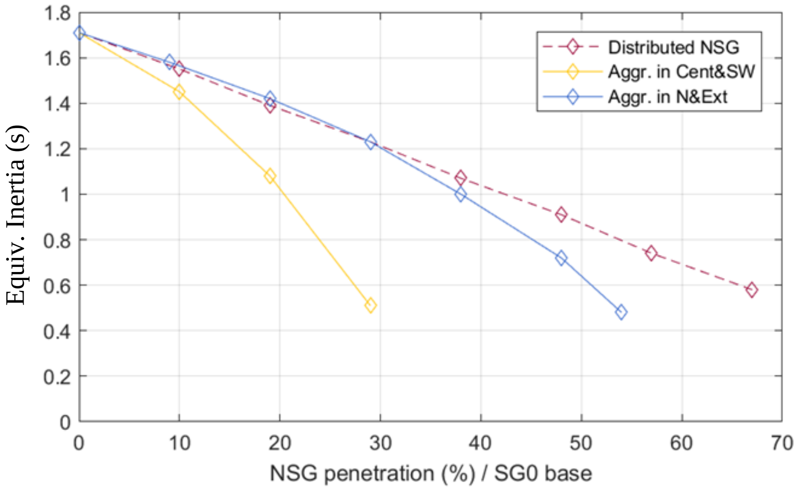

Fig. 3.27: Equivalent inertia of grid at distributed/aggregated NSG case(s).

In contrast, a more straight forward approach is to sum up the rotating energy of the whole grid $H_{tot} = \frac{\sum H_{Gen}\cdot S_{Gen}}{S_{Btot}}$.

The total inertia H_{tot} of the grid in the same cases is plotted in Fig. 3.28.

The critical clearing time characteristics for faults on Line 1 and Line 2 vs NSG penetration are plotted in Fig. 3.29.

It can be observed that the equivalent inertia (Fig. 3.27) gives a better prediction for the critical clearing time than the values of the total inertia (Fig. 3.28).

With an increase of NSG aggregated in Central & Southwest, there is a sudden drop in both the equivalent inertia and the critical clearing time characteristics. However, during aggregation in North & External (blue), the eq. inertia stays slightly above the values of the distributed case (dashed) until about 30% penetration. Similarly, the critical clearing time trend in Fig. 3.29 shows higher values for the aggregation in North & External (blue) until a sudden drop occurs, here between 40 and 50% NSG, which cannot be explained by the inertia-based theory developed here. This is because there are other nonlinear terms in the system, such as loads dynamic response, that affect the transient stability.

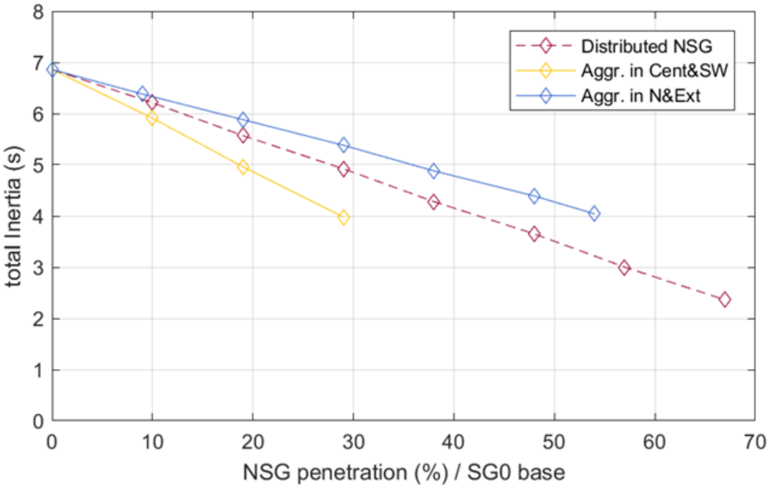

Fig. 3.28: Total inertia of grid at distributed/aggregated NSG case(s).

The first order approximate relation between critical clearing time and H_{eq} was given in (3.23) as $T_{cc} = \sqrt{\frac{4S_{Btot}H_{eq}(\delta_{cc}-\delta_0)}{\omega_0 \Delta P}}$. This can be simplified and written as $T_{cc} \approx k \cdot \sqrt{H_{eq}}$. The critical clearing time found from the simulation study for the faults at Line 1 (line between bus 4031 and bus 4041) and Line 2 (line between bus 4021 and bus 4042) are plotted in **Fig. 3.30** and **Fig. 3.31**. where, the theoretical prediction is also outlined. It is worth mentioning that the system cannot be run in a very low inertia mode (0.5s for the equivalent inertia as shown in **Fig. 3.30** and **Fig. 3.31**).

There are rather large differences between the basic theory and the simulation results. This is to be expected since a large number of factors influence the critical clearing time and the basic theory only accounts for a few of them. Both the theory and the simulation results show a monotonous increase in the critical clearing time with increasing H_{eq}. However, while the theory predicts that the critical clearing time should be zero when the H_{eq} is zero, the simulation results show that zero critical clearing time is reached for values well higher than zero inertia. This is counter-intuitive and suggests that other not accounted factors such as the geographical size and form of the grid areas and the voltage control performance of the NSG and SG units may affect the critical clearing time strongly [108].

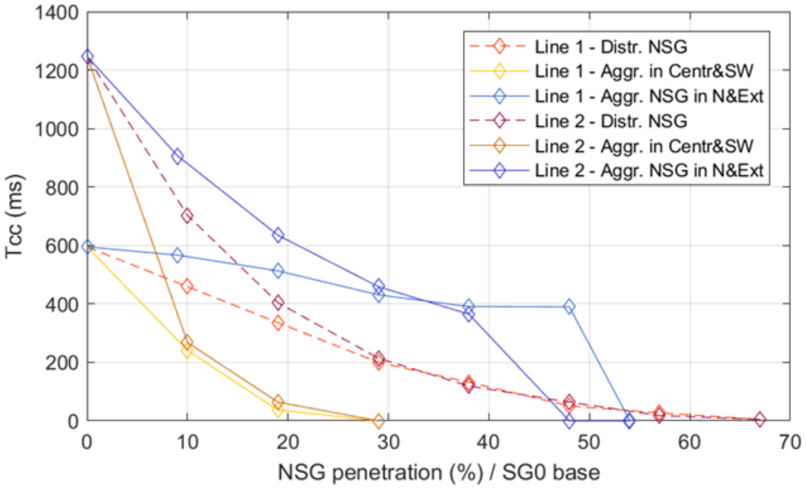

Fig. 3.29: Line 1 (line between bus 4031 and bus 4041) and Line 2 (line between bus 4021 and bus 4042) clearing times at increasing NSG penetration.

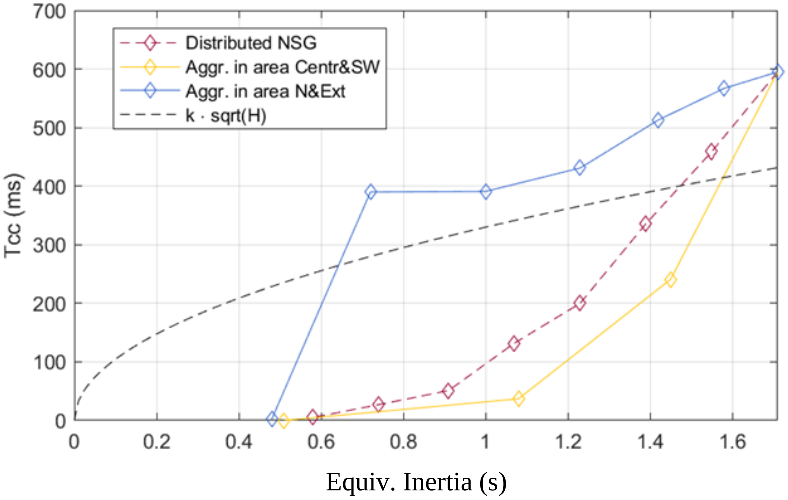

Fig. 3.30: Line 1 (line between bus 4031 and bus 4041) actual critical clearing time and prediction vs. equivalent Inertia.

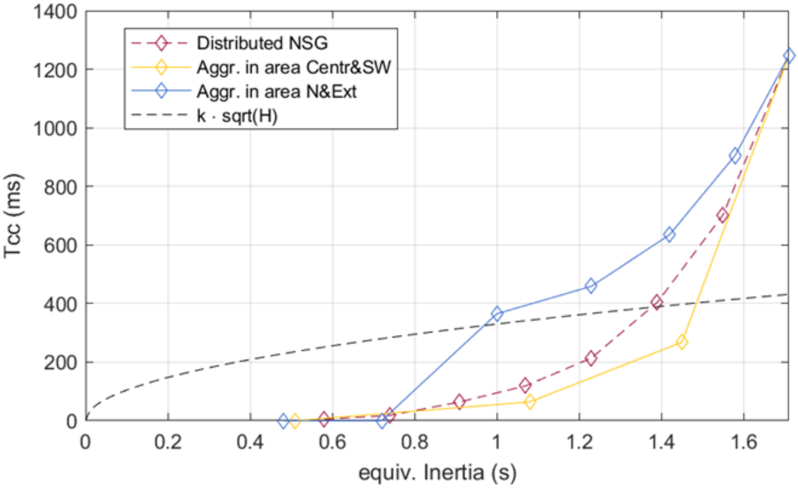

Fig. 3.31: Line 2 (line between bus 4021 and bus 4042) actual critical clearing time and predictor vs. equivalent Inertia

3.6. Summary

In this chapter, the large-signal stability of large-scale PE-based power systems is studied. To do so, first, different stability challenges introduced by the increase in PE-based unit's penetration are discussed. Then, an inertial-based method is proposed to assess the transient stability of systems with a high penetration of NSGs. The proposed method is tested on the Kundur two-area and Nordic32 standard test systems.

In addition, a discussion on the grid-tied VSC inertial response is presented, where it is shown that a grid-feeding VSC introduces a semi-inertial response to a fluctuation; however, its response is different to the well-known synchronous generator's inertial response. Therefore, by increasing the PE-based unit's penetration in power systems, it is expected to have lower equivalent and this is also discussed in this chapter.

Related Publications

J3. **B. Shakerighadi**, S. Peyghami, E. Ebrahimzadeh, M. G. Taul, F. Blaabjerg and C. L. Bak, " A New Guideline for Security Assessment of Power Systems with a High Penetration of Wind Turbines," in Appl. Sci., 10, 3190, pp. 1-16, 2020.

Main contribution:

In this paper, the work in presented in [C3] is extended in more details. The importance of the PE-based units' stability on the PE-based power system security is emphasized and studied in details. Different PE-based related stability issues of some modern power systems are reviewed and their stability issues are discussed in details.

C3. **B. Shakerighadi**, S. Peyghami, E. Ebrahimzadeh, F. Blaabjerg and C. L. Bak, "Security Analysis of Power Electronic-based Power Systems," IECON 2019 - 45th Annual Conference of the IEEE Industrial Electronics Society, Lisbon, Portugal, 2019, pp. 4933-4937.

Main contribution:

In this paper, a new guideline for the PE-based power systems security assessment is introduced. A wrong frequency estimation by the PLL during the three-phase fault is discussed. In addition, different security challenges of the modern power system, which cannot fully be covered by the conventional security assessment of power system, is introduced and discussed.

C4. **B. Shakerighadi**, E. Ebrahimzadeh, F. Blaabjerg and C. L. Bak, "Large Signal Stability Assessment of the Grid-Connected Converters based on its Inertia," 2019 21st European Conference on Power Electronics and Applications (EPE '19 ECCE Europe), Genova, Italy, 2019, pp. 1-7.

Main contribution:

In this paper, a nonlinear model of the grid-connected VSC based on its dynamic inertia is presented. In order to assess the large-signal stability of the system, the dynamic model of the equivalent synchronous machine (ESM) is monitored, and then based on the inertia of the ESM, the stability margin of the system is determined.

Chapter 4.
Conclusion

Based on the obtained results in the previous chapters, a summary of the Ph.D. project is presented in this chapter. Also, the main contributions of this work are discussed, as well as some new research directions are outlined for future work.

4.1. Summary

To understand the true stability behavior of PE-based power systems subjected to a large disturbance, a large-signal model of the system should be used for analysis. As modern power systems are nonlinear by their nature, they represents a nonlinear behavior when they are subjected to a large disturbance. Therefore, a large-signal model of the PE-based power system, following by a large-signal stability assessment, will give a clear understanding of the grid stability.

In this work, the large-signal stability of PE-based power system is assessed. To do so, non-linear techniques are used to analyze the non-linear model of the system, which are mostly based on the concept of the Lyapunov function. However, other techniques, such as the equal area criterion and phase portrait stability criterion, are also used to assess the nonlinear models, which represent the behavior of the PE-based power systems. The analysis starts with a simple model of the PE-based power system, which is a grid-tied VSC, and it continues and expands to larger systems, more specifically the Nordic 23-machine and IEEE 39 bus test systems. It should be noticed that the analysis for the smaller systems, like the grid-tied VSC, include details about the control systems, while for large-scale power systems, the behavior of the whole system is prioritized compared to the behavior of each component in order to do the stability analysis. In such case, a reduced model of large-scale grids is of importance.

The Thesis starts with an introduction of the power systems stability and its analysis in Chapter 1. Different grid-tied VSC types, such as the grid-feeding power converters, the grid-forming power converters, the grid-supporting voltage source converters, and the grid-supporting current source converters are discussed. Besides, the importance of the increase of NSGs in power systems and their impact on the systems stability are reviewed. Then, different analysis approaches in this PhD work are highlighted.

In Chapter 2, the stability of grid-tied VSC is discussed. First, the stabilities of different VSC components are treated. This includes the large-signal stability assessment of the current control loop, the active power control loop, the delay impact caused by the PWM switching, and the PLL large signal stability dynamics. A second-order Lyapunov function is used to assess the large-signal stability of the grid-tied VSC with its simplest model, which includes only the current controller. In this way, as the system is assumed linear, the large-signal stability assessment leads to the same result of the analysis with linear stability techniques. Also, in this chapter, a parametric Lyapunov function is developed to demonstrate the large-signal stability assessment of the grid-tied VSC and thereby, the stability of the single VSC connected to the grid can be assessed.

In Chapter 3, the main goal has been to assess the large-signal stability and security of more large-scale modern power systems. In this part, first, a new guideline for the security assessment of PE-based power systems is outlined. Then, a new method to assess the transient stability of large-scale power systems is proposed. In this chapter, the impact of increasing the penetration of PE-based energy sources on the grid stability is assessed. To do so, the main challenge is to model the system (or a part of the system) in its simplest form so that it represents its nonlinear behavior. The equivalent moment of inertia is the key in order to model the system behavior.

Finally, in Chapter 4, as it is presented here, the conclusion and future trends of the work are discussed.

4.2. Thesis contributions

In this work, the large-signal stability analysis of modern power systems with power electronic converters has been the main goal. The main contributions of this PhD thesis are listed as follows:

- ✓ Proposing a systematic use of a Lyapunov function for the grid-tied VSC.

A systematic Lyapunov function is proposed for the large-signal stability assessment of the grid-tied VSC. In the proposed method, a step-by-step guideline to find an appropriate second-order Lyapunov function is presented, so the method can be expanded to other nonlinear systems for doing large-signal stability assessment.

- ✓ Proposing a non-linear model for the PLL and analyzing its non-linear behavior.

The PLL is a nonlinear feedback control that is used to estimate the phase angle of its input signal e.g. the grid voltage at PCC. Although the PLL's behavior can be modeled by a linear equivalent model, the linear model of the PLL does not present the precise behavior of it when it is subjected to a large disturbance. For this reason, a large-signal stability assessment method for the PLL based on its nonlinear model is proposed.

- ✓ Proposing a new guideline and method for the security assessment of the PE-based power systems.

By increasing the penetration of PE-based energy sources, such as wind turbines and photovoltaics, the security assessment of modern power grids needs a revision. Different stability challenges caused by the PE-based units should be included in the security assessment. A new guideline for the security assessment of the PE-based power systems is proposed to cover all challenges introduced by the PE-based units and also from a power system stability point of view.

- ✓ Proposing a new method to assess the large-signal stability of large-scale power systems.

To assess the stability of large-scale power systems, one should consider the system-level stability criteria. The transient stability of large-scale power systems is related to different stability concepts, such as voltage stability, rotor angle stability, and frequency stability. In this work, an equivalent inertia-based method is proposed to represent the system (or a part of the system) behavior regarding large disturbances, such as a three-phase fault in the power grid.

4.3. Future Works

Some future trends and continuation of this works are listed as follows:

- Large-signal stability assessment of power system based on 100% NSG.

  As the number of PE-based units is increasing in power systems, at some point, the power system will become more PE-based oriented than the conventional ones. This brings new challenges, as these electrical grids run with very low inertia. Considering a power system that runs based on 100% NSG penetration, different challenges appear, such as the definition of a reference machine for the system synchronization, need to be introduced. A grid with 100% NSG penetration is already mentioned in the literature and is an ongoing challenge of nowadays modern grids, and how to operate such system is not clear [53], [109].

- Study the impact of offshore wind farms on the systems’ large-signal stability.

  Offshore wind farms are becoming the energy production of many power systems. Therefore, its impact on the power system stability is becoming an important issue. There is not much done regarding the modeling and stability assessment of offshore wind farms in the literature, especially seem from a large-signal perspective, which can be applied to large-scale power system analysis.

- Studying the impact of the protection system on the large-signal stability of the grid.

Conventional protection systems are well-designed for conventional power systems. For the modern distributed energy power systems, there has been a lot of efforts to design appropriate protection systems. However, their impact on the large-signal stability of the system is not well-studied. As the protection system behavior can change the grid topology, its impact on the grid's large-signal stability is an important topic to investigate.

- Aggregation of many units to do large-signal stability analysis

Generally, different forms of the grid-tied VSCs are used in power systems. This makes the stability assessment of PE-based power systems a more challenging and time consuming issue. To analyze the large-signal stability of such a system, the aggregation of different VSC models should be considered instantly.

- Reliability assessment of integrating different power converter structures, such as grid-feeding and grid-forming power converters

Apart from the stability issues discussed in this project, the reliability of PE-based power systems that include different models and control systems of power converters is an interesting topic to investigate. Also how the mix should be between grid-forming and grid-feeding systems.

- Model validation by using hardware in the loop

It could be interesting to investigate validation methods of the models developed in this project by using hardware in the loop studies. For grid-tied VSC laboratory validation, a dSPACE and grid simulator can be used; however, for large-scale power systems, real-time digital simulator (RTDS) need to be used in order to fully map the behavior of such a complicated system.

References

[1] F. Blaabjerg, R. Teodorescu, M. Liserre, and A. V. Timbus, “Overview of control and grid synchronization for distributed power generation systems,” *IEEE Trans. Ind. Electron.*, vol. 53, no. 5. pp. 1398–1409, Oct-2006.

[2] F. Blaabjerg, Z. Chen, and S. B. Kjaer, “Power electronics as efficient interface in dispersed power generation systems,” *IEEE Trans. Power Electron.*, vol. 19, no. 5, pp. 1184–1194, 2004.

[3] X. Wang, F. Blaabjerg, and W. Wu, “Modeling and analysis of harmonic stability in an AC power-electronics- based power system,” *IEEE Trans. Power Electron.*, vol. 29, no. 12, pp. 6421–6432, 2014.

[4] M. Liserre, R. Teodorescu, and F. Blaabjerg, “Stability of photovoltaic and wind turbine grid-connected inverters for a large set of grid impedance values,” *IEEE Trans. Power Electron.*, vol. 21, no. 1, pp. 263–271, 2006.

[5] V. Telukunta, J. Pradhan, A. Agrawal, M. Singh, and S. G. Srivani, “Protection challenges under bulk penetration of renewable energy resources in power systems: A review,” *CSEE J. Power Energy Syst.*, vol. 3, no. 4, pp. 365–379, Dec. 2017.

[6] S. Peyghami, P. Pakensky, and F. Blaabjerg, “An overview on the Reliability of Modern Power Electronic Based Power Systems,” *IEEE Open J. Power Electron.*, vol. 1, no. Feb., pp. 34–50, 2020.

[7] A. Karimi *et al.*, “Inertia Response Improvement in AC Microgrids: A Fuzzy-Based Virtual Synchronous Generator Control,” *IEEE Trans. Power Electron.*, vol. 35, no. 4, pp. 4321–4331, 2020.

[8] J. Ma, Z. Song, Y. Zhang, Y. Shen, and J. S. Thorp, “Research on the Impact of DFIG Virtual Inertia Control on Power System Small-Signal Stability Considering the Phase-Locked Loop,” *IET Gener. Transm. Distrib.*, vol. 11, no. 16, pp. 4087–4095, 2017.

[9] S. Golestan, J. M. Guerrero, and J. C. Vasquez, “Three-Phase PLLs : A Review of Recent Advances,” *IEEE Trans. Power Electron.*, vol. 32, no. 3, pp. 1894–1907, 2017.

[10] Eirgrid, “DS3: Frequency Control Workstream 2015,” *EirGrid SONI*, pp. 1–7, 2015.

[11] H. Ritchie and M. Roser, “Renewable Energy,” *Our World Data*, 2020.

[12] N. Miller, D. Lew, and R. Piwko, “Technology Capabilities for Fast Frequency Response,” *GE Energy Consult.*, p. 166, 2017.

[13] National Grid, “Enhanced Frequency Control Capability (EFCC),” *Tec. Rep., Nov.*, pp. 1–67, 2015.

[14] N. Hatziargyriou *et al.*, “Stability definitions and characterization of dynamic behavior in systems with high penetration of power electronic interfaced technologies,” *Tec. Rep., IEEE Power Energ. Soc.*, pp. 1–42, 2020.

[15] D. Mondal, A. Chakrabarti, and A. Sengupta, *Power System Small Signal Stability Analysis and Control*. London: Elsevier Inc., 2014.

[16] W. Du, Q. Fu, H. F. Wang, and S. Member, “Power System Small-Signal Angular Stability Affected by Virtual Synchronous Generators,” *IEEE Trans. Power Syst.*, vol. 34, no. 4, pp. 3209–3219, 2019.

[17] S. Wang, S. Member, Z. Liu, and J. Liu, “Small-Signal Modeling and Stability Prediction of Parallel Droop-Controlled Inverters Based on Terminal Characteristics of Individual Inverters,” *IEEE Trans. Power Electron.*, vol. 35, no. 1, pp. 1045–1063, 2020.

[18] E. Ebrahimzadeh, F. Blaabjerg, X. Wang, and C. L. Bak, “Small Signal Modeling of Wind Farms,” in *2017 IEEE Energy Conversion Congress and Exposition (ECCE)*, pp. 3710–3716.

[19] P. W. M. P. Sauer, “‘Power system dynamics and stability,’ Urbana, vol. 51,” pp. 34–361, 1997.

[20] D. Yang, X. Wang, S. Member, F. Liu, K. Xin, and Y. Liu, “Symmetrical PLL for SISO Impedance Modeling and Enhanced Stability in Weak Grids,” *IEEE Trans. Power Electron.*, vol. 35, no. 2, pp. 1473–1483, 2020.

[21] X. Wang and F. Blaabjerg, “Harmonic Stability in Power Electronic-Based Power Systems: Concept, Modeling, and Analysis,” *IEEE Trans. Smart Grid*, vol. 10, no. 3, pp. 2858–2870, 2019.

[22] J. Machowski, J. W. Bialek, and J. R. Bumby, *POWER SYSTEM DYNAMICS Stability and Control*, 2nd ed. United Kingdom: John Wiley & Sons, Ltd,

2008.

[23] M. Huang, Y. Peng, C. K. Tse, Y. Liu, J. Sun, and X. Zha, “Bifurcation and Large-Signal Stability Analysis of Three-Phase Voltage Source Converter Under Grid Voltage Dips,” *IEEE Trans. Power Electron.*, vol. 32, no. 11, pp. 8868–8879, 2017.

[24] Q. Hu, L. Fu, F. Ma, and F. Ji, “Large Signal Synchronizing Instability of PLL-Based VSC Connected to Weak AC Grid,” *IEEE Trans. Power Syst.*, vol. 34, no. 4, pp. 3220–3229, 2019.

[25] A. Sajadi, R. M. Kolacinski, K. Clark, K. A. Loparo, and L. Fellow, “Transient Stability Analysis for Offshore Wind Power Plant Integration Planning Studies — Part I : Short-Term Faults,” *IEEE Trans. Ind. Appl.*, vol. 55, no. 1, pp. 182–192, 2019.

[26] A. Sajadi, R. M. Kolacinski, K. Clark, K. A. Loparo, and L. Fellow, “Transient Stability Analysis for Offshore Wind Power Plant Integration Planning Studies — Part II : Long-Term Faults,” *IEEE Trans. Ind. Appl.*, vol. 55, no. 1, pp. 193–202, 2019.

[27] P. Kundur *et al.*, “Definition and classification of power system stability,” *IEEE Trans. Power Syst.*, vol. 19, no. 3, pp. 1387–1401, Aug. 2004.

[28] R. Yan, T. K. Saha, and S. Member, “The Anatomy of the 2016 South Australia Blackout : A Catastrophic Event in a High Renewable Network,” *IEEE Trans. Power Syst.*, vol. 33, no. 5, pp. 5374–5388, 2018.

[29] T. L. Vu and K. Turitsyn, “Lyapunov Functions Family Approach to Transient Stability Assessment,” *IEEE Trans. Power Syst.*, vol. 31, no. 2, pp. 1269–1277, 2016.

[30] M. Kabalan, S. Member, P. Singh, S. Member, D. Niebur, and S. Member, “Large Signal Lyapunov-Based Stability Studies in Microgrids : A Review,” *IEEE Trans. Smart Grid*, vol. 8, no. 5, pp. 2287–2295, 2017.

[31] P. V. Converters, H. Wu, S. Member, X. Wang, and S. Member, “Design-Oriented Transient Stability Analysis of,” *IEEE Trans. Power Electron.*, vol. 35, no. 4, pp. 3573–3589, 2020.

[32] H. Wu, S. Member, X. Wang, and S. Member, “Design-Oriented Transient Stability Analysis of Grid-Connected Converters With Power Synchronization Control,” *IEEE Trans. Ind. Electron.*, vol. 66, no. 8, pp. 6473–6482, 2019.

[33] R. Yousefian, S. Member, R. Bhattarai, and S. Member, "Transient Stability Enhancement of Power Grid With Integrated Wide Area Control of Wind Farms and Synchronous Generators," *IEEE Trans. Power Syst.*, vol. 32, no. 6, pp. 4818–4831, 2017.

[34] A. Ashouri-zadeh, M. Toulabi, A. S. Dobakhshari, and A. Mohammad, "Frequency stability improvement in wind- thermal dominated power grids," *IET Gener. Transm. Distrib.*, vol. 14, pp. 619–627, 2020.

[35] I. Microgrids, S. F. Zarei, H. Mokhtari, S. Member, and F. Blaabjerg, "Fault Detection and Protection Strategy for Islanded," *IEEE J. Emerg. Sel. Top. Power Electron.*, vol. 6777, no. c, pp. 1–12, 2019.

[36] S. F. Zarei, H. Mokhtari, M. A. Ghasemi, and F. Blaabjerg, "Reinforcing Fault Ride Through Capability of Grid Forming Voltage Source Converters Using an," *IEEE Trans. Power Deliv.*, vol. 34, no. 5, pp. 1827–1842, 2019.

[37] R. Liu, J. Yao, X. Wang, P. Sun, and J. Pei, "Dynamic Stability Analysis and Improved LVRT Schemes of DFIG-Based Wind Turbines During a Symmetrical Fault in a Weak Grid," *IEEE Trans. Power Electron.*, vol. 35, no. 1, pp. 303–318, 2020.

[38] H. Urdal, R. Ierna, J. Zhu, C. Ivanov, A. Dahresobh, and D. Rostom, "System strength considerations in a converter dominated power system," *IET Renew. Power Gener.*, vol. 9, no. 1, pp. 10–17, 2015.

[39] Y. Li, L. Fan, and Z. Miao, "Stability Control for Wind in Weak Grids," *IEEE Trans. Sustain. Energy*, vol. 10, no. 4, pp. 2094–2103, 2019.

[40] A. Adib, B. Mirafzal, X. Wang, and R. Blaabjerg, "On stability of voltage source inverters in weak grids," *IEEE Access*, vol. 6, pp. 4427–4439, 2017.

[41] P. Mitra, L. Zhang, and L. Harnefors, "Offshore wind integration to a weak grid by VSC-HVDC links using power-synchronization control: A case study," *IEEE Trans. Power Deliv.*, vol. 29, no. 1, pp. 453–461, 2014.

[42] H. Golpîra, H. Seifi, A. R. Messina, and M. R. Haghifam, "Maximum Penetration Level of Micro-Grids in Large-Scale Power Systems: Frequency Stability Viewpoint," *IEEE Trans. Power Syst.*, vol. 31, no. 6, pp. 5163–5171, 2016.

[43] P. Kundur *et al.*, "Definition and Classification of Power System Stability IEEE/CIGRE Joint Task Force on Stability Terms and Definitions," *IEEE Trans. Power Syst.*, vol. 19, no. 3, pp. 1387–1401, 2004.

[44] M. Farrokhabadi *et al.*, “Microgrid Stability Definitions, Analysis, and Examples,” *IEEE Trans. Power Syst.*, vol. 35, no. 1, pp. 13–29, 2020.

[45] M. Tsili and S. Papathanassiou, “A review of grid code technical requirements for wind farms,” *IET Renew. Power Gener.*, vol. 3, no. 3, pp. 308–332, 2009.

[46] Y. K. Wu, S. M. Chang, and P. Mandal, “Grid-Connected Wind Power Plants: A Survey on the Integration Requirements in Modern Grid Codes,” *IEEE Trans. Ind. Appl.*, vol. 55, no. 6, pp. 5584–5593, 2019.

[47] K. Christakou, J. Y. Leboudec, M. Paolone, and D. C. Tomozei, “Efficient computation of sensitivity coefficients of node voltages and line currents in unbalanced radial electrical distribution networks,” *IEEE Trans. Smart Grid*, vol. 4, no. 2, pp. 741–750, 2013.

[48] T. Van Cutsem *et al.*, “Test Systems for Voltage Stability Studies: IEEE Task Force on Test Systems for Voltage Stability Analysis and Security Assessment,” *Tec. Rep., TR-19*, pp. 1–161, 2015.

[49] M. Glavic and T. Van Cutsem, “Tracking network state from combined SCADA and synchronized phasor measurements,” *Proc. IREP Symp. Bulk Power Syst. Dyn. Control - IX Optim. Secur. Control Emerg. Power Grid, IREP 2013*, pp. 1–10, 2013.

[50] M. A. Awal, H. Yu, H. Tu, S. M. Lukic, and I. Husain, “Hierarchical control for virtual oscillator based grid-connected and islanded microgrids,” *IEEE Trans. Power Electron.*, vol. 35, no. 1, pp. 988–1001, 2020.

[51] L. Che, M. Shahidehpour, A. Alabdulwahab, and Y. Al-Turki, “Hierarchical coordination of a community microgrid with AC and DC microgrids,” *IEEE Trans. Smart Grid*, vol. 6, no. 6, pp. 3042–3051, 2015.

[52] B. Z. Jin, G. Sulligoi, R. Cuzner, L. Meng, J. C. Vasquez, and J. M. Guerrero, “Next-Generation Shipboard DC Power System,” *IEEE Electrif. Mag.*, vol. 4, pp. 45–57, 2016.

[53] B. J. Matevosyan, H. Urdal, S. Achilles, J. Macdowell, J. O. Sullivan, and R. Quint, “Grid-Forming Inverters,” *IEEE Power Energy Mag.*, vol. 17, no. 6, pp. 89–98, 2019.

[54] D. Pan, X. Wang, F. Liu, and R. Shi, “Transient Stability of Voltage-Source Converters with Grid-Forming Control: A Design-Oriented Study,” *IEEE J. Emerg. Sel. Top. Power Electron.*, vol. 8, no. 2, pp. 1019–1033, 2020.

[55] Q. C. Zhong and G. Weiss, “Synchronverters: Inverters that mimic synchronous generators,” *IEEE Trans. Ind. Electron.*, vol. 58, no. 4, pp. 1259–1267, 2011.

[56] V. Converters, L. Zhang, L. Harnefors, S. Member, H. Nee, and S. Member, “Power-Synchronization Control of Grid-Connected Voltage-Source Converters,” *IEEE Trans. Power Syst.*, vol. 25, no. 2, pp. 809–820, 2010.

[57] J. Rocabert, A. Luna, F. Blaabjerg, and P. Rodríguez, “Control of Power Converters in AC Microgrids,” *IEEE Trans. Power Electron.*, vol. 27, no. 11, pp. 4734–4749, Nov. 2012.

[58] Q. Hu, L. Fu, F. Ma, and F. Ji, “Large Signal Synchronizing Instability of PLL-Based VSC Connected to Weak AC Grid,” *IEEE Trans. Power Syst.*, vol. 34, no. 4, pp. 3220–3229, 2019.

[59] P. Kundur, *Power System Stability and Control*. McGraw-Hill, 1994.

[60] A. K. Abdelsalam, A. M. Massoud, S. Ahmed, and P. N. Enjeti, “High-performance adaptive Perturb and observe MPPT technique for photovoltaic-based microgrids,” *IEEE Trans. Power Electron.*, vol. 26, no. 4, pp. 1010–1021, 2011.

[61] L. Meng *et al.*, “Fast Frequency Response from Energy Storage Systems - A Review of Grid Standards, Projects and Technical Issues,” *IEEE Trans. Smart Grid*, vol. 11, no. 2, pp. 1566–1581, 2020.

[62] F. Wang, J. L. Duarte, and M. A. M. Hendrix, “Grid-interfacing converter systems with enhanced voltage quality for microgrid applicationconcept and implementation,” *IEEE Trans. Power Electron.*, vol. 26, no. 12, pp. 3501–3513, 2011.

[63] IEEE Standard Association, *IEEE Std. 1547-2018. Standard for Interconnection and Interoperability of Distributed Energy Resources with Associated Electric Power Systems Interfaces*. 2018.

[64] J. Sun, D. M. Mitchell, and D. E. Jenkins, “Delay Effects in Averaged Modeling of PWM Converters,” in *Proc. Power Electron. Spec. Conf*, 1999, pp. 1210–1215.

[65] D. Dong, B. Wen, D. Boroyevich, P. Mattavelli, and Y. Xue, “Analysis of phase-locked loop low-frequency stability in three-phase grid-connected power converters considering impedance interactions,” *IEEE Trans. Ind. Electron.*, vol. 62, no. 1, pp. 310–321, 2015.

[66] A. Yazdani and R. Iravani, *Voltage-Sourced Converters in Power Systems: Modeling, Control, and Applications*. John Wiley & Sons, Inc., 2010.

[67] North American Electric Reliability Corporation (NERC), “1200 MW Fault Induced Solar Photovoltaic Resource Interruption Disturbance Report,” no. June, p. 32, 2017.

[68] S. Shah *et al.*, “Large-Signal Impedance-Based Modeling and Mitigation of Resonance of Converter-Grid Systems,” *IEEE Trans. Sustain. Energy*, vol. 10, no. 3, pp. 1439–1449, 2019.

[69] H. Komurcugil and O. Kukrer, “Lyapunov-Based Control for Three-Phase PWM AC / DC Voltage-Source Converters,” *IEEE Trans. Power Syst.*, vol. 13, no. 5, 1998.

[70] M. Huang, Y. Peng, C. K. Tse, Y. Liu, J. Sun, and X. Zha, “Bifurcation and Large-Signal Stability Analysis of Three-Phase Voltage Source Converter under Grid Voltage Dips,” *IEEE Trans. Power Electron.*, vol. 32, no. 11, pp. 8868–8879, 2017.

[71] W. Du, J. Zhang, Y. Zhang, and Z. Qian, “Stability criterion for cascaded system with constant power load,” *IEEE Trans. Power Electron.*, vol. 28, no. 4, pp. 1843–1851, 2013.

[72] Y. Zhang and L. Xie, “Online Dynamic Security Assessment of Microgrid Interconnections in Smart Distribution Systems,” *IEEE Trans. Power Syst.*, vol. 30, no. 6, pp. 3246–3254, 2015.

[73] P. V. Brogan, R. J. Best, D. J. Morrow, K. McKinley, and M. L. Kubik, “Effect of BESS Response on Frequency and RoCoF During Underfrequency Transients,” *IEEE Trans. Power Syst.*, vol. 34, no. 1, pp. 575–583, 2019.

[74] M. M. Kabsha and Z. H. Rather, “A New Control Scheme for Fast Frequency Support from HVDC connected Offshore Wind Farm in Low Inertia System,” *IEEE Trans. Sustain. Energy*, vol. 11, no. 3, pp. 1829–1837, 2020.

[75] H. Sun *et al.*, “Review of Challenges and Research Opportunities for Voltage Control in Smart Grids,” *IEEE Trans. Power Syst.*, vol. 34, no. 4, pp. 2790–2801, 2019.

[76] Australian Energy Market Operator (AEMO), “Black System South Australia 28 September 2016,” 2017.

[77] I. M. Dudurych, “The control of power system with a high wind power

penetration," *2007 IEEE Lausanne POWERTECH, Proc.*, pp. 528–531, 2007.

[78] J. O'Sullivan, A. Rogers, D. Flynn, P. Smith, A. Mullane, and M. O'Malley, "Studying the maximum instantaneous non-synchronous generation in an Island system-frequency stability challenges in Ireland," *IEEE Trans. Power Syst.*, vol. 29, no. 6, pp. 2943–2951, 2014.

[79] D. Popovic and I. Wallace, "International Review of Fault Ride On behalf of EirGrid," *London, Nov.*, 2010.

[80] A. D. Hansen, N. A. Cutululis, H. Markou, P. E. Sørensen, and F. Iov, "Grid fault and design-basis for wind turbines - Final report," *Riso Nat. Lab., Roskilde, Denmark, Tech. Rep. Risø-R-1714(EN), Jan.*, 2010.

[81] K. Sun *et al.*, "Frequency Compensation Control Strategy of Energy Storage in the Wind-energy storage Hybrid System for Improving Frequency Response Performance," *2019 IEEE Ind. Appl. Soc. Annu. Meet. IAS 2019*, pp. 1–8, 2019.

[82] R. Khatami, M. Parvania, and A. Narayan, "Flexibility Reserve in Power Systems: Definition and Stochastic Multi-Fidelity Optimization," *IEEE Trans. Smart Grid*, vol. 11, no. 1, pp. 644–654, 2020.

[83] X. Chen, J. Lv, M. B. McElroy, X. Han, C. P. Nielsen, and J. Wen, "Power system capacity expansion under higher penetration of renewables considering flexibility constraints and low carbon policies," *IEEE Trans. Power Syst.*, vol. 33, no. 6, pp. 6240–6253, 2018.

[84] Y. Lin, Y. Ding, Y. Song, and C. Guo, "A Multi-State Model for Exploiting the Reserve Capability of Wind Power," *IEEE Trans. Power Syst.*, vol. 33, no. 3, pp. 3358–3372, 2018.

[85] Y. Liu, S. You, J. Tan, Y. Zhang, and Y. Liu, "Frequency Response Assessment and Enhancement of the U.S. Power Grids Toward Extra-High Photovoltaic Generation Penetrations-An Industry Perspective," *IEEE Trans. Power Syst.*, vol. 33, no. 3, pp. 3438–3449, 2018.

[86] S. You, Y. Liu, and J. Tan, "Primary Frequency Response Without Curtailing Solar Output in High Photovoltaic," vol. 10, no. 2, pp. 718–728, 2019.

[87] A. Rodriguez-Cabero, J. Roldan-Perez, M. Prodanovic, J. A. Suul, and S. D'Arco, "Coupling of AC Grids via VSC-HVDC Interconnections for Oscillation Damping Based on Differential and Common Power Control," *IEEE Trans. Power Electron.*, vol. 35, no. 6, pp. 6548–6558, 2020.

[88] Electricity Storage Network, "Development of electricity storage in the national interest," *Elect. Stor. Netw., Exet. U.K.*, 2014.

[89] Renewable Energy Association, "Energy Storage in the U.K.—An Overview," *Renew. Energy Assoc., Abu Dhabi, UAE, 2015.*

[90] H. Thiesen, C. Jauch, and A. Gloe, "Design of a system substituting today's inherent inertia in the European continental synchronous area," *Energies*, vol. 9, no. 8, 2016.

[91] G. Delille, B. François, and G. Malarange, "Dynamic frequency control support by energy storage to reduce the impact of wind and solar generation on isolated power system's inertia," *IEEE Trans. Sustain. Energy*, vol. 3, no. 4, pp. 931–939, 2012.

[92] Y. K. Sun, Q. Ding, H. Xing, P. P. Zeng, and F. F. Sun, "Optimal Placement and Sizing of Grid-scale Energy Storage in Distribution Networks with Security Constrains," in *2018 Int. Conf. Power Syst. Tec.*, 2018, pp. 1477–1482.

[93] M. Kabalan, P. Singh, and D. Niebur, "Large Signal Lyapunov-Based Stability Studies in Microgrids: A Review," *IEEE Trans. Smart Grid*, vol. 8, no. 5, pp. 2287–2295, 2017.

[94] H. Wu and X. Wang, "Design-oriented transient stability analysis of grid-connected converters with power synchronization control," *IEEE Trans. Ind. Electron.*, vol. 66, no. 8, pp. 6473–6482, 2019.

[95] J. J. E. Slotine and W. Li, "Applied Nonlinear Dynamics," in *Englewood Cliffs, NJ: Prentice-Hall*, 1991.

[96] M. Liserre, F. Blaabjerg, and S. Hansen, "Design and control of an LCL-filter-based three-phase active rectifier," *IEEE Trans. Ind. Appl.*, vol. 41, no. 5, pp. 1281–1291, 2005.

[97] J. Wang, J. D. Yan, L. Jiang, and J. Zou, "Delay-Dependent Stability of Single-Loop Controlled Grid-Connected Inverters with LCL Filters," *IEEE Trans. Power Electron.*, vol. 31, no. 1, pp. 743–757, 2016.

[98] E. Ebrahimzadeh, F. Blaabjerg, X. Wang, and C. L. Bak, "Optimum Design of Power Converter Current Controllers in Large-Scale Power Electronics Based Power Systems," *IEEE Trans. Ind. Appl.*, vol. 55, no. 3, pp. 2792–2799, 2019.

[99] S. Golestan, F. D. Freijedo, A. Vidal, J. M. Guerrero, and J. Doval-gandoy, “A Quasi-Type-1 Phase-Locked Loop Structure,” *IEEE Trans. Power Electron.*, vol. 29, no. 12, pp. 6264–6270, 2014.

[100] S. Golestan, M. Ramezani, J. M. Guerrero, F. D. Freijedo, and M. Monfared, “Moving average filter based phase-locked loops: Performance analysis and design guidelines,” *IEEE Trans. Power Electron.*, vol. 29, no. 6, pp. 2750–2763, 2014.

[101] P. W. Sauer, M. A. Pai, and J. H. Chow, *Power system dynamics and stability : with synchrophasor measurement and power system toolbox*. John Wiley & Sons, Inc., 2018.

[102] M. Malisoff and F. Mazenc, *Constructions of Strict Lyapunov Functions*. London, 2009.

[103] H. Haes Alhelou, M. Hamedani-Golshan, T. Njenda, and P. Siano, “A Survey on Power System Blackout and Cascading Events: Research Motivations and Challenges,” *Energies*, vol. 12, no. 4, p. 682, Feb. 2019.

[104] T. of P. S. D. P. C. Report, T. F. on S. definitions and characterization of Dynamic, behavior in systems with high penetration of power electronic Interfaced, and Technologies, “Stability definitions and characterization of dynamic behavior in systems with high penetration of power electronic interfaced technologies,” *IEEE Syst. J.*, vol. 11, no. April, pp. 2108–2117, 2020.

[105] D. Gmbh, “PowerFactory 2018,” 2018.

[106] P. Tielens and D. Van Hertem, “The relevance of inertia in power systems,” *Renew. Sustain. Energy Rev.*, vol. 55, no. 2016, pp. 999–1009, 2016.

[107] S. Peyghami, P. Davari, M. Fotuhi-Firuzabad, and F. Blaabjerg, “Standard Test Systems for Modern Power System Analysis: An Overview,” *IEEE Ind. Electron. Mag.*, vol. 13, no. 4, pp. 86–105, 2019.

[108] W. Bignell, H. Saffron, T. T. Nguyen, and W. Derek Humpage, “Effects of machine inertia constants on system transient stability,” *Electr. Power Syst. Res.*, vol. 51, no. 3, pp. 153–165, 1999.

[109] M. Ndreko, S. Rueberg, and W. Winter, “Grid Forming Control Scheme for Power Systems with up to 100% Power Electronic Interfaced Generation: A Case Study on Great Britain Test System,” *IET Renew. Power Gener.*, pp. 1–15, 2020.

[110] D. Della Giustina *et al.*, “Smart Grid Automation Based on IEC 61850: An Experimental Characterization,” *IEEE Trans. Instrum. Meas.*, vol. 64, no. 8, pp. 2055–2063, 2015.

Part II
Selected Publications

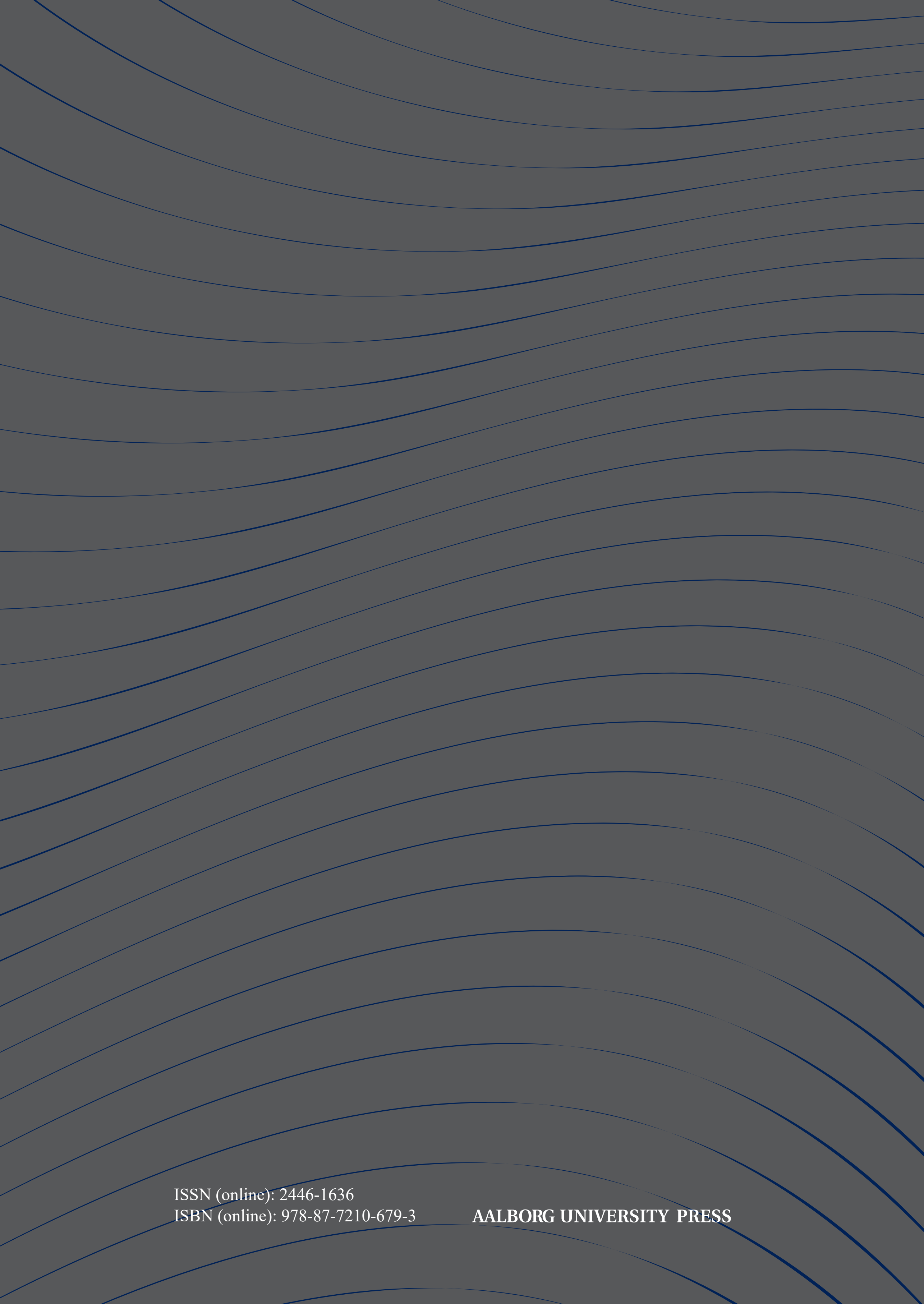

ISSN (online): 2446-1636
ISBN (online): 978-87-7210-679-3

AALBORG UNIVERSITY PRESS